

MORPHOLOGY BASED STOCHASTIC SIMULATION OF SPRAY FLUIDIZED BED AGGLOMERATION

Dissertation

zur Erlangung des akademischen Grades

**Doktoringenieur
(Dr. -Ing.)**

von **M.Sc. Abhinandan Kumar Singh**

geb. am 2 Juli 1991 in Deoghar, Indien

genehmigt durch die Fakultät für Verfahrens- und Systemtechnik
der Otto-von-Guericke-Universität Magdeburg

Promotionskommission:

Prof. Dr. Ir. Berend van Wachem (Vorsitz)

Prof. Dr.-Ing. habil. Evangelos Tsotsas (Gutachter)

Prof. Dr.-Ing. habil. Lutz Mädler (Gutachter)

Prof. Dr.-Ing. Andreas Bück (Gutachter)

eingereicht am 25. November 2020

Promotionskolloquium am 12. März 2021

Declaration

I hereby declare that I prepared the dissertation entitled:

“Morphology based stochastic simulation of spray fluidized bed agglomeration”

submitted without inadmissible assistance and without the use of any aids other than those indicated. Facts or ideas taken from other sources, either directly or indirectly have been marked as such.

In particular, I did not use the services of a commercial graduation consultation. Further I have not made payments to third parties either directly or indirectly for any work connected with the contents of the submitted dissertation.

The work has not been submitted as a dissertation either in Germany or abroad in the same or similar form and has also not been published as a whole.

M.Sc. Abhinandan Kumar Singh

25. November 2020

Abstract

The constant volume Monte Carlo (CVMC) method is a discrete stochastic method that can be used to describe the agglomerate growth during spray fluidized bed (SFB) agglomeration. The methodology overcomes the difficulties of expressing and solving multivariate population balance equations. It enables to account for micro-scale events and processes involved in agglomeration, especially for binder addition and drying. Previous CVMC models assume that all agglomerates have the same porosity. This simplistic assumption is replaced in the present work by given fractal dimension, which means that porosity can change with agglomerate size and process conditions.

Morphological descriptors of the SFB agglomerates are imperative in understanding product characteristics that affect their behavior. Morphology plays a crucial role in the evaluation of different micro-scale mechanisms that control the agglomeration process. In the present work, a tunable aggregation model is developed to reconstruct SFB agglomerates consisting of monodisperse spherical primary particles by a particle-cluster algorithm using a novel approach of tuning the fractal dimension at given prefactor. Various morphological descriptors obtained from this aggregation model are validated using experimental data. Furthermore, this aggregation model is incorporated into the CVMC framework to evaluate both, the morphological descriptors and formation kinetics of SFB agglomerates produced under different process conditions (inlet fluidized gas temperature and binder content).

Previous study focused on agglomerates composed of monodispersed primary particles to understand the formation kinetics and morphology of SFB agglomerates. Size dispersity of primary particles is, though, an important aspect to fully assess the morphological features of an agglomerate. Therefore, a polydisperse tunable aggregation model is also developed. It is shown that the radius of gyration, porosity, surface area and agglomeration rate increase with primary particle size dispersity.

Furthermore, the breakage of already formed agglomerates is introduced to improve the predictions of the CVMC model. A dynamic breakage model is developed on the basis of physical properties of binder and agglomerates. The breakage model is incorporated in the CVMC framework to investigate and discuss the influence of breakage on the morphology and kinetics of SFB agglomeration under different operating conditions.

Kurzzusammenfassung

Die Monte Carlo Methode mit konstantem Volumen (CVMC) ist eine diskrete stochastische Methode zur Beschreibung des Agglomeratwachstums während der Sprühwirbelschicht-Agglomeration (SFB). Dieser Ansatz überwindet die Schwierigkeiten beim Ausdrücken und Lösen multivariater Populationsbilanzgleichungen. Er ermöglicht die Berücksichtigung von Ereignissen und Prozessen im Mikromaßstab, die an der Agglomeration beteiligt sind, insbesondere bei der Bindemittelzugabe und Trocknung. Frühere CVMC-Modelle gehen davon aus, dass alle Agglomerate die gleiche Porosität haben. Diese vereinfachte Annahme wird in der vorliegenden Arbeit durch eine gegebene fraktale Dimension ersetzt, was bedeutet, dass sich die Porosität mit der Agglomeratgröße und den Prozessbedingungen ändern kann.

Die morphologischen Deskriptoren der SFB-Agglomerate müssen zum Verständnis der Produkteigenschaften, die das Verhalten des Produkts beeinflussen, bekannt sein. Die Morphologie von SFB-Agglomeraten spielt zudem eine entscheidende Rolle bei mikroskaligen Mechanismen, die den Agglomerationsprozess steuern. In der vorliegenden Arbeit wird ein einstellbares Aggregationsmodell entwickelt, um die aus monodispersen sphärischen Primärpartikeln bestehenden SFB-Agglomerate mit Hilfe eines Partikel-Cluster-Algorithmus zu rekonstruieren. Dabei wird ein neuartiger Ansatz zur Abstimmung der fraktalen Dimension auf einen gegebenen Präfaktor verwendet. Verschiedene morphologische Deskriptoren, die aus dem Aggregationsmodell gewonnen wurden, werden anhand experimenteller Daten validiert. Darüber hinaus wird das Aggregationsmodell in das CVMC-Modell integriert, um sowohl die Morphologie als auch die Bildungskinetik von SFB-Agglomeraten für verschiedene Prozessbedingungen (Gaseintrittstemperatur, Bindemittelgehalt) berechnen zu können.

Derzeit konzentrierte sich die Arbeit auf Agglomerate aus monodispersen Primärpartikeln, um deren Bildungskinetik und Morphologie zu verstehen. Die

Größendispersion der Primärpartikel ist jedoch ein wichtiger Aspekt zur vollständigen Erfassung der morphologischen Merkmale eines Agglomerats. Daher wird auch ein polydisperses einstellbares Aggregationsmodell entwickelt. Es wird gezeigt, dass Kreisradius, Porosität, Oberfläche und Agglomerationsrate mit der Primärpartikeldispersität zunehmen.

Darüber hinaus wird das Aufbrechen bereits gebildeter Agglomerate eingeführt, um die Vorhersagen des CVMC-Modells zu verbessern. Ein dynamisches Bruchmodell wird auf Grundlage der physikalischen Eigenschaften von Bindemittel und Agglomeraten entwickelt. Dieses wird in den CVMC-Rahmen aufgenommen, um den Einfluss des Bruchs auf Morphologie und Kinetik des SFB-Agglomerationsprozesses unter verschiedenen Betriebsbedingungen untersuchen und diskutieren zu können.

Contents

Abstract	v
Kurzzusammenfassung	vii
Contents	ix
Nomenclature	xiii
Chapter 1 Introduction: Theoretical and practical background	1
1.1 Particle growth mechanisms	2
1.1.1 Coating	3
1.1.2 Agglomeration	3
1.1.3 Criterion for domination	3
1.2 Agglomeration processes	4
1.3 Spray fluidized bed agglomeration	4
1.4 Modeling of spray fluidized bed agglomeration processes	5
1.4.1 Population balance equation	6
1.4.2 Monte Carlo method	6
1.4.3 Discrete element method	8
1.5 Morphology of agglomerates	8
1.6 Motivation and goal	9
1.7 Outline of the thesis	11
Chapter 2 Stochastic and discrete modeling of agglomeration processes	15
2.1 Introduction	16
2.2 General algorithm of CVMC model	17
2.3 Fluidized bed parameters	19
2.4 Particle collisions	21
2.5 Droplet deposition	23
2.5.1 Concept of positions	25
2.6 Droplet drying	26
2.6.1 Deposited droplet drying	27

2.6.2	Variation of viscosity during drying.....	31
2.7	Agglomeration criterion.....	32
2.8	Equivalent agglomerate diameter.....	34
Chapter 3	Morphological approach to simulate agglomeration processes	37
3.1	Introduction	38
3.2	Number of primary particles in an agglomerate.....	38
3.3	Center of gravity.....	39
3.4	Radius of gyration.....	40
3.5	Porosity	41
3.5.1	Porosity from the radius of gyration.....	41
3.5.2	Porosity from convex hull.....	42
3.5.3	Comparison of different porosity evaluation methods.....	42
3.6	Fractal properties.....	43
3.6.1	Fractal dimension.....	44
3.6.2	Prefactor	45
3.7	Coordination number	46
3.8	Interrelation and predictability of morphological descriptors	48
3.8.1	Correlation of porosity as a function of fractal properties.....	48
3.8.2	Correlation between fractal properties	54
3.9	Modified Monte Carlo model (CVMC-1).....	57
3.10	Model sensitivity to variation of the initial number of primary particles	59
3.11	Comparison of the old model and the modified MC (CVMC-1) model	62
3.11.1	Agglomerate kinetics.....	65
3.11.2	Agglomerate morphology	67
3.12	Conclusion.....	68
Chapter 4	Aggregation model	71
4.1	Introduction	72
4.2	General classification	72
4.3	Diffusion limited aggregation model.....	75
4.4	Ballistic aggregation model.....	77
4.5	Reaction limited aggregation model	79
4.6	Sticking probability model.....	81
4.7	Tunable aggregation model.....	84

4.8	Tunable sequential aggregation model and its limitation.....	88
4.9	Validation of the TSA model	92
4.10	CVMC simulation incorporated with aggregation model (CVMC-2).....	97
4.11	Conclusion.....	103
Chapter 5 Polydispersity in agglomeration processes.....		105
5.1	Introduction	106
5.2	Polydisperse aggregation model.....	106
5.3	Validation of PTSA model	109
5.4	Effect of polydispersity on morphology using the PTSA model	111
5.5	Effect of polydispersity on kinetics using the CVMC model.....	114
5.6	Conclusion.....	117
Chapter 6 Breakage of SFB agglomerates		119
6.1	Introduction	120
6.2	Breakage model	120
6.3	CVMC simulation incorporated with breakage model	125
6.4	Effect of breakage on kinetics using the CVMC model	126
6.5	Conclusion.....	128
Chapter 7 Influence of process parameters on agglomeration behavior		129
7.1	Introduction	130
7.2	Influence of inlet fluidization gas temperature	130
7.3	Influence of initial binder mass fraction	132
7.4	Comparison of enhanced CVMC model (CVMC-4) with experiments	134
Chapter 8 Conclusions and outlook.....		139
8.1	Conclusions	140
8.2	Outlook	142
References		145
Appendix A Coordination angle.....		153
Appendix B Experiments of Dadkhah		155
B.1	Detailed results of experiments A to F	158
Appendix C Estimation of agglomerate diameter		165

Appendix D	Simulation parameters for different experiment trials	167
-------------------	--	------------

Nomenclature

a	base radius	m
A	area	m ²
Ar	Archimedes number	-
D	diameter	m
D_f	fractal dimension	-
e	restitution coefficient	-
f_{coll}	collision frequency	1/s
F_c	cohesive force	N
F_{coll}	collision frequency prefactor	1/m
g	gravity	m ² /s
h	binder layer thickness	m
h_a	height of particle surface asperities	m
k	fractal prefactor	-
M	mass	kg
\dot{M}	mass flow rate	kg/s
\tilde{M}	molecular weight	kg/kmol
N, n	number of entities	-
P	pressure	Pa
P_v^*	saturation vapor pressure	Pa
q_0	number density size distribution	1/mm
q_3	volume density size distribution	1/mm
r_G	overall growth rate	m/s
R	radius	m
Re	Reynolds number	-
R_g	radius of gyration	m
R_k	killing radius	m
R_l	launching radius	m

Sc	Schmidt number	-
Sh	Sherwood number	-
St_{coal}	Stokes coalescence number	-
St_{coal}^*	Stokes coalescence critical number	-
St_{def}	Stokes deformation number	-
t	time	s
T	temperature	°C
u_c	collision velocity	m/s
u_0	fluidization gas velocity (superficial)	m/s
V	volume	m ³
x	position on x-axis	m
x_b	mass fraction of binder	-
y	position on y-axis	m
\tilde{y}_g	molar fraction in the gas phase	-
Y	moisture content	kg/kg
z	position on z-axis	m

Greek letters

α	angle	deg
β	mass transfer coefficient	m/s
γ	droplet addition rate	1/s
ε	porosity	-
θ	contact angle	deg
μ	viscosity	Pa s
σ	standard deviation of primary particle size	m
σ_T	strength	Pa
ρ	density	kg/m ³
\emptyset	solid volume fraction	-

Subscripts

<i>a</i>	aggregate (cluster)
<i>agg(s)</i>	agglomerate(s)
<i>app</i>	approaching trajectory
<i>b</i>	binder
<i>bed</i>	fluidized bed
<i>cap</i>	spherical cap, deposited droplet
<i>coal</i>	coalescence
<i>d</i>	droplet
<i>dry</i>	drying
<i>e</i>	equivalent sphere
<i>exp</i>	expanded bed
<i>fix</i>	fixed bed
<i>g</i>	fluidization gas
<i>i</i>	particle index
<i>in</i>	inlet
<i>j</i>	particle index
<i>l</i>	liquid, binder
<i>lim</i>	limited value
<i>p</i>	primary particle
<i>pos</i>	position
<i>surf</i>	surface area
<i>w</i>	water
<i>0</i>	initial
<i>*</i>	saturation

Abbreviations

AES	area (surface) equivalent sphere
CC	cluster-cluster aggregation
CFD	computational fluid dynamics
CH	convex hull
CN	coordination number
CVMC	constant volume Monte Carlo
DEM	discrete element method
DLA	diffusion limited aggregation
DLCA	diffusion limited cluster aggregation
HPMC	hydroxypropylmethylcellulose
MC	Monte Carlo
MCN	mean coordination number
PBE	population balance equations
PC	particle-cluster aggregation
PSD	particle size distribution
RLCA	reaction limited cluster aggregation
PTSA	polydisperse tunable sequential aggregation
RG	radius of gyration
SA	sequential algorithm
SFB	spray fluidized bed
TSA	tunable sequential aggregation
VES	volume equivalent sphere

Chapter 1 Introduction: Theoretical and practical background

This chapter gives an overview of the basic principles of size enlargement processes and briefly explains the basics of agglomeration in spray fluidized beds. It is followed by a short overview on modeling schemes of spray fluidized bed agglomeration, which have been used in the past and are often used to determine the kinetics and morphological descriptors. Finally, the scope and objective of present work are explained.

1.1 Particle growth mechanisms

Particle growth is a size enlargement process of combining small particles into large permanent particles (combining the masses of all the individual constituent particles) where the initial primary particles are either visible (agglomeration) or hidden (coating). Particle growth processes are widely used in pharmaceutical, chemical and food industry to modify the physical properties of powders, such as size, shape, porosity, and to generate products with specific desired characteristics, such as solubility, mechanical strength or flowability (Boyce, 2018; Mörl et al., 2007; Peglow et al., 2014). Two different growth mechanisms, namely coating or agglomeration, as shown in Fig. 1.1, can be observed.

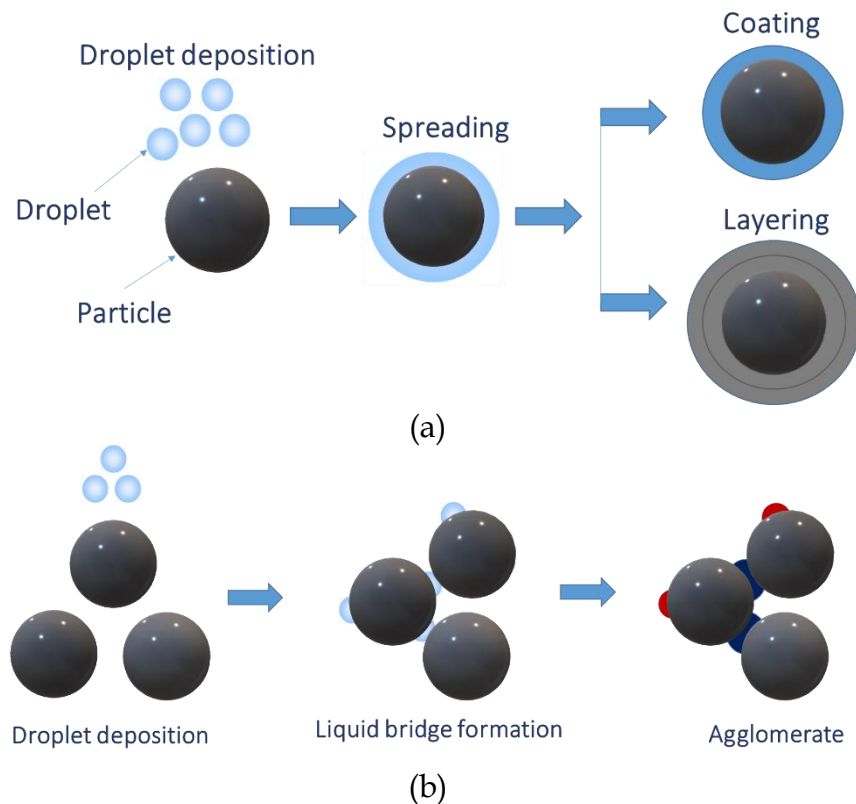


Fig. 1.1: Schematic diagram of two growth mechanisms, coating (a) and agglomeration (b).

1.1.1 Coating

Coating corresponds to the granulation of particles with either the same (termed as layering) or foreign material (Bück et al., 2014). In this process, the coating material is dissolved, finely dispersed and uniformly deposited on the carrier particles. After drying, evaporation of the solvent, the dissolved solute (coating material), which is initially in solution, remains on the surface of the particle and coats it. The thickness of the coating increases by continuous deposition and drying of droplets. Coating can be used to encapsulate substances (Mörl et al., 2007).

1.1.2 Agglomeration

Agglomeration can be defined as the process by which particles are randomly connected or bound together and end up with an aggregate of porous structure much larger than the original material. During collisions between the particles, liquid bridges are formed, which are finally solidified by drying of the dissolved material. Weak bridges are broken by further collisions, while the strong bridges survive and form the final product. If the primary particles are not soluble, binder must be added to the sprayed liquid.

1.1.3 Criterion for domination

Depending on the process conditions and the materials used, two mechanisms of particle growth can be observed: coating or agglomeration (Bück et al., 2014). The border between them, which also makes the boundary of validity of agglomeration models, has recently been evaluated and discussed in detail in (Rieck et al., 2020). Regime maps have been created based on the likelihood of a successful collision to determine the dominant growth mechanism. The present work is focused on size enlargement by agglomeration.

1.2 Agglomeration processes

Many techniques to carry out agglomeration processes are available depending on the nature of material used and on the end-product applications (Bück et al., 2014). Agglomerate properties like growth and structure depend on many parameters, linked to the type of equipment, operating conditions, the particle materials, and sprayed liquid properties (Peglow et al., 2014). The most common types of agglomeration are categorized as pressure, sintering and tumble agglomeration.

The first two technologies make use of mechanical agitation to set the particles in motion and are normally operated in continuous mode. This study is focused on spray fluidized bed processes, which are in the category of tumble agglomeration. Spray fluidized bed agglomerators produce high porosity particles and are known by their very good heat and mass transfer rates which make possible the simultaneous liquid dispersion and drying.

1.3 Spray fluidized bed agglomeration

Spray fluidized bed (SFB) agglomeration is a size enlargement process used to enhance the properties of powders (Mörl et al., 2007). A schematic diagram for SFB agglomeration is given in Fig. 1.2. In this process, liquid binder sprayed through a nozzle upon the fluidized particles wets the surface of the particles. Due to fluidization, the particles collide with each other and form liquid bridges. Water present in the binder evaporates into the fluidizing gas used as a drying agent. Solid bonds are formed between the primary particles in the agglomerate, resulting in a blackberry like structure (Dernedde et al., 2013). The properties of the agglomerates formed depend on the materials used, the type of equipment used and the operating conditions (Peglow et al., 2007). SFB agglomeration is widely applied in chemical, pharmaceutical and food industry to influence product properties such as shelf life,

composition, porosity, size and moisture content. The formulation of new products is still challenging, as mixing, wetting and drying occur simultaneously in the bed and are difficult to control independently. Final products have different microscopic structures, resulting in different macroscopic characteristics and end-use properties, such as strength, stability, flowability, porosity, re-dispersion and abrasivity (Peglow et al., 2014).

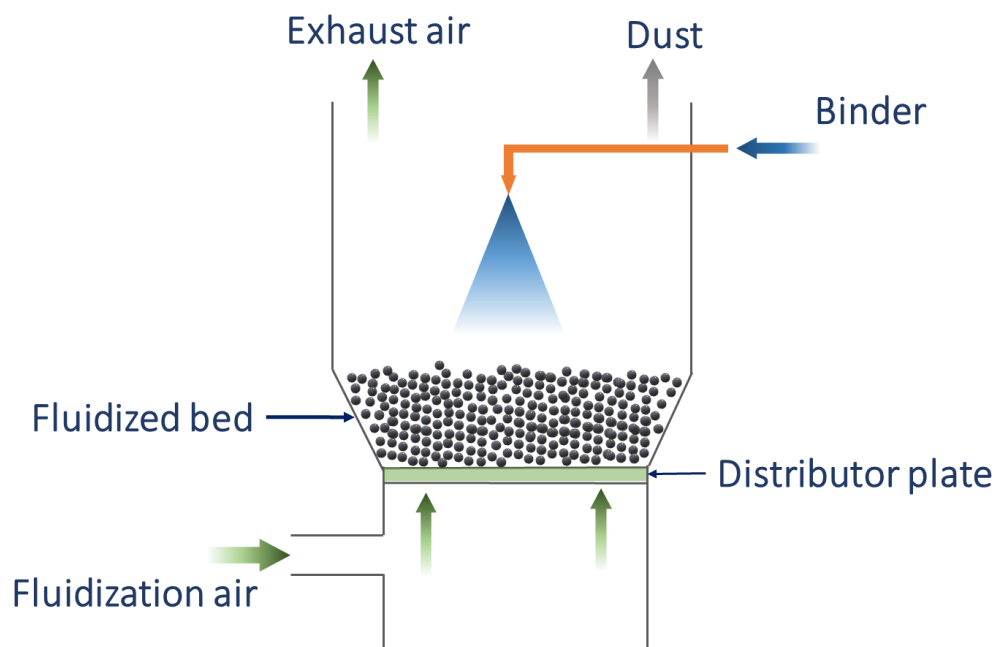


Fig. 1.2: Schematic diagram of spray fluidized bed agglomeration.

1.4 Modeling of spray fluidized bed agglomeration processes

Modeling of enlargement in particulate systems is essential to analyze and understand the underlying phenomena behind the formation of SFB agglomerates. The focus of

the present work is to model spray fluidized bed agglomeration in batch mode of operation. This is often done macroscopically using population balance equations (PBE) (Kumar, 2006; Peglow et al., 2007) and microscopically using Monte Carlo models (Dernedde et al., 2012; Singh & Tsotsas, 2019; Terrazas-Velarde et al., 2009) and discrete element methods coupled with computational fluid dynamics (Dosta et al., 2013; Jiang et al., 2020).

1.4.1 Population balance equation

Population balance equations (PBE) are a common and effective approach to track the evolution of the particle size distribution (PSD) in any size enlargement process (Hussain et al., 2013). PBE are integro-differential equations which must be discretized both spatially and temporally. The occurrence of each event possesses a probability, which is related to the operating conditions of SFB agglomeration and can be statistically described by kernels. In addition, initial conditions and at least one realistic kernel are mandatory for solving the PBE (Hussain et al., 2014; Peglow et al., 2007b).

The kernels in PBE have to be obtained from experimental results and empirical correlations. Besides, the Monte Carlo (MC) method was also used to model the aggregation kernel of PBE in a way that the effect of micro-scale mechanisms on the macroscopic kinetics of the process can be analyzed (Hussain et al., 2014). However, obtaining the kernels is complicated and increases the difficulty of solving PBE.

1.4.2 Monte Carlo method

The Monte Carlo method (Metropolis & Ulam, 1949) is a probabilistic approach to investigate a problem by using the statistical properties of a finite sample of entities. The advantages of the MC model over the deterministic approach and its various applications have been stated in (Yu, 2016; Zhang et al., 2019). With the advancement

of computational machines, MC methods have become an important alternative for the solution of complex problems. A common classification of different Monte Carlo methods is given in Table 1.1.

Table 1.1. Monte Carlo methods.

Simulation box size regulation	Constant number (Smith & Matsoukas, 1998)	Constant volume (Zhao et al., 2007)
Treatment of time step	Event-driven (Terrazas-Velarde et al., 2009)	Time-driven (van Peborgh Gooch & Hounslow, 1996)

Monte Carlo methods are divided into two groups according to the size regulation of simulation box: continuous (constant number) and periodic (constant volume). In constant volume MC (CVMC) methods, the number of particles is doubled after it has reached half of its original value in a simulation dominated by agglomeration. In contrast, the number of particles is halved after it has reached twice its original value in breakage-dominant simulations. However, in constant number MC methods, the regulation of the particle number is performed in each time step. A particle is added or deleted from the simulation box as soon as an agglomeration or breakage event has occurred.

Monte Carlo methods are further divided into two groups according to the treatment of the time step: event-driven and time-driven methods. In the event-driven approach, an event is designed to occur and then time runs by a predetermined amount. In the time-triggered approach, a time step is first specified and then all possible events within this time step are implemented.

1.4.3 Discrete element method

In addition to the models that are based on the probabilistic approach of sequential addition of primary particles, there are other models of deterministic nature, such as the discrete element method. In this method each particle is considered as a separate entity and the Newtonian equation of motion is solved for each particle. The formation of agglomerates is modeled by considering the cohesive force between the primary particles and is represented as a set of primary particles connected with solid bonds of the binder (Dosta et al., 2013; Sommerfeld & Stübing, 2017). Discrete element methods can be coupled with computational fluid dynamics (CFD-DEM) (Dosta et al., 2013; Jiang et al., 2020) to simulate granulation processes. CFD-DEM simulations can be used for SFB coating (Jiang et al., 2018), but not yet for SFB agglomeration, because collision frequencies and velocities that currently popular definitions deliver don't match with MC models. However, CFD-DEM results can help to distinguish between different zones (for example, spray and drying zone) in multi-compartment MC models (Jiang et al., 2020).

1.5 Morphology of agglomerates

Morphological descriptors of agglomerates formed in a SFB process are imperative in understanding the characteristics of a product that affect its behavior. They play a vital role in determining the breakage and droplet (binder) deposition mechanism of an agglomerate. The fractal properties (prefactor and fractal dimension) which are key characteristics of an agglomerate, usually represent compactness and arrangement of primary particles. It had been seen in the past (Brasil et al., 2001; Sorensen & Roberts, 1997) that both prefactor and fractal dimension must be properly ascertained in order to determine the structure of an agglomerate. Porosity and coordination number (CN) are other prominent morphological properties of agglomerates. Porosity is a measure of the internal pores and cavities that affects the strength and density of an

agglomerate (Baric et al., 2019; Klobes et al., 2006). Coordination number also affects the strength of an agglomerate as it defines the connectivity of the primary particles with each other.

1.6 Motivation and goal

SFB agglomeration occurs by combination of many micro-scale mechanisms like binder addition, collision, adhesion, bridge formation, drying and breakage. Terrazas (Terrazas-Velarde et al., 2009) developed a MC simulation method that enhanced the understanding of the spray fluidized bed agglomeration process by implementing most of the underlying micro-scale mechanisms. This model can easily predict the kinetics of the process under different operating conditions. However, the morphology of the final agglomerates was not captured as the formed particles were assumed to be spheres of constant porosity, with a quite arbitrarily chosen value of porosity equal to 0.6.

In recent years, experiments have been conducted to study the morphology of SFB agglomerates formed at different operating conditions using either rigid (Dadkhah & Tsotsas, 2014) or deformable (Pashminehazar et al., 2016) primary particles. The internal structure of the agglomerates produced by SFB agglomeration at different operating conditions was investigated by means of X-ray μ -computed tomography (Dadkhah et al., 2012). Apart from the agglomerates formed by spherical primary particles, some non-spherical primary particle experiments have also been conducted to describe the morphology of soft material agglomerates (Pashminehazar et al., 2016).

In the present work, a cross-correlation between the main morphological descriptors is formulated for agglomerates formed from spherical primary particles. The agglomerate size is determined by considering spheres with characteristic diameter as

a function of number of primary particles (N_p) and their fractal properties (D_f, k). Various empirical correlations are obtained from the experimental data to reduce the number of parameters necessary in order to predict the agglomerate size.

Numerically, the interest in structure formation by aggregation of small particles has motivated the search for simulation algorithms that might give comparable results to experimental observations. For instance, Dervedde (Dervedde et al., 2012) proposed a novel approach to simulate the structure of SFB agglomerates using a cluster-cluster ballistic aggregation model, which stores and preserves a complete description of the spatial arrangement of primary particles. However, the formed agglomerates were predicted too porous and the model was computationally very expensive and slow.

A fast and tunable structure formation model is developed for estimating the agglomerate morphology corresponding to its fractal properties. Further, this structure model is incorporated into the CVMC simulation to reconstruct emerging SFB agglomerates computationally. Various morphological descriptors of agglomerates formed under different operating conditions, such as inlet air temperature and binder content, are predicted and compared with experimental results from (Dadkhah & Tsotsas, 2014).

In general, however, agglomerates typically consist of polydisperse primary particles. There is great interest in understanding the formation dynamics and structure of such agglomerates, and especially their agglomeration rate, which strongly influences the design of the agglomerator. Several studies have been conducted to analyze the influence of polydispersity on the physical or chemical properties of fractal aggregates made of very small primary particles, such as sintering, coagulation and radiation properties (Dastanpour & Rogak, 2016; Goudeli et al., 2016; Morán et al., 2018). However, the influence of polydispersity on the kinetics and morphology of SFB agglomerates has not yet been investigated. In the present work, a polydisperse tunable aggregation model is developed to generate the SFB agglomerates. This

structural model is combined with the models that describe micro-scale processes and events in the comprehensive simulation framework (CVMC). The influence of polydisperse primary particles on morphology and overall kinetics of SFB agglomeration is investigated using the CVMC model.

Breakage of already formed agglomerates is introduced in the CVMC model as a mechanism that decreases the growth rate and can lead to an equilibrium between growth (agglomeration) and rupture (binary breakage), which is typical for fluidized bed processes. Finally, the influence of the breakage mechanism on the overall kinetics of SFB agglomeration is analyzed and compared with experimental results from (Dadkhah, 2014) under different operating conditions.

1.7 Outline of the thesis

This thesis consists of several chapters dealing with the stochastic modeling of spray fluidized bed agglomeration processes by incorporating the morphological influence of the agglomerates on their properties.

Chapter 2 describes in detail the CVMC model and the sub-models for the different micro-scale mechanisms that influence the agglomeration process. This model uses random tools, which represent the basis for the stochastic simulation of agglomeration processes.

Chapter 3 describes the morphological descriptors and the properties of an agglomerate associated with it. A cross-correlation between the main morphological descriptors is formulated for agglomerates formed from spherical primary particles. The formulated correlation is used to check the consistency of morphological data measured by (Dadkhah, 2014). A characteristic diameter, which is a function of fractal dimension and prefactor, is developed and considered to reflect the structure of the

agglomerates. Various empirical correlations are obtained from the experimental data to reduce the number of parameters necessary in order to predict the agglomerate size. Subsequently, the MC model from Chapter 2 is modified by implementing the correlations to predict the morphology of the agglomerates formed as well as the kinetics of the process at different operating conditions.

Chapter 4 reviews various structure-based algorithms and their limitations with regard to SFB agglomerates. A fast and tunable structure formation model for estimating the agglomerate morphology corresponding to its fractal properties is developed. Further, a modification to the CVMC model from Chapter 3 is made by implementing this structure formation model to reconstruct emerging SFB agglomerates computationally. Implementation of the structure formation model in the CVMC simulation can be either in-situ or post-processing. Morphological descriptors of agglomerates formed under different operating conditions, such as inlet air temperature and binder content, are predicted and compared with experimental results from (Dadkhah & Tsotsas, 2014).

In Chapter 5, a polydisperse aggregation model is developed to investigate the influence of primary particle size dispersity on the morphology and size distribution of SFB agglomerates. This structural model is combined with the CVMC framework to study the influence of primary particle size dispersity on the overall growth kinetics.

Chapter 6 describes in detail the formulation of a dynamic breakage model. This breakage model is introduced in the CVMC model as a mechanism that decreases the growth rate and can lead to an equilibrium between growth (agglomeration) and rupture (binary breakage), which is typical for fluidized bed processes. The influence of the breakage mechanism on the overall kinetics of SFB agglomeration is analyzed and compared with experimental results.

Chapter 7 investigates the influence of process parameters on the overall process kinetics and the morphology of agglomerates. The CVMC simulation results are compared with the experiments of Dadkhah.

Finally, although each chapter has its own conclusion, the last Chapter 8 provides the most relevant conclusions and an outlook to future research.

Chapter 2 Stochastic and discrete modeling of agglomeration processes

Spray fluidized bed agglomeration involves many micro-scale mechanisms. This chapter provides a detailed description of the CVMC algorithm used in the present study. This model enhanced the understanding of the spray fluidized bed agglomeration process by implementing some of the underlying micro-scale mechanisms. It uses probabilistic tools to simulate the evolution of a finite sample of the particle population during the process. The individual role of the micro-scale mechanisms on the agglomeration behavior can be analyzed due to the discrete nature of the approach.

2.1 Introduction

Spray fluidized bed (SFB) agglomeration processes take place by combination of many micro-scale mechanisms like binder addition, collision, adhesion, bridge formation, drying and breakage (Dernedde et al., 2013), given in Fig. 2.1.

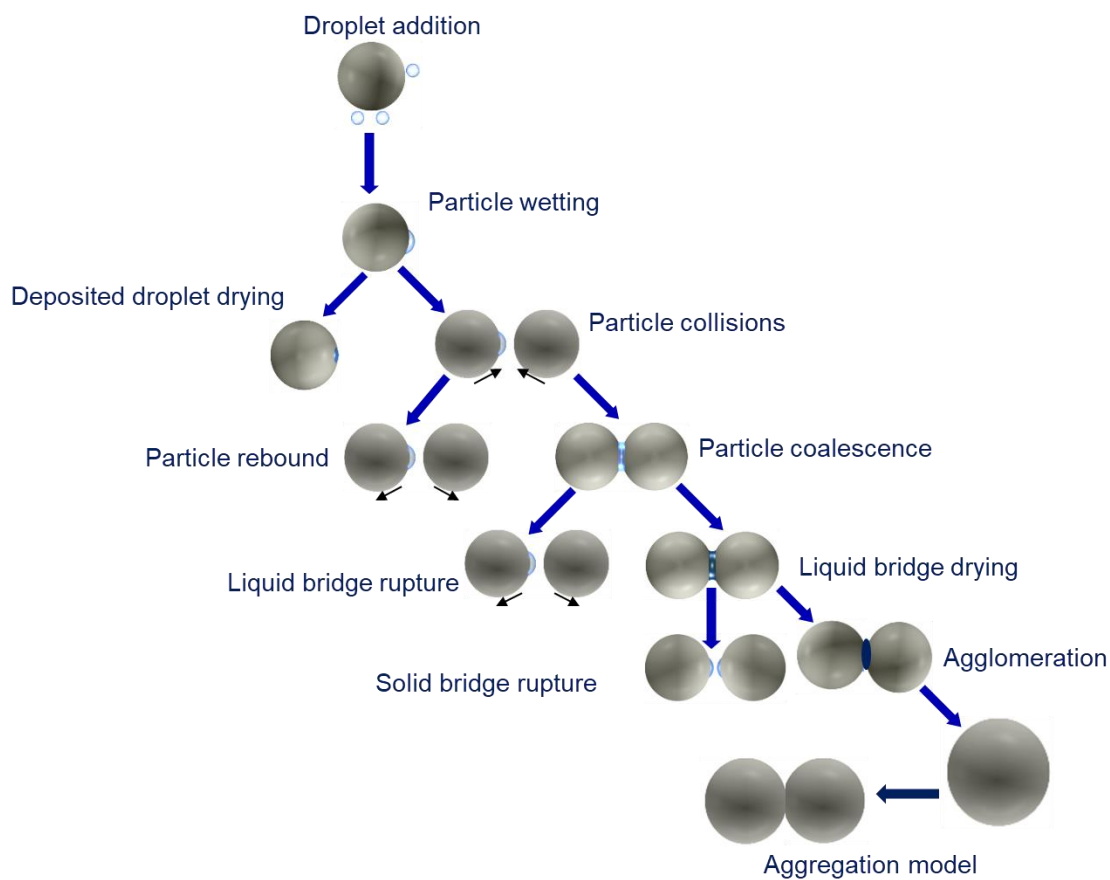


Fig. 2.1: Micro-scale mechanisms of spray fluidized bed agglomeration.

In SFB agglomeration, the particles are fluidized by inlet gas from the bottom of the granulator. In addition, liquid binder in the form of small droplets is sprayed onto the fluidized particles to make them wet and sticky. As soon as a droplet enters the system, it is deposited on the particles. In a state of equilibrium, a droplet takes the form of a spherical cap and gradually loses height, mainly due to two mechanisms:

drying and imbibition. Imbibition is the process of droplets penetrating into the particles and occurs only in porous particles. The deposited droplets can disappear from the surface of the particles by drying and/or imbibition. It is therefore important for agglomeration that particle collisions take place before the deposited droplets have disappeared. The following scenarios are observed for random collisions between particles:

- I. rebound of the particles, because the liquid layer does not dissipate the kinetic energy of the collision;
- II. agglomeration, because the liquid layer can successfully dissipate the kinetic energy of the collision;
- III. breakage, because the kinetic energy of the collision can be so high that it not only overcomes the resistance of the liquid layer but also forces already formed solid and/or liquid bridges of colliding particles to break.

In order to simulate the overall SFB agglomeration process, a MC method is considered in this work for describing random events and processes (micro-scale mechanisms), creating a scaled-down virtual spray fluidized bed granulator, similar to the work of Terrazas (Terrazas-Velarde et al., 2009) and Dervedde (Dervedde et al., 2012).

2.2 General algorithm of CVMC model

A comprehensive CVMC model, introduced by Terrazas (Terrazas-Velarde et al., 2009), is used by incorporating most of the micro-scale mechanisms to simulate the SFB agglomeration by treating the CVMC simulation box as a scaled-down virtual granulator, as shown in Fig. 2.2. The framework of the CVMC simulation has been set and the simulations have been conducted in MATLAB using self-programmed codes.

The event-driven nature of the method, with collision events between particles in the fluidized bed being the pacemakers, establishes the connection between the CVMC model and the real particulate system. Under this methodology, an event occurs first and then time is advanced by an appropriate amount.

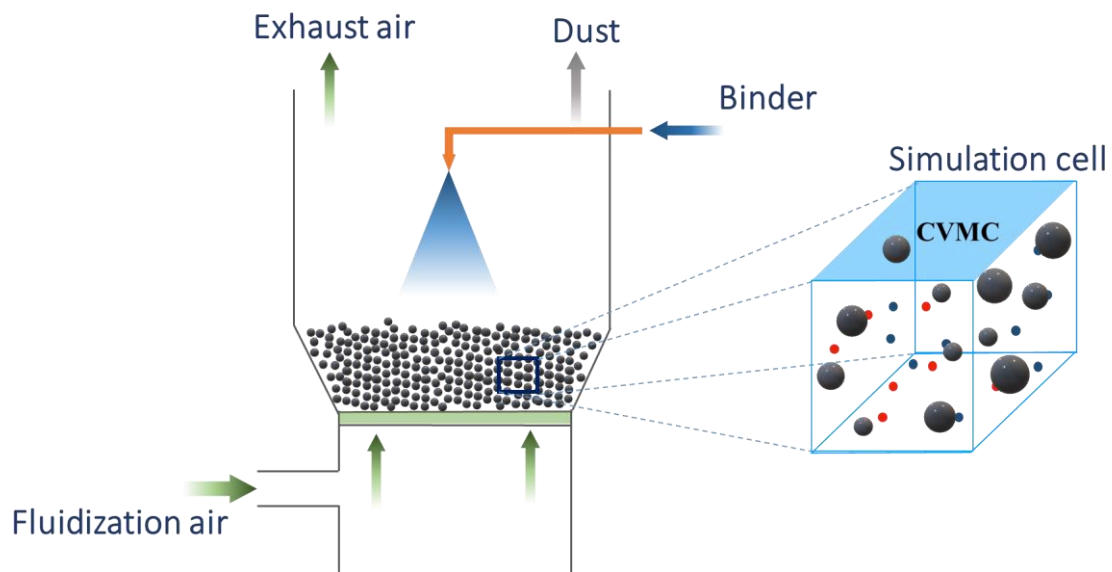


Fig. 2.2: CVMC modeling scheme for spray fluidized bed agglomeration.

The simulation box is considered as a representative sample of the particle population, consisting of an initial number of primary particles. The number of particles in the simulation box changes depending on the process, namely agglomeration or breakage, which dominates during the simulation. The periodic regulation of the particles takes place when the number of particles in the simulation box has been halved by doubling the particle population. An exact copy of the particle population is then introduced to the simulation box, restoring the number of entities to the initial value.

Collisions between primary particles and droplet deposition start taking place simultaneously with the begin of the simulation. Droplets randomly deposit on the primary particles (later on, on agglomerates) and eventually dry off. After a successful

collision of primary particles on wet areas, an agglomerate may form. The flowchart of the CVMC model is given in Fig. 2.3.

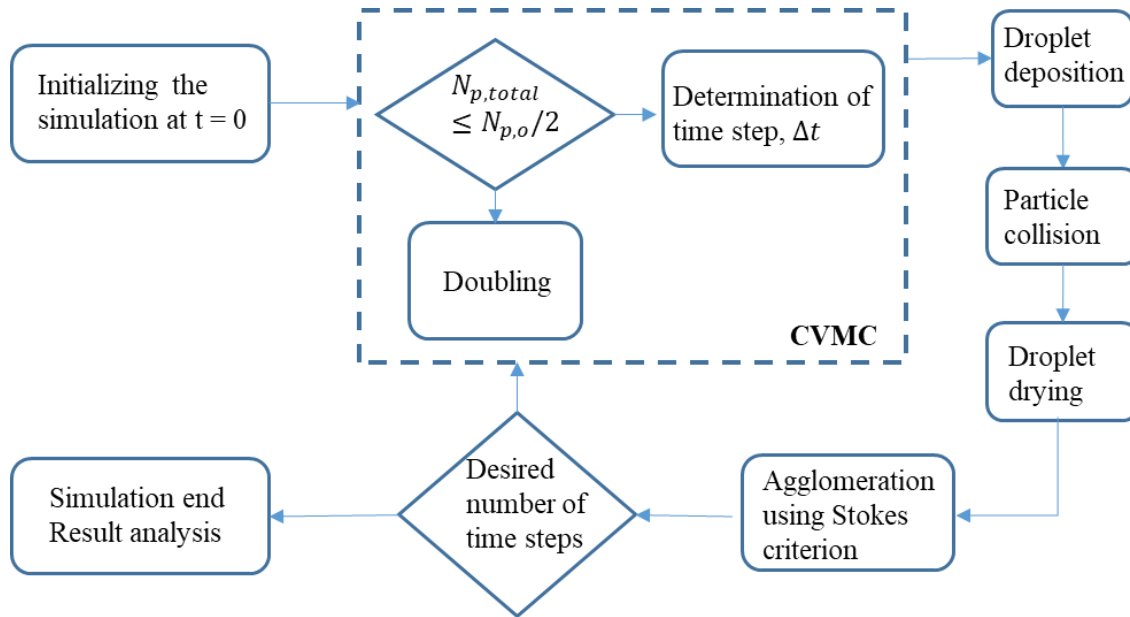


Fig. 2.3: Flowchart representation of CVMC modeling for spray fluidized bed agglomeration.

2.3 Fluidized bed parameters

The simulation corresponds to a batch process in which the mass flow rate of the fluidizing gas is kept constant during the entire agglomeration process. The fixed bed void fraction ε_{fix} is assumed equal to 0.39, which corresponds to a random packing of monodispersed spheres. As soon as fluidization has been started, the bed reaches its maximum void fraction ε_{exp} which depends on the gas velocity u_0 and particle properties, as described by (Mörl et al., 2007)

$$\varepsilon_{exp} = \left(\frac{18Re_p + 0.36Re_p^2}{Ar} \right)^{0.21}. \quad (2.1)$$

Here, Re_p and Ar are the particle Reynolds and Archimedes dimensionless numbers defined by

$$Re_p = \frac{u_o \rho_g D_{agg,32,t}}{\mu_g}, \quad (2.2)$$

$$Ar = \frac{D_{agg,32,t}^3 \rho_g (\rho_p - \rho_g) g}{\mu_g^2}. \quad (2.3)$$

Here, ρ_g and ρ_p are densities of dry gas (i.e. air) and primary particle, respectively, g is the acceleration due to gravity taken to be 9.8 m/s^2 , $D_{agg,32,t}$ is Sauter mean diameter of the particle population in the simulation box at time t (at $t = 0$; $D_{agg,32,t} = D_p$) and μ_g is the dynamic viscosity of the dry gas. The density and dynamic viscosity of the dry gas are calculated in kg/m^3 and Pa s , respectively, by empirical correlations given in (Terrazas-Velarde, 2012) as

$$\rho_g = 9.04 \times 10^{-9} T_g^3 + 9.45 \times 10^{-6} T_g^2 - 4.25 \times 10^{-3} T_g + 1.29, \quad (2.4)$$

$$\mu_g = 3.89 \times 10^{-8} T_g + 1.779 \times 10^{-5}, \quad (2.5)$$

where T_g is the inlet gas temperature in $^\circ\text{C}$.

As agglomeration progresses, the particles become larger and the expanded bed void fraction decreases. This is accompanied by a contraction of the bed from its maximum height to the fixed bed height. The height of the expanded bed is calculated by

$$H_{exp} = \frac{1-\varepsilon_{fix}}{1-\varepsilon_{exp}} H_{fix}, \quad (2.4)$$

where H_{fix} is the height of the packed bed which is a function of the bed mass M_{bed} , particle density ρ_p and equipment cross-section A as follows

$$H_{fix} = \frac{M_{bed}}{(1-\varepsilon_{exp}) A \rho_p}. \quad (2.5)$$

The simulation is stopped when the void fraction of the expanded bed has become equal to that of the fixed bed ($\varepsilon_{exp} = \varepsilon_{fix} = 0.39$). It is then assumed that the bed has collapsed.

2.4 Particle collisions

Interparticle collisions play a crucial role in the numerical computation performed in this study. Their discrete nature allows us to calculate the length of the time step during the simulation and thus to correlate real with the computational time. In this study, the experimental correlation proposed by (Buffière & Moletta, 2000), is used to estimate the frequency of collisions within the fluidized bed

$$f_{coll} = F_{coll} \left(1 - \frac{\phi_{exp}}{\phi_{fix}}\right) \left(\frac{\phi_{exp}}{\phi_{fix}}\right)^2 u_0, \quad (2.6)$$

where u_0 is the fluidization velocity, ϕ_{exp} and ϕ_{fix} are the solid volume fractions of the expanded bed and the fixed bed, respectively, and F_{coll} is the collision frequency prefactor. This correlation describes the number of collisions that a single particle experiences per unit of time. It can be inferred that the number of collisions strongly

influences the agglomeration rate of the process. The more collisions a particle experiences, the higher is the probability of successful coalescence, assuming that all other parameters are kept constant.

Collision frequency is a crucial model parameter and has been adapted by the prefactor (F_{coll}) of Eq. (2.6) to experimental data. It has been shown in lengths how the value of F_{coll} influences the aggregation rate and that moderate values of this parameter must be selected (Terrazas-Velarde et al., 2011b). Otherwise, there is practically not any inactivation of sterically accessible deposited droplets by drying, gas temperature does not play any role and agglomeration rate is very high. All this would severely contradict many experimental findings, so that it has unequivocally been demonstrated that collision frequency in the CVMC model for SFB agglomeration must be much smaller than the kinetic theory of granular media, particle tracking velocimetry or other experimental techniques behind correlations like that of Eq. (2.6), or CFD-DEM simulations indicate (Jiang et al., 2018).

In SFB agglomeration, however, the overall growth kinetics depend strongly on the drying process of droplets. Collision events with partially dried droplets are achieved at lower F_{coll} values. In the present study, F_{coll} is taken as 10 1/m , which has been experimentally validated for spray fluidized bed agglomeration by (Terrazas-Velarde, 2012).

Nevertheless, the correlation according to Eq. (2.6) can describe the behavior of the number of collisions that a particle experiences per unit time as the fluidized bed moves from the packed bed limit ($\phi_{exp} \approx 0.6$; $\varepsilon_{exp} \approx 0.4$) to the elutriation limit ($\phi_{exp} \approx 0$; $\varepsilon_{exp} \approx 1$). Solid volume fraction of the fixed bed is assumed $\phi_{fix} = 0.61$, corresponding to a packing of spheres with porosity equal to 0.39 (Terrazas-Velarde et al., 2009). The solid volume fraction of the expanded bed is by definition

$$\emptyset_{exp} = 1 - \varepsilon_{exp}. \quad (2.7)$$

Here, ε_{exp} is the voidage of the expanded bead and is computed by Eq. (2.1).

In order to advance the simulation in real-time, a number of collision events (i.e. 2000) are set at the beginning of the simulation. As the events occur one after the other, the collision frequency for each event is calculated using Eq. (2.6), and from the collision frequency the length of the time step for between subsequent collision events is set to

$$t_{step} = \frac{1}{f_{coll}}. \quad (2.8)$$

2.5 Droplet deposition

In the CVMC model, hydroxypropylmethylcellulose (HPMC) binder dissolved in water is continuously added to the particles. The relationship between the real process and the model is established by the concentration of droplets per unit time and particle inside the simulation box. The number of droplets added per unit time and particle in the real process, which depends on the liquid flow rate and the droplet diameter, is

$$\gamma = \frac{\dot{M}_l}{M_{bed}} \left(\frac{\rho_p}{\rho_l} \right) \left(\frac{D_p}{D_d} \right)^3 \quad (2.9)$$

where \dot{M}_l is spray mass flow rate, M_{bed} is bed mass, ρ_p is particle density, ρ_l is liquid density, D_p is mean particle diameter (twice the mean radius, R_p) and D_d is droplet diameter. Depending on surface energy, a liquid droplet deposited on a particle will either spread completely forming a film coating (contact angle $\theta = 0^\circ$) or, in the case

of partial wetting ($\theta > 0^\circ$), it will take the shape of a spherical cap with a base radius a_0 and height h_0 (Clarke et al., 2002). A schematic representation of droplet deposition is shown in Fig. 2.4.

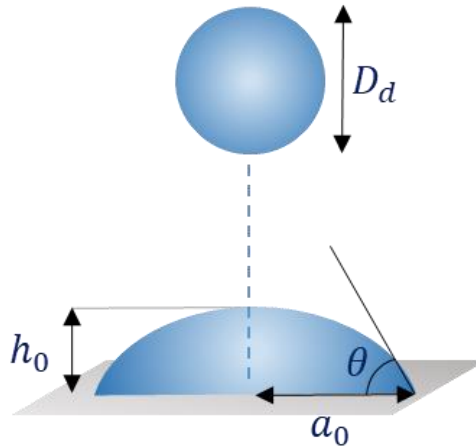


Fig. 2.4: Droplet deposition and geometrical nomenclature.

A value of $\theta = 40^\circ$ applies here for binder deposited on the non-porous glass beads used as primary particles. If the droplet size is assumed relatively small compared to the particle size, so the particle curvature can be neglected, any droplet of volume V_d captured on the surface of a particle is characterized by

$$a_0 = \left(\frac{3V_d}{\pi} \frac{\sin^3 \theta}{2 - 3 \cos \theta + \cos^3 \theta} \right)^{1/3}, \quad (2.10)$$

$$h_0 = a_0 \left(\frac{\sin \theta}{1 + \cos \theta} \right). \quad (2.11)$$

In order to model deposition of binder droplet and wetting of particles (primary particles and agglomerates) a “concept of positions” similar to (Terrazas-Velarde et al., 2011a) is used, cf. (Singh & Tsotsas, 2019, 2020).

2.5.1 Concept of positions

The particles are divided into sectors. A sector of a particle is the part of the surface of the particle facing at and covered by an adjoining particle. With the notion of six neighbors in a simple cubic packing, each particle is assumed to have six sectors. The specific number of six sectors per particle belongs to the parametric setting of the model, which has been taken over from (Terrazas-Velarde et al., 2009), see also (Singh & Tsotsas, 2019). A schematic diagram of this concept is shown in Fig. 2.5.

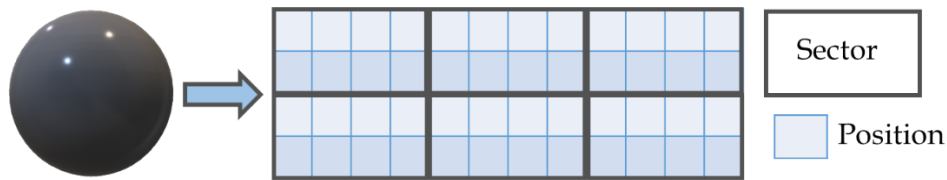


Fig. 2.5: Schematic diagram of the “concept of positions”.

Moreover, for droplet deposition, the area of each sector is further subdivided into smaller areas called positions. The area of each position is approximately set equal to the footprint of a droplet (spherical cap base area). This implies that the total number of positions available for a droplet of certain base radius (a_0) on a particle is given by the reciprocal of the single droplet fractional covered area (ψ_s),

$$N_{pos} = \frac{1}{\psi_s} = \frac{A_{surf}}{\pi a_0^2}. \quad (2.12)$$

The value of N_{pos} is rounded to the nearest integer. Taking into account the diameter of the primary particle as $520 \mu m$ and droplet diameter of $80 \mu m$, the number of positions available on the primary particle is calculated as 47 from Eq. (2.12).

However, for even number of positions on each sector (i.e. 8), the number of positions available on the primary particle is taken as 48.

If one such position has been wetted and resulted in successful agglomeration, all remaining seven positions of the respective sector are inactivated, because they can no more be reached by droplets or other particles. This steric hindrance caused by neighboring particles in the deposition of droplets decreases the agglomeration rate (in addition to the decrease caused by droplet drying) and must be accounted for.

Dry and wet zones on the particles are distinguished by a binary code of zeros and ones, where zero denotes an empty region and one a wet point. Successful coalescence can only occur if the colliding particles touch each other through at least one wetted zone and if the coalescence criterion given by the Stokes number (described in Section 2.7) is fulfilled. Furthermore, overlapping and penetration of the droplets deposited on the particles are not considered in this work.

2.6 Droplet drying

Droplet drying sets on immediately after droplet deposition in spray fluidized bed agglomeration. Two main mechanisms are, in general, responsible for the aging of deposited droplets during fluidized bed agglomeration, namely drying and imbibition into porous substrates. The type of solid substrate is critical and determines which mechanism dominates in height reduction. In non-porous systems, the reduction of deposited droplet height and finally the slowing down of agglomeration due to droplet losses is exclusively due to the drying of the liquid binder. In porous systems, however, both mechanisms are present. In the present work, primary particles are non-porous and therefore, imbibition is not considered.

2.6.1 Deposited droplet drying

Once the droplet has been deposited on the particle, it evaporates and eventually solidifies. For the description of this phenomenon, the particles are considered to be non-porous. Additionally, binder droplet height and radius are assumed to diminish simultaneously, maintaining the contact angle constant (Erbil et al., 2002). Under these conditions, the number of moles of water contained in the deposited droplet is

$$N_w = \frac{\rho_w}{\bar{M}_w} V_{cap}. \quad (2.13)$$

The spherical cap volume is given by (Clarke et al., 2002)

$$V_{cap} = \pi h^3 \left[\frac{1}{1-\cos\theta} - \frac{1}{3} \right]. \quad (2.14)$$

Combining Eq. (2.13) with Eq. (2.14) and taking the first derivative one can obtain

$$\frac{dN_w}{dt} = 3 \frac{\rho_w}{\bar{M}_w} \pi \left[\frac{1}{1-\cos\theta} - \frac{1}{3} \right] h^2 \frac{dh}{dt}. \quad (2.15)$$

Additionally, from the mass balance one gets

$$\frac{dN_w}{dt} = -A_{cap} \beta \frac{\rho_g}{\bar{M}_g} (\tilde{y}^* - \tilde{y}_g), \quad (2.16)$$

where β is the mass transfer coefficient, \tilde{y}^* is the vapor molar fraction for saturation conditions at the droplet-air interface and \tilde{y}_g is the vapor mole fraction in the gas. The spherical cap surface area is given by (Clarke et al., 2002) to

$$A_{cap} = \frac{2\pi h^2}{1-\cos\theta}. \quad (2.17)$$

Substituting Eq. (2.17) in Eq. (2.16), the following expression is obtained

$$\frac{dN_w}{dt} = -\frac{2\pi h^2}{1-\cos\theta} \frac{\rho_g}{\tilde{M}_g} \beta (\tilde{y}^* - \tilde{y}_g). \quad (2.18)$$

Combining Eq. (2.18) with Eq. (2.15), the transformed mass balance is then

$$\left[\frac{1}{1-\cos\theta} - \frac{1}{3} \right] \frac{dh}{dt} = -\frac{2\rho_g \tilde{M}_w}{3\rho_w \tilde{M}_g} \frac{\beta}{1-\cos\theta} (\tilde{y}^* - \tilde{y}_g). \quad (2.19)$$

Integrating Eq. (2.19) under the assumption of a constant mass transfer coefficient, droplet drying is described by reduction of droplet height with time as

$$h = h_0 - \frac{2\rho_g \tilde{M}_w}{3\rho_w \tilde{M}_g} \frac{\beta}{1-\cos\theta} (\tilde{y}^* - \tilde{y}_g) \left[\frac{1}{1-\cos\theta} - \frac{1}{3} \right]^{-1} t. \quad (2.20)$$

Equation (2.20) describes the reduction of the initial binder layer height h_0 of a droplet deposited on a non-porous solid particle by drying as a function of time, temperature (implicit in \tilde{y}^*), fluidization velocity (implicit in the mass transfer coefficient), contact angle, as well as particle, binder and fluidization gas properties. Figure 2.6 shows a graphical representation of deposited droplet drying assuming a simultaneous decrease in height and radius of the drop at a constant contact angle.

The vapor molar fraction at saturation conditions is

$$\tilde{y}^* = P_v^*/P. \quad (2.21)$$

Here, P_v^* and P are the saturation vapor pressure and the system pressure, respectively.

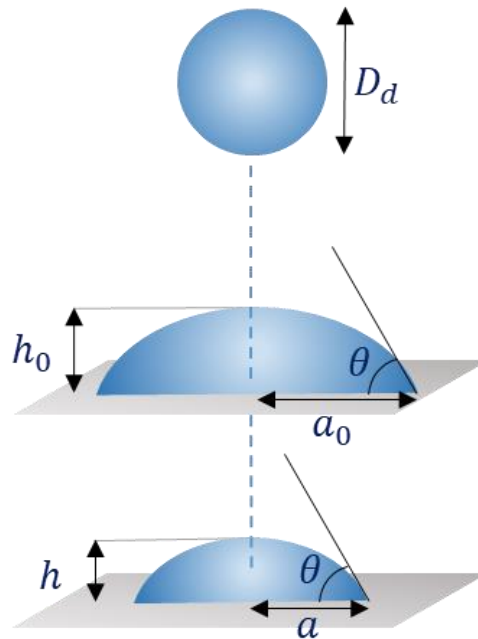


Fig. 2.6: Schematic representation of the reduction in the height of the deposited droplet by drying.

The saturation pressure of water in Pa is calculated by the Antoine equation to

$$P_v^* = \left[10^{8.0713 - \frac{1730.63}{T^* + 233.426}} \right] \frac{101325}{760}, \quad (2.22)$$

where T^* is the adiabatic saturation temperature in °C. The molar fraction of water in the gas phase

$$\tilde{y}_g = \frac{Y_g}{Y_g - (\tilde{M}_w / \tilde{M}_g)} \quad (2.23)$$

is obtained from gas moisture content Y_g . By assuming that the fluidized bed is perfectly mixed and the amount of evaporating water is at any time equal to the amount of water sprayed, the latter can be calculated from

$$Y_g = Y_{g,in} + \frac{\dot{M}_w}{\dot{M}_g}, \quad (2.24)$$

where \dot{M}_g and \dot{M}_w are the mass flow rates of dry gas and sprayed water, respectively.

The mass transfer coefficient β is assumed to be constant and calculated for the initial conditions from correlations for the dimensionless Sherwood number given by (Schlünder & Tsotsas, 1988) as follows:

$$Sh = \frac{\beta l}{\delta}, \quad (2.25)$$

$$Sh = 2 + \sqrt{Sh_1 + Sh_2}, \quad (2.26)$$

$$Sh_1 = 0.664 Re_{cap}^{1/2} Sc^{1/3}, \quad (2.27)$$

$$Sh_2 = \frac{0.037 Re_{cap}^{0.8} Sc}{1 + 2.443 Re_{cap}^{-1} (Sc^{2/3} - 1)}. \quad (2.28)$$

Sc is the dimensionless Schmidt number given by

$$Sc = \frac{\mu_g}{\delta \rho_g}, \quad (2.29)$$

and Re_{cap} is the deposited spherical cap Reynolds number defined by

$$Re_{cap} = \frac{u_0 \rho_g l}{\mu_g}. \quad (2.30)$$

The diffusion coefficient of water in air δ is calculated as

$$\delta = \frac{2.252}{P} \left(\frac{T_g}{273} \right)^{1.81}, \quad (2.31)$$

where T_g is the fluidization gas inlet temperature in K and P is the system pressure in Pa.

The characteristic length l in Eq. (2.30) is assumed to be the initial diameter of the droplet, i.e.

$$l = D_d. \quad (2.32)$$

2.6.2 Variation of viscosity during drying

The deposited droplet has an initial binder mass fraction

$$x_{b,0} = \frac{M_b}{M_b + M_{w,0}}. \quad (2.33)$$

Here, M_b and $M_{w,0}$ are the mass of solute and the initial mass of liquid solvent (water) in the solution, respectively. The mass of solute in the binder solution is constant for each deposited droplet as

$$M_b = x_{b,0} V_{cap,0} \rho_b, \quad (2.34)$$

where ρ_b is the density of the binder solution. As the droplet dries, the mass of solute M_b remains constant and the amount of water M_w is reduced, this leads to an increase in binder mass fraction x_b and therefore, increase in viscosity μ_l of binder solution.

The mass of water in the droplet M_w is calculated at each time step based on the remaining cap volume V_{cap} as

$$M_w = \rho_w V_{cap} = \rho_w \pi h^3 \left[\frac{1}{1-\cos\theta} - \frac{1}{3} \right]. \quad (2.35)$$

Accordingly, the instantaneous average binder mass fraction is given by

$$x_b = \frac{M_b}{M_b + M_w}. \quad (2.36)$$

In order to introduce the change of viscosity due to drying into the model, a relationship between the binder mass fraction x_b (in wt. %) and binder viscosity (in Pa·s) is used, as proposed by (Terrazas-Velarde, 2012):

$$\mu_l = ax_b^3 + bx_b^2 + cx_b + d \quad (2.37)$$

where $a = 7.23 \times 10^{-4}$; $b = -6.42 \times 10^{-3}$; $c = 0.0265$ and $d = -0.0246$ in appropriate units.

2.7 Agglomeration criterion

Particles (primary particles or agglomerates) will coalesce if their initial kinetic energy is small enough to overcome the viscous lubrication resistance in the liquid layer. The critical conditions for the dissipation of kinetic energy by a viscous layer of a given thickness were first derived by (Davis et al., 1986) in the form of a Stokes number

$$St_{coal} = \frac{2M_{agg}s u_c}{3\pi\mu_l D_{agg}s^2}. \quad (2.38)$$

Coalescence between two colliding particles (agglomerates) happens when the Stokes number is smaller than the critical Stokes number (Barnocky & Davis, 1988)

$$St_{coal}^* = \left(1 + \frac{1}{e}\right) \ln\left(\frac{h}{h_a}\right). \quad (2.39)$$

In the case of collision between particles of unequal size, a combined mass and diameter are used:

$$M_{agg}s = \frac{2M_{agg1}M_{agg2}}{M_{agg1}+M_{agg2}}, \quad (2.40)$$

$$D_{agg}s = \frac{2D_{agg1}D_{agg2}}{D_{agg1}+D_{agg2}}. \quad (2.41)$$

The Stokes model depends strongly on the particle collision velocity. In this study, the collision velocity of the pair of particles is randomly chosen by assuming a normally distributed function around a mean value equal to $0.5u_0$ and a standard deviation of 0.1 m/s. This is a coarse assumption in comparison to the velocity distributions in some aerosol aggregation models (Morán et al., 2020), but it belongs to the parametric setting of the MC model for SFB agglomeration that has been adopted from the previous work (Terrazas-Velarde et al., 2009), where it was quite successful in describing experimental results.

2.8 Equivalent agglomerate diameter

For simplification, in the CVMC model, every formed agglomerate is considered as a sphere with a characteristic diameter (D_{agg}). There are many ways of calculating this characteristic diameter. It can, for example, be calculated by using the radius of gyration of the considered agglomerate,

$$D_{agg} = 2R_g. \quad (2.42)$$

Dadkhah provided a correlation to calculate the equivalent radius of agglomerates consisting of monodisperse primary particles using the radius of gyration of the formed agglomerates (Dadkhah et al., 2012),

$$R_e = \sqrt{\frac{5}{3}} R_g. \quad (2.43)$$

From it, the characteristic diameter can be calculated as

$$D_{agg} = 2R_e. \quad (2.44)$$

Knowing the porosity of an agglomerate, the diameter of a volume equivalent sphere can also be used as a characteristic diameter

$$D_{agg} = \left[\frac{\sum_{i=1}^{N_p} D_{p,i}^3}{1 - \varepsilon_{agg}} \right]^{1/3}. \quad (2.45)$$

Porosity of an agglomerate consisting of monodisperse primary particles can be calculated by inserting the fractal properties (Singh & Tsotsas, 2019), or by

reconstructing the agglomerates using an aggregation model (Singh & Tsotsas, 2020). Porosity of an agglomerate consisting of polydisperse primary particles can only be determined by reconstructing the agglomerates using a polydisperse aggregation model.

The diameter of agglomerates composed of polydisperse primary particles can also be determined by generating the agglomerates computationally and evaluating their surface area. The surface area of reconstructed agglomerates can be calculated by using the alphaShape or convex hull functions of MATLAB and it can then be used to determine the diameter by

$$D_{agg} = \left[\frac{A_{surf}}{\pi} \right]^{1/2}. \quad (2.46)$$

Similarly, the volume occupied by the surface laid around the agglomerates by application of the alphaShape or convex hull functions of MATLAB can also be used to determine the diameter of the agglomerates to

$$D_{agg} = \left[\frac{6V_{surf}}{\pi} \right]^{1/3}. \quad (2.47)$$

Few of these methods of determining the diameter of the agglomerates will be discussed and compared in the further chapters.

Chapter 3 Morphological approach to simulate agglomeration processes

This chapter is a modified version of the paper “Stochastic model to simulate spray fluidized bed agglomeration: A morphological approach, Powder Technology (2019)”. It discusses the morphological descriptors of SFB agglomerates and their importance for understanding the properties of the final product that influence its behavior.

3.1 Introduction

Morphology of the agglomerates is required to analyze the temporal evolution of agglomeration and to compare agglomerates formed at different operating conditions. The fractal properties (prefactor and fractal dimension), which are key characteristics of an agglomerate, usually represent compactness and arrangement of primary particles. It had been seen in the past (Brasil et al., 2001; Sorensen & Roberts, 1997) that both prefactor and fractal dimension must be properly ascertained in order to determine the structure of an agglomerate. Porosity and coordination number (CN) are other prominent morphological properties of agglomerates. Porosity is a measure of the internal pores and cavities that affects the strength and density of an agglomerate (Klobes et al., 2006). Coordination number also affects the strength of an agglomerate as it defines the connectivity of the primary particles with each other.

The morphological aspects considered in this work are mainly characterized by means of the following scalar descriptors:

- Number of primary particles in an agglomerate
- Radius of gyration
- Porosity
- Fractal dimension
- Prefactor
- Coordination number

3.2 Number of primary particles in an agglomerate

The most important way to describe an agglomerate is to denote the number of primary particles that form this agglomerate. It is also the primary step in the evaluation of other morphological descriptors of the agglomerate. For example, when

calculating the radius of gyration, knowing the number of primary particles simplifies the assessment. Traditionally, the number of primary particles in an agglomerate has been evaluated by scaling the projected area of the agglomerate (Medalia, 1967), its mobility radius (Meakin, 1987) or radius of gyration (Mandelbrot, 1992). Processing techniques of μ CT and Camsizer images helped to precisely count spherical (Dadkhah, 2014) or irregular (Pashminehazar et al., 2016) primary particles in an agglomerate.

3.3 Center of gravity

Center of gravity is the mean location of gravitational force acting on a body. For a body of distributed mass, center of gravity is the mean location of all mass in the body. The center of gravity of an agglomerate that is built of primary particles of equal density is calculated by treating the discrete masses of the primary particles as separate objects. The position vector of the center of gravity is

$$R_{CG} = \frac{\sum_{i=1}^{N_p} M_i R_i}{\sum_{i=1}^{N_p} M_i}, \quad (3.1)$$

where M_i and R_i are the mass and position vector of the primary particle i as seen in Fig. 3.1. Center of gravity is required in further calculation of radius of gyration.

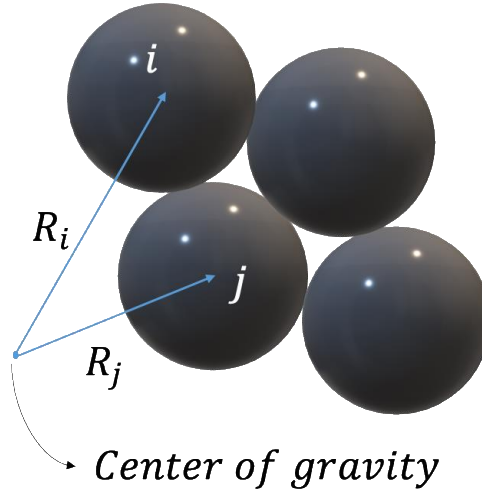


Fig. 3.1: Position vectors to calculate the radius of gyration.

3.4 Radius of gyration

Radius of gyration (R_g) is one of the principal properties to characterize an agglomerate. It is the radius at which the entire mass of the body would have the same moment of inertia as the original object (Dadkhah et al., 2012). Consequently, the radius of gyration describes the size of an object as it shows how the mass is distributed around the center of gravity. The radius of gyration of an assembly of monodisperse spheres with respect to a point is calculated as

$$R_g = \sqrt{\frac{I_m}{M}} = \sqrt{\frac{1}{N_p} \sum_{i=1}^{N_p} R_i^2} = \sqrt{\frac{1}{2N_p^2} \sum_{i=1}^{N_p} \sum_{j=1}^{N_p} (R_i - R_j)^2}, \quad (3.2)$$

where

$$I_m = \int_0^{R_e} R^2 dM = \int_0^{R_e} R^2 \rho dV = \int_0^{R_e} 4\pi R^4 \rho dR = \frac{4\pi R_e^5 \rho}{5}, \quad (3.3)$$

and

$$M = \frac{4\pi R_e^3 \rho}{3}, \quad (3.4)$$

Here, I_m is the moment of inertia, R_i and R_j are the position vectors of the i^{th} and j^{th} primary particles from the center of gravity as seen in Fig. 3.1 and N_p is the number of primary particles in the agglomerate.

3.5 Porosity

Porosity is defined as the ratio of volume of voids to the total volume occupied by an assembly of packed particles. It measures the volume fraction of internal pores as cavities or channels connected with body's surface. It is an important parameter to characterize the packing of particles. Porosity affects the effective density (Baric et al., 2019) and can influence the mechanical strength of agglomerates (Rumpf & Schubert, 1974). It is also widely used as an index of flowability of dry cohesive powders (Deng et al., 2016). Porosity of an agglomerate is expressed as

$$\varepsilon_{agg} = 1 - \frac{1}{V} \sum_{i=1}^{N_p} V_i, \quad (3.5)$$

where V is the total volume of the agglomerate and V_i is the volume of individual primary particles in it.

3.5.1 Porosity from the radius of gyration

In this method the radius of gyration of an agglomerate is calculated and the volume of the agglomerate is set equal to the volume of an equivalent sphere with the

radius R_e , which is calculated by inserting the value of I_m from Eq. (3.3) and M from Eq. (3.4) in Eq. (3.2),

$$R_e = \sqrt{\frac{5}{3}} R_g. \quad (3.6)$$

3.5.2 Porosity from convex hull

The convex hull of a certain structure is by definition the smallest convex region containing the structure. After the convex hull has been computed, the volume within it is set equal to the total volume of the agglomerate to calculate porosity using Eq. (3.5).

3.5.3 Comparison of different porosity evaluation methods

The estimation of the volume of the agglomerate from the different routes results in different porosity of the agglomerate. The variation of porosity assessed by the two different methods for an agglomerate with 100 primary particles generated by the TSA model (described in detail in Chapter 4) is shown in Fig. 3.2.

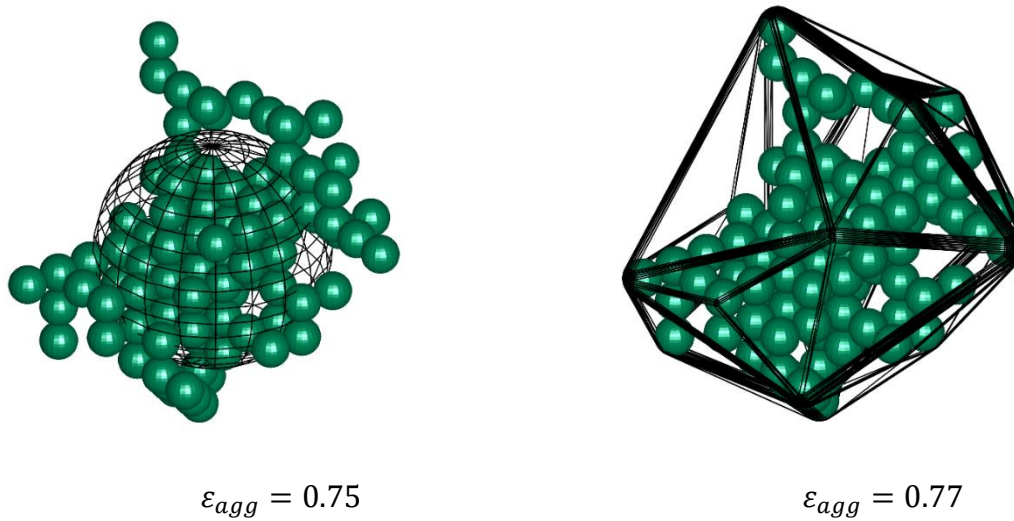


Fig. 3.2: Porosity calculated for a computer-generated agglomerate using the gyration method (left) and the convex hull method (right).

3.6 Fractal properties

Fractal properties of aggregates are defined by fractal dimension (D_f) and prefactor (k). Fractal dimension and prefactor of a large number of agglomerates are usually determined by least squares regression fitting to a power law relationship which correlates the number of primary particles of the agglomerates, N_p , with their radii of gyration, R_g , as

$$N_p = k \left(\frac{R_g}{R_p} \right)^{D_f}. \quad (3.7)$$

Here, R_p is the radius of primary particles. An illustration is provided in Fig. 3.3. Agglomerates in this chapter have been generated using the tunable sequential aggregation (TSA) model, which is explained in detail in Chapter 4. The slope of the plot in Fig. 3.3 is the fractal dimension of the agglomerates.

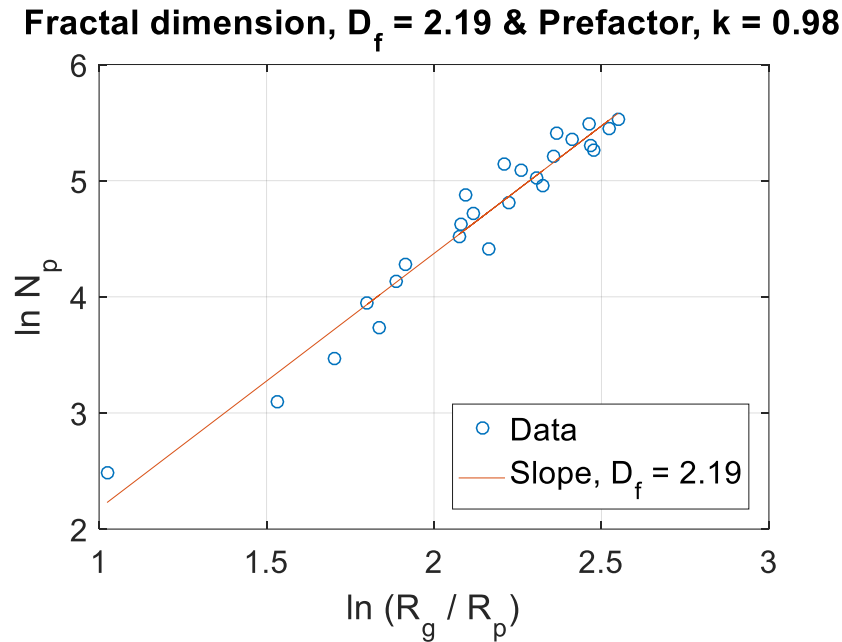
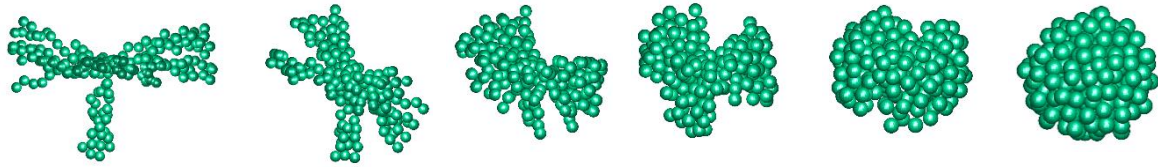


Fig. 3.3: Fractal dimension and prefactor calculation for computer-generated agglomerates by plotting the number of primary particles and the ratio of radius of gyration and primary particle radius on a double logarithmic scale.

3.6.1 Fractal dimension

Fractal dimension (D_f) provides an insight into the arrangement of particles within the agglomerate as well as the degree of compactness of agglomerates (Salman & Hounslow, 2004). It provides a quantitative measure of the degree to which a structure fills physical space beyond its topological dimension (Crowe et al., 2011). It is an important measure to determine the strength of an agglomerate. Higher D_f indicates that the structure is compact and has more inter-particle bonding which implies that the agglomerate is strong. Whereas, lower D_f indicates that the agglomerate is open and more tenuous in structure. The value of fractal dimension can vary from one (chain-like structure like in (Rong et al., 2006)) to three (spherical agglomerate).

This can be perceived from Fig. 3.4 where the morphology of synthetic agglomerates (with 200 primary particles and prefactor equal to 1) is changed at different fractal dimensions. With fixed prefactor, the mean coordination number (MCN) of the agglomerates increases and porosity decreases with an increase in fractal dimension. Porosity is measured using the gyration method.



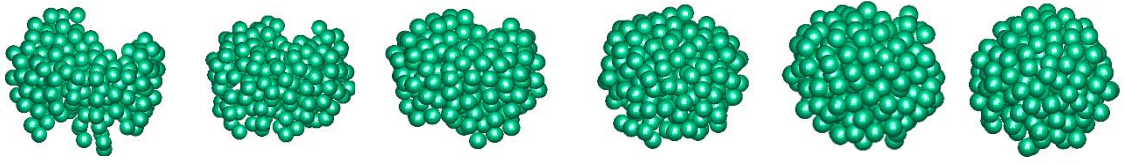
$D_f(k = 1)$	2.0	2.2	2.4	2.6	2.8	3.0
MCN	2.26	2.49	2.76	3.17	3.54	4.52
ε_{agg}	0.96	0.93	0.87	0.78	0.67	0.53

Fig. 3.4: Morphological change of agglomerates ($N_p = 200$) with the same prefactor ($k = 1$) and varying fractal dimension.

3.6.2 Prefactor

Prefactor (k) is related to the packing fraction in D_f dimensional space. It is also referred to as lacunarity (Lapuerta et al., 2009) or structure factor (Gmachowski, 1995). It is a parameter whose importance is increasingly being appreciated as a descriptor of packing of the primary particles, which indicates the local structure of an agglomerate (Wu & Friedlander, 1993). It is an essential ingredient for a complete description of a power-law agglomerate, as suggested by the scaling power law (Eq. (3.7)).

As indicated in Fig. 3.5, the fractal prefactor has an influence on the degree of compactness of agglomerates. With a fixed fractal dimension (of $D_f = 3$), if the prefactor is increased, the mean coordination number (MCN) of the agglomerate (with 200 primary particles) increases and the porosity decreases, making the agglomerates compact and strong.



$k(D_f = 3)$	0.5	0.6	0.7	0.8	0.9	1.0
MCN	3.36	3.51	3.73	3.83	4.31	4.52
ε_{agg}	0.76	0.72	0.66	0.62	0.58	0.53

Fig. 3.5: Morphological change of agglomerates ($N_p = 200$) with varying prefactor and same fractal dimension ($D_f = 3$).

3.7 Coordination number

Coordination number (CN) of a primary particle in an agglomerate is defined by the sum of all contact points that the primary particle has with surrounding primary particles. For two primary particles (i, j) with center coordinates (x, y, z) and radius (R), if the condition

$$\sqrt{(x_i - x_j)^2 + (y_i - y_j)^2 + (z_i - z_j)^2} \leq |R_i - R_j| \quad (3.8)$$

is satisfied, then they are in contact. CN is a very popular microscopic parameter associated with packing structure (Li et al., 2018). It influences the elasticity (Gaume

et al., 2017), plastic strength (Vo et al., 2017) and densification rate (Kamyabi et al., 2019).

The coordination number is somehow correlated with the packing fraction. For monodisperse spherical particles, the densest packing is that with a packing ratio (relative packing density) of $\pi/\sqrt{18} \approx 0.74$ (Hales, 1994). This maximum packing ratio of 0.74 for monodisperse spheres corresponds to the hexagonal closest packing (hcp) or the face-centered cubic (fcc) packing and its stacking variants, all with a coordination number of 12 (i.e. any selected particle has 12 closest neighbors in direct point contact). The simple cubic packing, on the other hand, has a packing ratio of 0.52 and a coordination number of 6. It is not known whether stable packings of monodisperse spheres with a lower packing ratio and coordination number exist in 3D space (diamond packing with a packing ratio of 0.34 and a coordination number of 4 is unstable). Table 3.1 lists several regular packings of monodisperse spheres.

Table 3.1. Packing fraction and coordination number of regular packings of monodispersed spheres in 3D space.

Packing type	Packing fraction	Coordination number
Closest packing (fcc/hcp)	0.741	12
Tetragonal-sphenoidal	0.708	10
Body-centered cubic	0.680	8
Orthorhombic	0.605	8
Simple cubic	0.524	6
Diamond	0.340	4

All the morphological descriptors, which have been explained in Sections 3.2 – 3.7, are scalar descriptors. A vector descriptor, namely coordination angle, is explained in Appendix A.

3.8 Interrelation and predictability of morphological descriptors

Different correlations have been developed to simplify the parameters in quantifying the morphology of the agglomerates. The various correlations between the morphological descriptors developed are discussed here.

3.8.1 Correlation of porosity as a function of fractal properties

Assuming the primary particles as monodisperse, Eq. (3.5) can be reduced to

$$\varepsilon_{agg} = 1 - \frac{N_p V_p}{V}, \quad (3.9)$$

where the volume of any primary particle is defined as

$$V_p = \frac{4\pi R_p^3}{3}. \quad (3.10)$$

The volume of the agglomerate can be set equal to the volume of the equivalent sphere with radius R_e

$$V = \frac{4\pi R_e^3}{3}. \quad (3.11)$$

Substituting the radius of equivalent sphere, R_e , from Eq. (3.6) in Eq. (3.11), Eq. (3.9) becomes

$$\varepsilon_{agg} = 1 - N_p \left(\frac{R_p}{R_e} \right)^3. \quad (3.12)$$

Using the power law relationship from Eq. (3.7) in Eq. (3.12), the porosity is articulated as a function of D_f , k and N_p ,

$$\varepsilon_{agg} = 1 - 0.465 N_p \left(\frac{k}{N_p} \right)^{3/D_f}. \quad (3.13)$$

The underlying assumptions for the above correlation are as follows:

- Primary particles are monodispersed.
- Radius of gyration is used to predict the equivalent radius of an agglomerate.

Agglomerate diameter ($D_{agg} = 2R_e$) can be correlated to porosity by rearranging Eq. (3.12). With $D_p = 2R_p$ it is obtained:

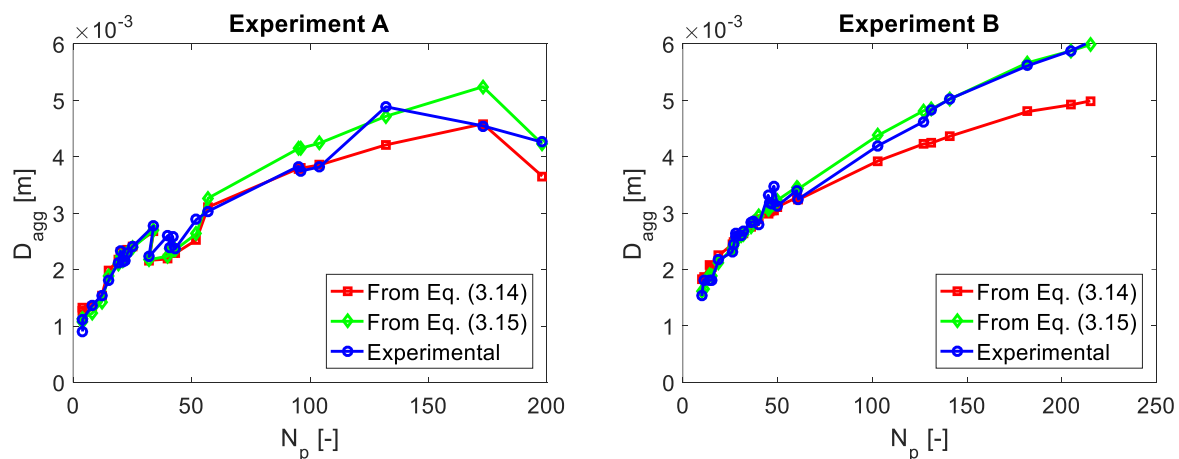
$$D_{agg} = \left[\frac{N_p D_p^3}{1 - \varepsilon_{agg}} \right]^{1/3}. \quad (3.14)$$

Inserting the porosity expression from Eq. (3.13) in the above equation, agglomerate diameter is finally

$$D_{agg} = 1.291 \times D_p \left(\frac{N_p}{k} \right)^{1/D_f}. \quad (3.15)$$

In order to validate the underlying assumptions for the above correlations of porosity and agglomerate diameter, the experimental findings from (Dadkhah & Tsotsas, 2014) are used. These experiments were performed in batch mode with glass beads as primary particles and HPMC in aqueous solution as a binder. A brief description of the experiments, as well as of the examined and experimentally obtained morphological descriptors is given in Appendix B.

On the one hand, agglomerate diameter is calculated using Eq. (3.14), where porosity is assumed to be the averaged porosity of the batch (Table B.2) whereas N_p and D_p ($= 2R_p$) are taken for each individual agglomerate (i.e. from data like those of Tables B.3-B.8 in Appendix B for respective experiments A to F). On the other hand, agglomerate diameter is calculated using Eq. (3.15), with D_f and k from Table B.2 and D_p , again, for each individual agglomerate. From the plots for different trials from (Dadkhah & Tsotsas, 2014) at varying process parameters in Fig. 3.6 it is clear that the agreement between experimental results and the new formulation of agglomerate diameter according to Eq. (3.15) is closest when the standard deviation of primary particle radius (last row of Table B.2) is smallest. This is the case for Exp. B and Exp. F.



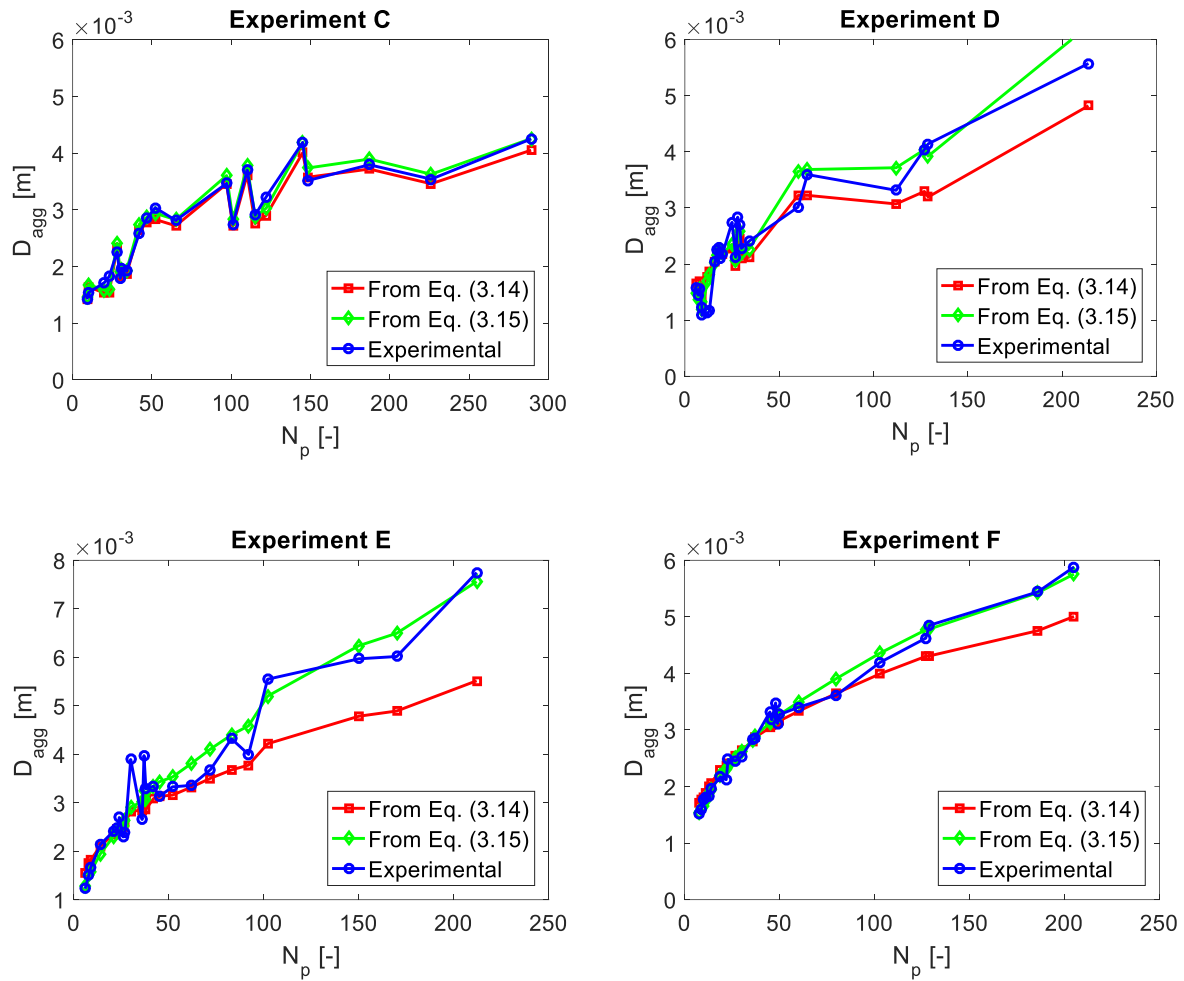


Fig. 3.6: Different ways to obtain agglomerate diameter from the number and size of primary particles (Eq. (3.14): via agglomerate porosity, Eq. (3.15): via fractal properties) in comparison to experimental results.

Agglomerate diameters obtained from Eq. (3.15) are compared to experimental results for all six experiments conducted by Dadkhah (Dadkhah & Tsotsas, 2014) in the parity plot of Fig. 3.7. Slopes and degrees of regression are close to unity for all the trials, which validates the new correlation for agglomerate size according to Eq. (3.15). Best fit is obtained for Exp. B and Exp. F. As already pointed out, it is believed that this is

due to best fulfillment of the underlying assumption about monodispersed primary particles in those two trials.

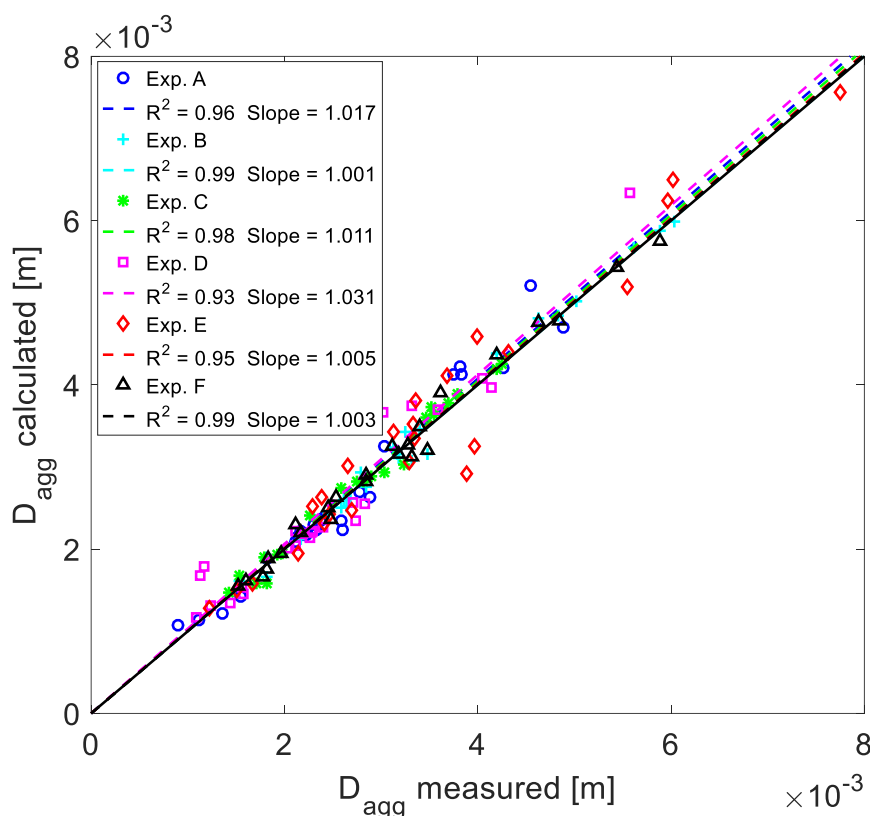


Fig. 3.7: Parity plot of agglomerate diameter obtained from Eq. (3.15) resp. measured for all six experiments.

Porosity of an agglomerate is formulated in Eq. (3.13) as a function of fractal dimension, prefactor, and the number of primary particles in the agglomerate. This formulation was also used to study the mechanical properties and morphological features of nanoparticle agglomerates (Deng et al., 2016). A decrease in porosity is observed with increasing prefactor keeping a fixed fractal dimension and number of primary particles in Fig. 3.8. Since the prefactor is usually less than the number of primary particles, the expression $(\frac{k}{N_p})$ is less than one in Eq. (3.13) and the exponent is greater than one as the value of D_f is always less than three. So, increasing the fractal

dimension leads to a decrease in the porosity for a fixed prefactor and number of primary particles, as exemplarily shown for $k = 1$ in Fig. 3.8.

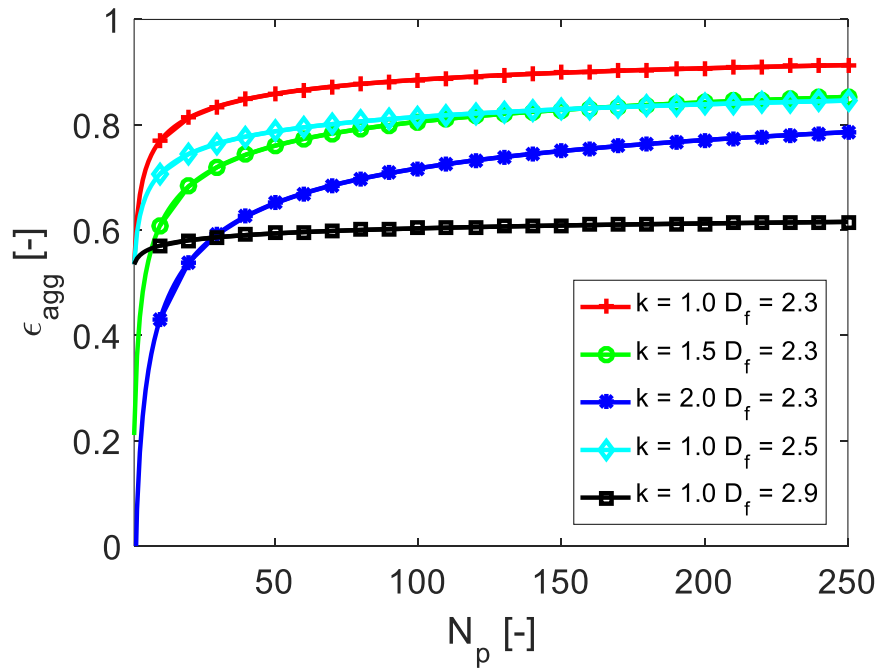


Fig. 3.8: Porosity of agglomerates along the number of primary particles present in the agglomerates with varying fractal dimension and prefactor.

The overall conclusion is that the porosity of an agglomerate decreases with an increase in its fractal dimension and prefactor, depending on those two quantities and on the number of primary particles in the agglomerate,

$$\varepsilon_{agg} = f(N_p, D_f, k). \quad (3.16)$$

3.8.2 Correlation between fractal properties

The porosity of an agglomerate is a function of its fractal dimension and prefactor, and the number of primary particles in the agglomerate. Any equation of this type (Eq. 3.16) would be reduced to just two influencing parameters (N_p, D_f) and simplified if the prefactor could be correlated with the fractal dimension. Therefore, various empirical correlations of this kind have been proposed for aggregates formed by experimental aggregation processes or simulated by aggregation models (Table 3.2).

Table 3.2. Prefactor correlations from various researchers.

$k = 0.414 \times D_f - 0.211$	(Vanni, 2000)
$k = \left(\sqrt{1.56 - \left(1.728 - \frac{D_f}{2}\right)^2} - 0.228 \right)^{D_f} \left(\frac{D_f+2}{D_f} \right)^{D_f/2}$	(Gmachowski, 2002)
$k = 0.7321 + 0.8612 \left(\frac{D_f-1}{2} \right)^{1.95}$	(Lapuerta et al., 2006)
$k = 4.46 \times D_f^{-2.08}$	(Ehrl et al., 2009)
$k = 5.323 - 1.4802D_f$	(Present work, Singh & Tsotsas, 2019)

Gmachowski (Gmachowski, 2002) used the ratio of the hydrodynamic to the geometric radius of aggregates to deduce the relation of fractal dimension and prefactor. A generalized curve was provided for values from different aggregation models (detailed descriptions in Chapter 4) and experimental values of various researchers. Lapuerta (Lapuerta et al., 2006) gave in a study of diesel soot agglomerates a relation between fractal dimension and the prefactor by considering the boundary conditions as the packing fraction of particles in different lattice

arrangements. Ehrl (Ehrl et al., 2009) generated and analyzed geometrically dense clusters with variable fractal dimension, composed of rigid monodisperse primary particles, to present a power law relation between fractal dimension and prefactor. In the present work, an empirical correlation has been generated from the set of experimental values of fractal dimension and prefactor in Table B.2. This is

$$k = f(D_f) = 5.323 - 1.4802D_f. \quad (3.17)$$

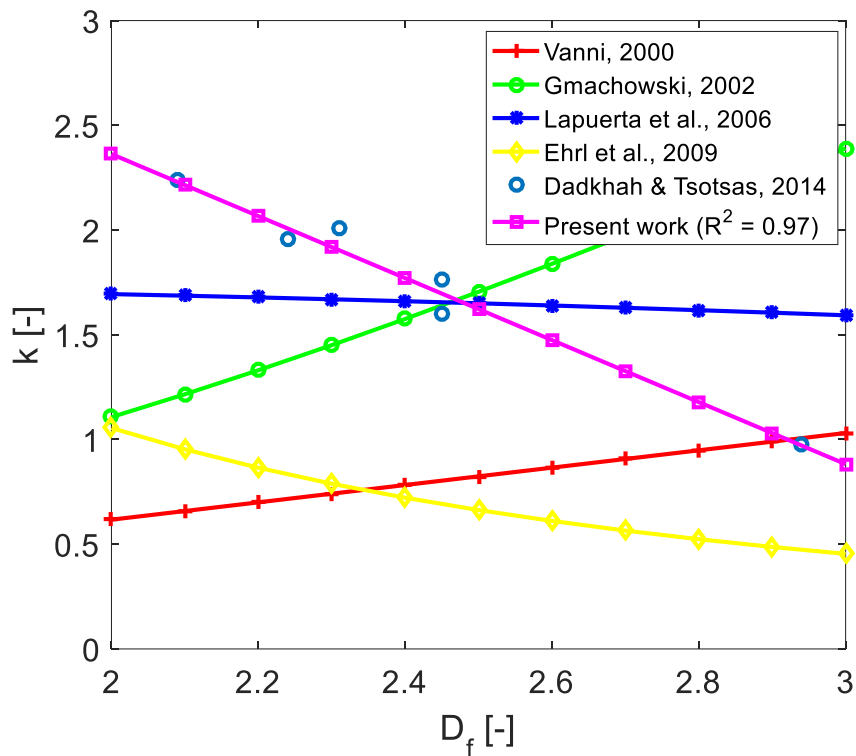


Fig. 3.9: Correlation between prefactor and fractal dimension, compared with spray fluidized bed data from (Dadkhah & Tsotsas, 2014) and with Eq. (3.17).

Figure 3.9 shows that the correlations of Gmachowski (Gmachowski, 2002) and Vanni (Vanni, 2000) are similar in that they predict the prefactor to increase with increasing fractal dimension. This in turn contradicts the pattern followed by spray fluidized bed agglomerates in (Dadkhah & Tsotsas, 2014) (Table B.2). The correlations of Lapuerta

(Lapuerta et al., 2006) and Ehrl (Ehrl et al., 2009) follow the same trend of spray fluidized bed agglomerates but don't meet the values. Trend and values can only be described by the newly developed correlation (Eq. (3.17)).

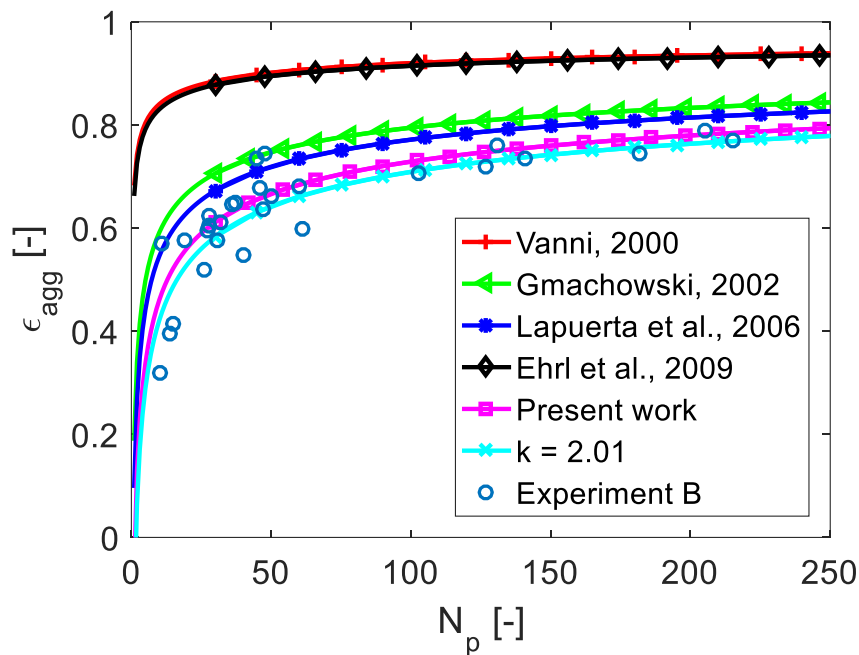


Fig. 3.10: Agglomerate porosity according to different correlations of prefactor, k , for Exp. B.

Porosity calculated from Eq. (3.13) by using different prefactor correlations from Table 3.2 while keeping fractal dimension at the value measured for experiment B ($D_f = 2.31$, see Table B.2) is plotted in Fig. 3.10. The porosity calculated by the prefactor correlations of Vanni and Ehrl is very high, leading to very porous agglomerates. Porosity from the correlations by Lapuerta and Gmachowski is better comparable to the experimental results from (Dadkhah & Tsotsas, 2014), though still too high. Use of Eq. (3.17) in Eq. (3.13) meets the measured data almost equally well as the use of prefactor obtained directly from the measurement ($k = 2.01$ for Exp. B, see Table B.2).

In general, use of Eq. (3.17) reduces the number of parameters that need to be known in order to predict agglomerate size from the number of primary particles to just one (namely the fractal dimension).

3.9 Modified Monte Carlo model (CVMC-1)

In the CVMC models to be discussed and compared in this section, the process conditions and material properties are taken same as in the experiments from (Dadkhah & Tsotsas, 2014) (Table B.1). Glass beads have been used as the primary particles in trials A to E of this experimental investigation, and HPMC has been the binder for the agglomeration process. The simulation box, containing monodispersed primary particles, is considered as representative for the overall agglomeration process. A scheme of the CVMC approach is given in Fig. 3.11.

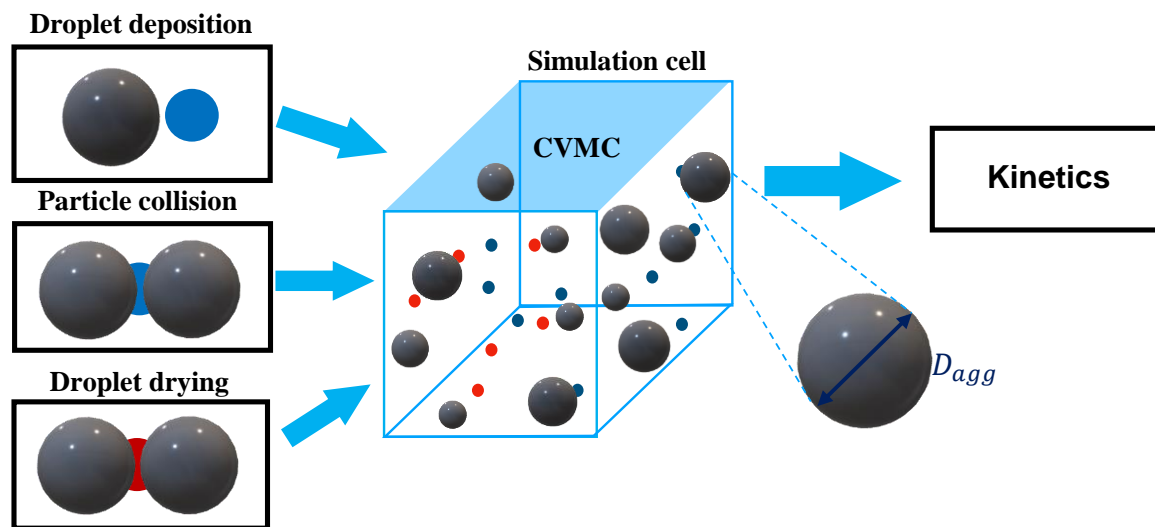


Fig. 3.11: Simplified diagram of the CVMC algorithm used in the present work.

Particles are added periodically to the simulation box, when the total number of particles becomes half of its initial value. The time step is computed according to the

collision event from the collision frequency, f_{coll} (Buffière & Moletta, 2000). More details on the CVMC model are given in Chapter 2.

During each time step of the CVMC, collisions between randomly chosen pairs of particles take place and a decision about successful or unsuccessful agglomeration is made for each collision based on whether the following conditions are fulfilled, or not:

- i. the collision is a wet collision;
- ii. particles strike at wet position/s;
- iii. the so-called Stokes criterion for coalescence is fulfilled (Adetayo & Ennis, 1997).

If the above-mentioned conditions are satisfied, then the colliding particles form a new agglomerate. For simplicity, each formed agglomerate is represented by a sphere having porosity equal to the porosity of the agglomerate. Where this agglomerate porosity is taken from, distinguishes the models to be compared from each other.

In the **old model**, developed by Terrazas (Terrazas-Velarde et al., 2009), Eq. (3.14) is used to get the agglomerate diameter with a constant porosity value of $\varepsilon_{agg} = 0.6$. This means that the agglomerates formed are assumed to have the same porosity irrespective of their size and the change in the process parameters. To implement the structural change, the old model is modified to the **CVMC-1 model** by calculating variable values of porosity from Eq. (3.13).

Correspondingly, agglomerate diameter is obtained as a function of fractal dimension and prefactor from Eq. (3.15). This means that fractal dimension and prefactor are replacing porosity in the new model in determining the agglomerate diameter. Concerning the data of Dadkhah (Dadkhah et al., 2012) fractal dimension from Table B.2 can be correlated empirically with external parameters (namely inlet temperature of the fluidizing gas, T_g in °C, and the mass fraction of the liquid binder, x_b) to obtain

$$D_f = (0.0105 \times T_g) - (0.067 \times x_b) + 2.13. \quad (3.18)$$

Accordingly, the new MC model (CVMC-1) incorporates the change in agglomerate diameter with the change in operating parameters of the agglomeration process, whereas the old model did not. The value of prefactor is obtained from the empirical correlation derived from the experimental results, i.e. from Eq. (3.17). This decreases the number of parameters necessary in order to determine the agglomerate diameter from the number of primary particles to just one, namely the fractal dimension.

3.10 Model sensitivity to variation of the initial number of primary particles

The simulation box, which is considered as a representative sample of the particle population, consists of an initial number of primary particles ($N_{p,0,box}$). It has no geometric dimension. In order to investigate the effect of the initial number of primary particles in the simulation box on the accuracy of the CVMC model, a series of simulations has been performed. The simulations were performed for 5 minutes by means of the CVMC-1 model. The simulations use same experimental, from Table B.1 (Dadkhah, 2014), and model parameters given in Table 3.4, corresponding to Exp. A, under exactly the same conditions, with the initial number of primary particles varying between 100 and 10000.

Table 3.4. Simulation parameters.

Bed mass	M_{bed}	500	g
Primary particle diameter	D_p	0.52	mm
Primary particle density	ρ_p	2500	kg/m ³
Particle surface asperities height	h_a	10	μm
Particle restitution coefficient	e	0.8	-
Droplet diameter	D_d	80	μm
Droplet addition rate	γ	0.08	1/s
Particle-droplet contact angle	θ	40	°
Positions on the primary particle surface	N_{pos}	48	-
Fluidization velocity	u_0	1.912	m/s
Gas (dry) mass flow rate	\dot{M}_g	130	kg/h
Moisture content in the gas	Y_g	3.4	g/kg

The accuracy (measured as standard deviation of particle size distribution at the end of simulation) of the CVMC model, 95 % confidence spread of final agglomerate diameter and computation time (on a usual personal computer with 4 cores; 3.4 GHz processor and 4 GB RAM) required in each case for one realization of the CVMC simulation at different initial number of primary particles are noted in Table 3.5. To quantify the standard deviation and computation time for each case, the case with 1000 primary particles was taken as a reference, where $\sigma(N_{p,0,box} = 1000) = 183 \mu\text{m}$ and $t_{CPU}(N_{p,0,box} = 1000) = 180 \text{ min}$ to reach the real-time of 5 min, in Table 3.5. In general, it is expected that the accuracy of the CVMC model is improved by increasing the initial number of primary particles in the simulation box. However, this improvement always takes place at the expense of simulation speed.

Table 3.5. Effect of the number of simulated particles on the model accuracy and on the simulation speed.

$N_{p,0,box}$ [-]	95 % confidence spread [mm]	$\frac{\sigma(N_{p,0,box})}{\sigma(N_{p,0,box}=1000)}$ [-]	$\frac{t_{CPU}(N_{p,0,box})}{t_{CPU}(N_{p,0,box}=1000)}$ [-]
100	[0.717 0.831]	1.434	0.045
200	[0.648 0.723]	1.115	0.096
500	[0.643 0.686]	1.062	0.313
1000	[0.642 0.671]	1.000	1.000
2000	[0.648 0.668]	0.997	4.113
5000	[0.648 0.662]	0.976	32.40
10000	[0.649 0.658]	0.957	125.4

The results of the CVMC simulations are shown in Fig. 3.12. As expected, all simulation results fluctuate to a certain degree, with the largest standard deviation of agglomerate diameter being observed for 100 primary particles. As far as the simulation time is concerned, it increases with increasing number of primary particles, especially for 10000 primary particles being most. On the other hand, no significant change in the accuracy is observed for the cases after the reference case with 1000 primary particles. This shows that a simulation box with 1000 to 2000 initial primary particles can be regarded as optimal for the CVMC model. The same was concluded by Terrazas (Terrazas-Velarde et al., 2009). Compromising between accuracy and computation time, 1000 initial primary particles have been used in the present work, cf. (Singh & Tsotsas, 2019, 2020).

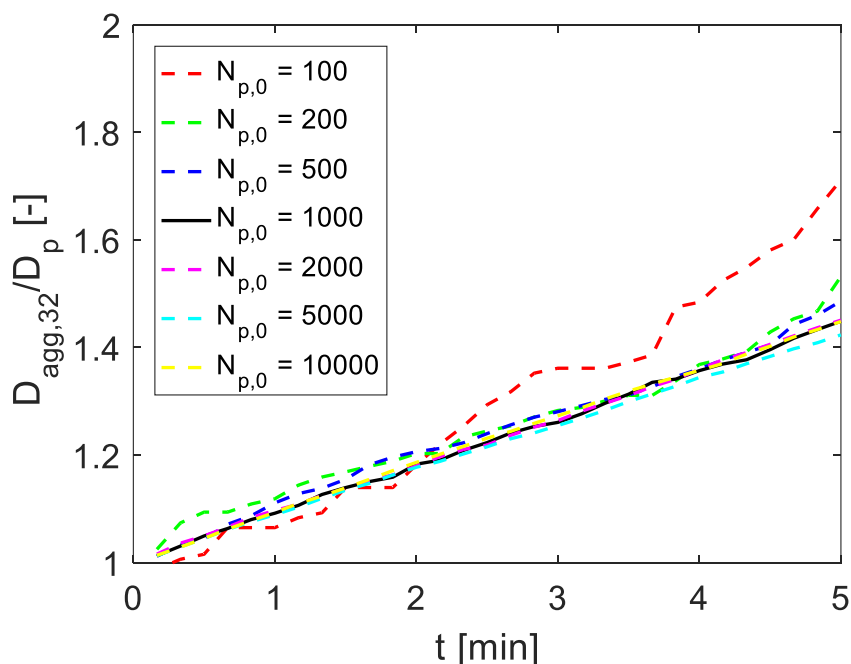


Fig. 3.12: Effect of the initial number of primary particles in the simulation box.

All further simulations have been performed with an initial number of primary particles of $N_{p,0} = 1000$.

3.11 Comparison of the old model and the modified MC (CVMC-1) model

Simulations have been carried out for all the experiments from Table B.2, especially for Exp. A to Exp. E with glass beads as the primary particles, by means of the old and the CVMC-1 model for 5 mins. Contrary to (Terrazas-Velarde et al., 2009), the breakage mechanism is not considered in the present simulations with either model. The purpose of this is to first concentrate on the influence of the morphology on growth. Breakage will be the subject of a separate chapter (Chapter 6). Simulation parameters corresponding to the experimental parameters have been presented in Table B.1; additional parameters are summarized in Table 3.4.

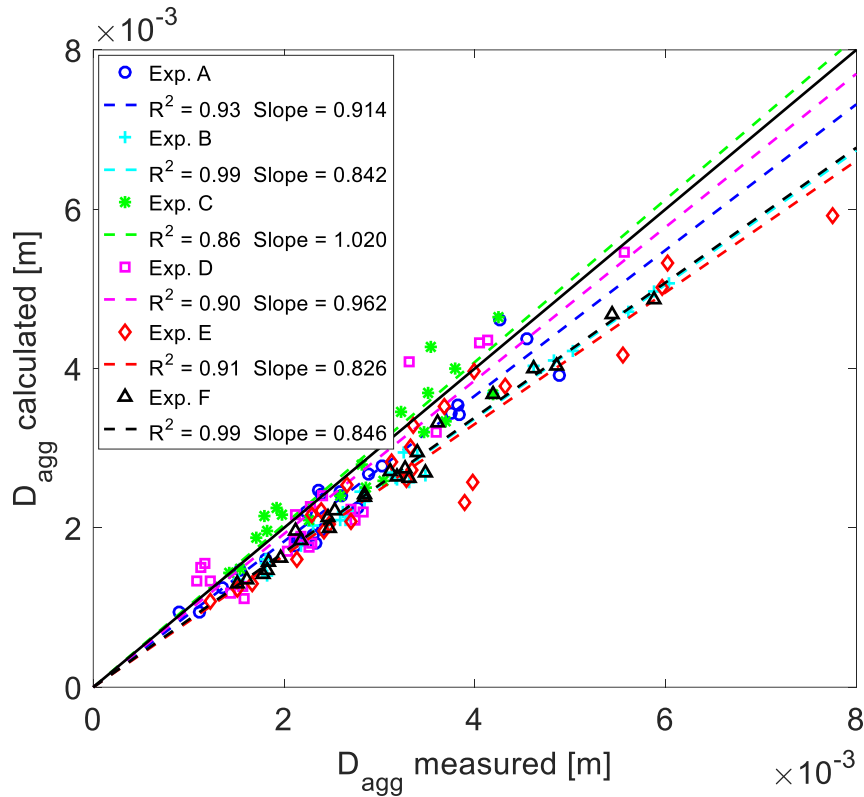


Fig. 3.13: Parity plot with average primary particle diameter of 0.52 mm, otherwise same as that of Fig. 3.7.

One important aspect of Table B.2 is that the diameter of the primary particles is taken as 0.52 mm. This is the average size of primary particles used by (Dadkhah et al., 2012), as separately measured by particle projection images (Camsizer). The corresponding radius of $R_p = 0.26$ mm differs from the primary particle radii for individual agglomerates; being smaller than them especially for Exp. B and Exp. E (cf. ranges of R_p in Table B.2). This means that the consistency of the morphological features reflected in the parity plot of Fig. 3.7 cannot be preserved with the same quality when evaluating with $R_p = 0.26$ mm throughout. Indeed, agglomerate diameter is underpredicted for most trials in Fig. 3.13, by up to around 15% (slopes less than unity).

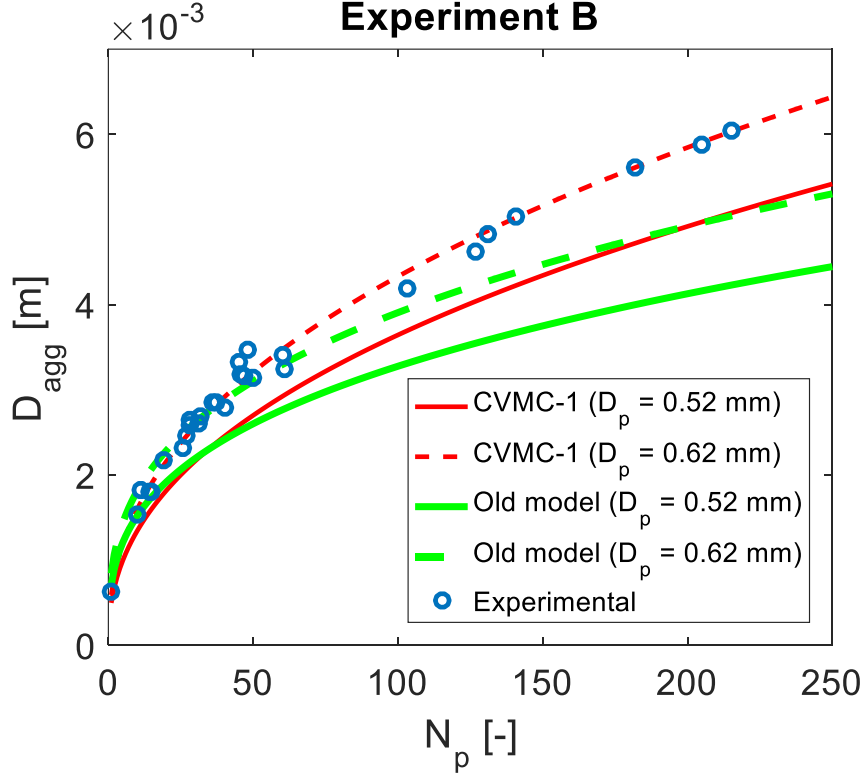


Fig. 3.14: MC simulation results with constant porosity (old model) and porosity correlation (CVMC-1) for $D_p = 0.62$ mm (average over individual experiment) and $D_p = 0.52$ mm (average over all experiments) in comparison with experimental results.

Results from Exp. B are not captured very well in Fig. 3.13, because $R_p = 0.26$ mm is below the range of primary particles sizes observed in the agglomerates analyzed from the specific trial (Table B.2). Agglomerate sizes from Exp. B for different numbers of primary particles, N_p , and different primary particle diameters, D_p , are compared in Fig. 3.14 with predictions of the old model (from Eq. (3.14) with $\varepsilon_{agg} = 0.6$) and of the new model (from Eq. (3.15) with D_f from Eq. (3.18) and k from Eq. (3.17)). It can be seen that predictions of the CVMC-1 model differ significantly from those of old model. Specifically, the old model overestimates in comparison to the CVMC-1 model agglomerate size for small agglomerates (N_p less than around 50), whereas it increasingly underestimates the size of large agglomerates ($N_p > 50$).

3.11.1 Agglomerate kinetics

Time does not appear in Fig. 3.13 or Fig. 3.14, but it is an important factor in Fig. 3.15 and in Table 3.6. In Fig. 3.15, the time evolution of the relative agglomerate diameter at different inlet temperatures and binder concentrations is compared using the old model (with porosity equal to 0.6) and the modified (CVMC-1) model (with variable porosity).

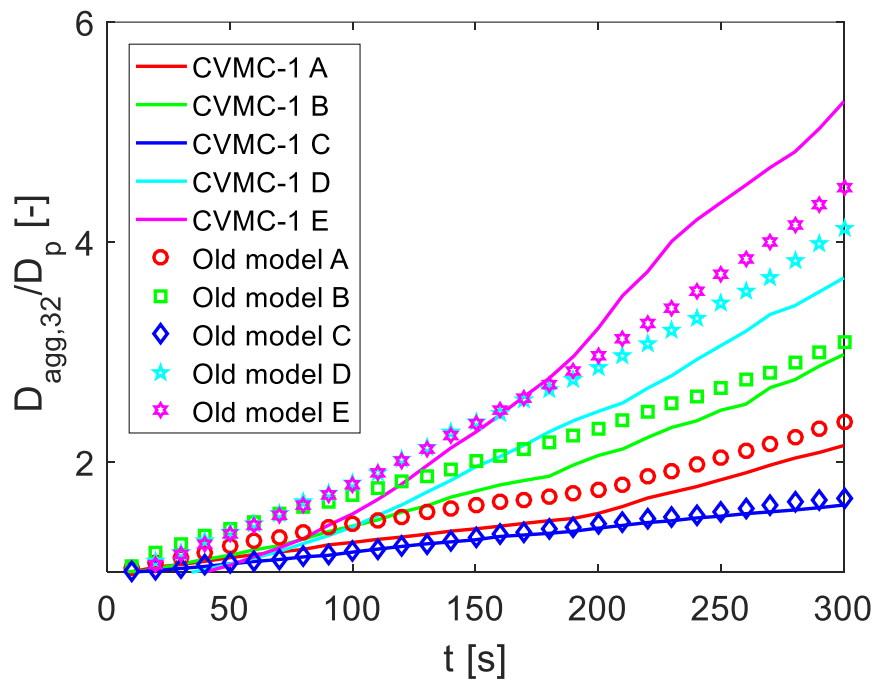


Fig. 3.15: Agglomerate relative diameter with respect to the time using different MC models for different experiments.

The relative diameter of the agglomerates is the ratio of Sauter mean diameter of the population and the initial diameter (equal to $D_p = 0.52$ mm) at a given instant of time. In Table 3.6, the overall growth rate is defined as the ratio of the difference between Sauter mean diameter of the final agglomerates at the end of the process and the diameter of primary particles to the duration of the trial (i.e. 300 s),

$$r_G = \frac{D_{agg,32,t} - D_p}{t}. \quad (3.19)$$

With its help, kinetics of the process at different temperatures (Exp. B, A and C with increasing temperature) and binder concentrations (Exp. A, D and E with increasing concentration) is expressed.

Table 3.6. The overall growth rate for different experiments and respective simulations by both models after 300 s.

Trial	Overall growth rate ($\mu\text{m/s}$)				
	A	B	C	D	E
CVMC-1	1.79	2.92	1.23	4.47	6.82
Old model	1.96	3.72	1.69	5.52	6.12
Experiment	1.07	1.15	0.63	3.79	8.20

Table 3.6 shows that the estimated kinetics (overall agglomerate growth rate) of the agglomeration process is overestimated for most of the experiments (except for the case of Exp. E) by both models. This is due to the fact that the breakage of agglomerates has not been considered in the models. Consideration of breakage in further work might be accompanied by the reconsideration of the model parameters (Table 3.4), which have just been taken over without any tuning from (Terrazas-Velarde et al., 2009) for the present discussion. In the frame of this discussion it is important to note that the old model is overestimating the growth rate for all the experiments, except Exp. E, in Table 3.6. This overestimation is notable, though not dramatic. It is due to the fact that relatively small agglomerates ($N_p < 50$) are considered in Table 3.6, which are predicted to be larger with the old model than with the CVMC-1 model (Fig. 3.14). Since it depends on agglomerate size and agglomeration progress, this result cannot be generalized and may turn to the exactly opposite behavior.

3.11.2 Agglomerate morphology

The diameters of agglomerates with respect to their numbers of primary particles for different models are plotted in Fig. 3.16. Due to constant porosity of $\varepsilon_{agg} = 0.6$ in Eq. (3.14), agglomerates formed with the same number of primary particles have the same diameter if simulated using the old model, irrespectively of different process parameters. However, morphological change is captured in the CVMC-1 model by predicting different diameter of formed agglomerates with the same number of primary particles at different experimental conditions. With an increase of inlet gas temperature, corresponding to experiments B, A and C at 30°C, 60°C and 90°C respectively, the agglomerates become compact because the fractal dimension increases and the size (diameter) decreases.

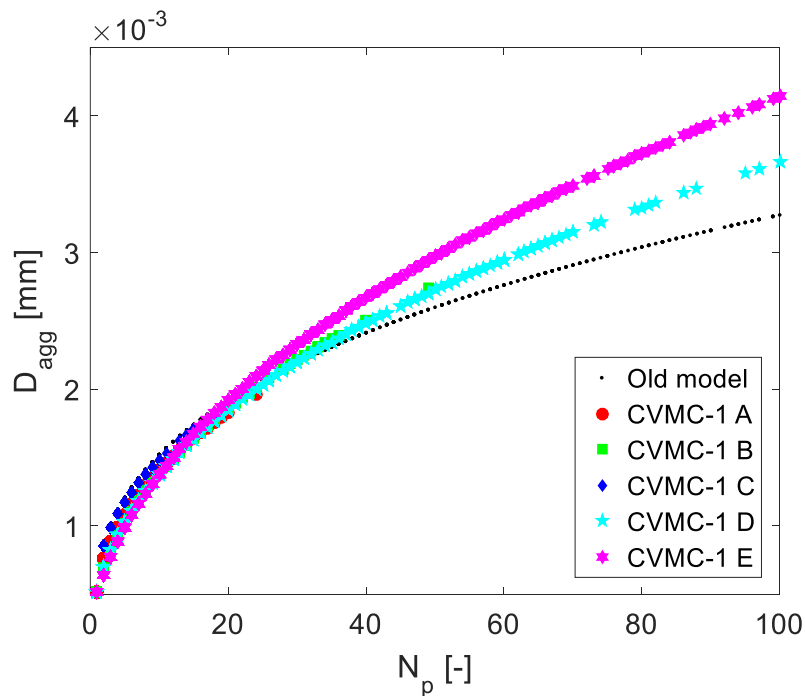


Fig. 3.16: Agglomerate diameter with respect to the number of primary particles using different MC models for different experiments.

Contrarily, as the mass fraction of the binder increases, corresponding to experiments A, D and E, fractal dimension of the agglomerates decreases. Consequently, the agglomerates become branched and porous and their size (diameter) increases. Such effects can be captured when using the CVMC-1 model (Fig. 3.16) by just correlating the fractal dimension to operating conditions of the agglomeration process (Eq. (3.18)).

3.12 Conclusion

This chapter discussed morphological descriptors of spray fluidized bed agglomerates and formulated a cross-correlation between them. Dadkhah (Dadkhah et al., 2012) did not check the consistency of the morphological descriptors that she measured, i.e. of average porosity and agglomerate size on one, and fractal dimension and prefactor on the other side. This has been done in the present chapter to show that the morphological data from (Dadkhah et al., 2012) are consistent. It has been shown that agglomerate size can be more accurately predicted from the number of primary particles by known fractal dimension and prefactor of an agglomerate sample, than by known average porosity of the agglomerates of the same sample. The clarity in the consistency of the morphological data and in the superiority of the approach that is based on the fractal properties seems to be reduced for morphological data evaluated by assuming monodispersed primary particles with increasing deviation from this assumption. Increased attention should be given in the future to the size distribution of primary particles, as recently also indicated by (Pashminehazar et al., 2016).

It has moreover been shown that the fractal dimension can be clearly correlated with the prefactor for the agglomerates produced by (Dadkhah et al., 2012). This reduces the number of parameters that need to be known in order to predict agglomerate size from the number of primary particles to just one (namely the fractal dimension). The correlation developed for fractal dimension and prefactor lies in the region of other correlations presented in the literature to this purpose, but there are also differences

in values and trends among literature correlations as well as in their comparison to the new correlation. This issue is still not well understood.

The cross-correlation between the morphological descriptors to predict agglomerate size is used in the MC model to incorporate the morphological change with respect to different experimental parameters. The new MC model (denoted by CVMC-1) predicts reasonably the kinetics and the temporal change in the morphology of the agglomerates. The size (diameter) of the agglomerates with the same number of primary particles changes with the change in the operating parameters of the agglomeration process rather than being constant (old model).

Chapter 4 Aggregation model

This chapter is a modified version of the paper “A tunable aggregation model incorporated in Monte Carlo simulations of spray fluidized bed agglomeration, Powder Technology (2020)”. It gives an overview of various aggregation models and their limitations with respect to spray fluidized bed agglomerates.

4.1 Introduction

Particle aggregation is the process by which individual particles or small clusters combine with each other to form big clusters. The aggregates are generally constituted of identical spherical particles. Computer models for the growth of these clusters are useful tools for the understanding of aggregation phenomena. The main contribution of such models is to provide pathways to investigate the underlying physical ingredients ruling the properties observed in growth phenomena (Alves et al., 2008).

In general, every aggregate formation starts with a single seed particle. Aggregate growth is then accomplished by adding other spherical primary particles to the seed particle (Ball & Witten, 1984). Such a scheme may also be easily realized in a computer simulation using Monte Carlo methods. They are important tools to understand the growth of clusters (Meakin, 1999).

4.2 General classification

Basically, parameters that can be varied to achieve different types of aggregation models can be assigned to four groups (Kätzler et al., 2008), as they refer to aggregate formation, particle trajectories, the simulation lattice or algorithm tuning.

Aggregate formation occurs, as illustrated in Fig. 4.1, either through particle-cluster aggregation, where only one primary particle is added each time to an existing aggregate, or through cluster-cluster aggregation, which means that even two clusters may be added to a new cluster.

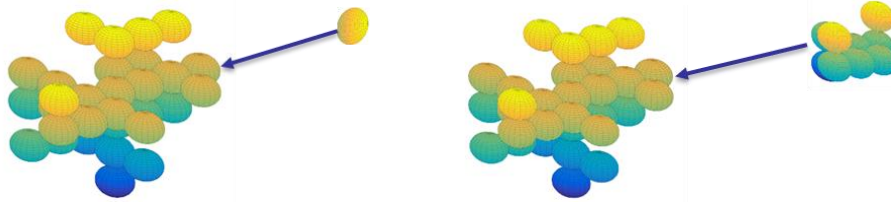


Fig. 4.1: Particle-cluster aggregation (left) and cluster-cluster aggregation (right).

Particle trajectories are composed by the movements that entities (primary particles or small clusters) undergo in the working lattice until they can stick to the main cluster and form an aggregate (Dirkse & Cawley, 1995). The entities may take a path that consists of many linear pieces or is linear over the whole distance. Erratic, multi-step trajectories are usually obtained by a random walk in all six directions, while the considered entity gets closer to the main cluster in order to form an aggregate. Aggregates are formed by such trajectories in the diffusion-limited aggregation (DLA) model (Witten & Sander, 1981), which is described in detail in (Meakin, 1983). Alternatively, entities may follow an uninterrupted linear trajectory over the entire distance to the main cluster in order to form an aggregate. This type of model is termed as ballistic aggregation model and is described in detail in (Vold, 1963).

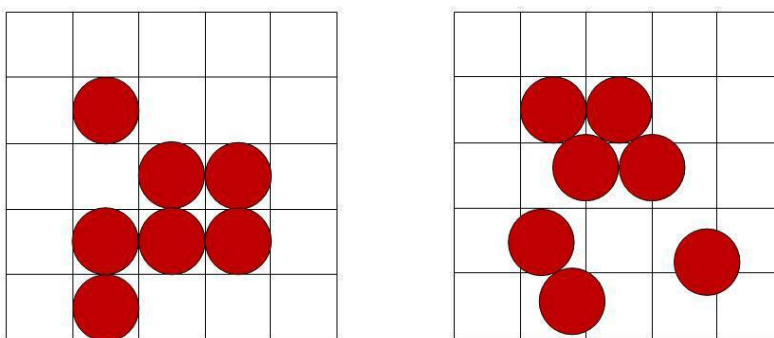


Fig. 4.2: On-lattice aggregation (left) and off-lattice aggregation (right).

Simulation lattice is the network (grid) of usually equally spaced horizontal and vertical lines that cover the simulated space. Simulation may be on-lattice, when

entities may take only specific positions in the simulated space (Fig. 4.2, left) or off-lattice, when entities may take every position, as seen in Fig. 4.2 (right).

Tuning parameters that can have a governing influence on the aggregation algorithm are sticking probability and fractal properties. Sticking probability is the probability of entities to stick to the main cluster to form an aggregate (Turkevich & Scher, 1986). If an entity sticks to the main cluster after every single collision, then the sticking probability is one (Meakin, 1999). The formed aggregates are tenuous and fractal in structure. The fractal dimension is close to 2.2 and the porosity is high, leading to the DLA model (Meakin, 1999). Sticking probability decreases with increasing number of collisions needed for successful aggregation between the entities and the main cluster. The value of sticking probability can become as low as almost zero. The formed aggregates are then closely packed like a sphere with a fractal dimension close to three. The process of formation is termed as reaction-limited aggregation (RLA) model and is described in detail in (Wang et al., 1995). Figure 4.3 illustrates exemplarily on-lattice PC aggregates generated using DLA and RLA models.

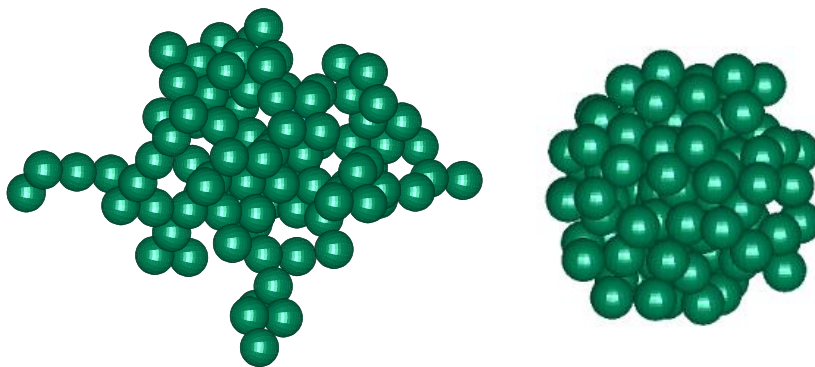


Fig. 4.3: Particle-cluster (PC) aggregates of 100 primary particles generated on-lattice using DLA (left) and RLA at sticking probability 0.0001 (right) models.

Fractal properties of any aggregate are defined by its fractal dimension (D_f) and prefactor (k). Provided a sufficiently large set of agglomerates of different sizes, the power-law relationship (which correlates the number of primary particles of the

agglomerates, N_p , with their radii of gyration, R_g in Eq. (3.7)), is supposed to be fulfilled. Assuming validity of the scaling law according to Eq. (3.7), addition of primary particles to a cluster can be performed with the goal of establishing specific fractal properties. This method of aggregation is termed as a tunable aggregation model and is described in detail in Section 4.7.

4.3 Diffusion limited aggregation model

Diffusion-limited aggregation (DLA) is the non-equilibrium growth model introduced by (Witten & Sander, 1981). The rules of the DLA model are based on an iterative stochastic process in which the particles successively follow Brownian trajectories until they touch and join together to form an aggregate. According to (Witten & Sander, 1981) a cluster is represented by the filled locations in a regular 2D grid, and each particle follows a random path consisting of jumps between neighboring positions until it reaches an unoccupied location at the periphery of the cluster. Meakin (Meakin, 1983) proposed the same model with a computationally more efficient method, where the new particles are launched from a circle with a radius slightly larger than the distance of the farthest particle of the cluster from the origin as seen in Fig. 4.4.

First, a seed particle of unitary diameter is placed at the center. Particles of unitary diameter are released individually from a launching radius R_l , which is larger than the cluster radius R_a . Particles on random walks of unitary steps either touch the aggregate or cross a killing radius R_k as illustrated in Fig. 4.4 (right). When a particle exceeds the killing radius, it is removed and a new particle is freshly launched from the launching radius. When a particle reaches the cluster, it sticks and forms an aggregate as shown in the flowchart (Fig. 4.4 (left)). This procedure is repeated until a given number of primary particles in the aggregate has been achieved.

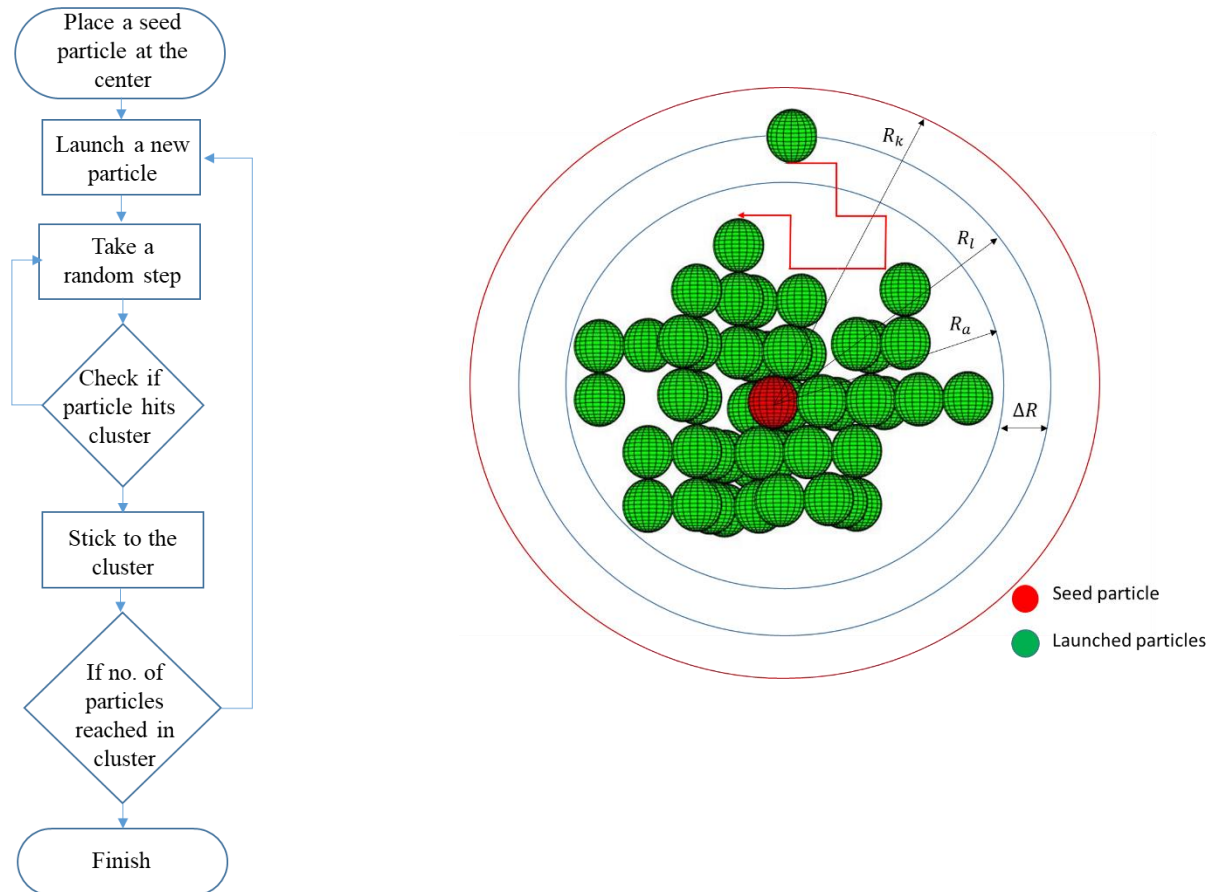


Fig. 4.4: Flowchart and pictorial representation of diffusion-limited aggregation model.

Figure 4.5 shows the morphological descriptors generated by the above algorithm through plots of porosity and fractal dimension. D_f and k of the series of agglomerates (10:10:250) generated by means of the DLA model are calculated using the power-law relationship (which correlates the number of primary particles of the agglomerates, N_p , with their radii of gyration, R_g in Eq. (3.7)) on a double logarithmic scale for the entire sample, similar to the evaluation method in (Dadkhah et al., 2012). Applying linear regression to the logarithms of N_p and R_g/R_p the calculated fractal dimension is $D_f = 2.20$ and prefactor is $k = 0.98$.

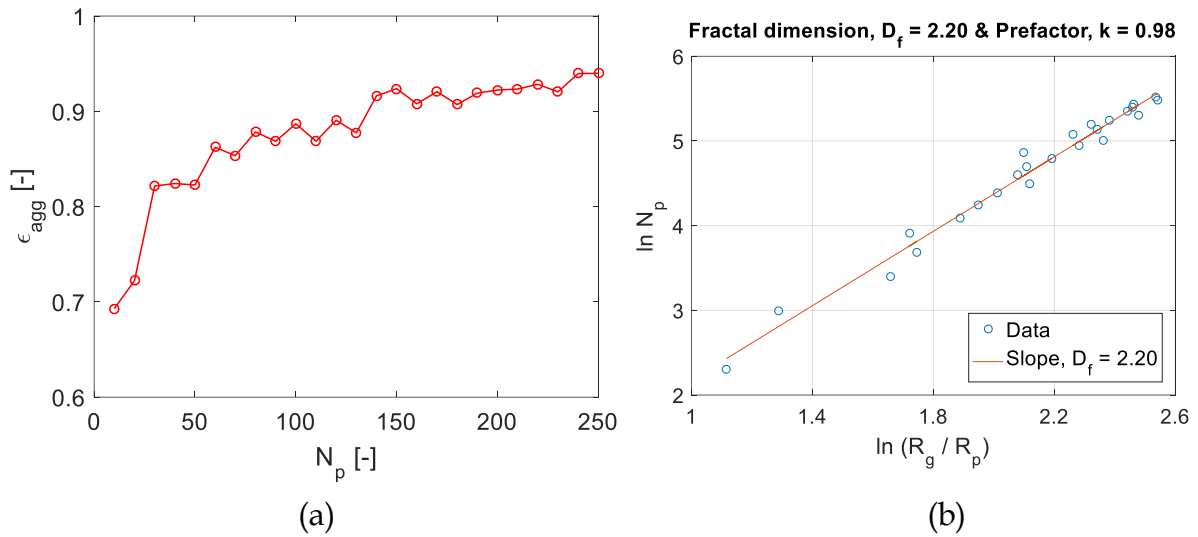


Fig. 4.5: Porosity (a) and fractal properties (b) of agglomerates generated using the DLA model.

4.4 Ballistic aggregation model

The ballistic aggregation (BA) model proposed by (Vold, 1963) is an aggregation model in which the random walks of the DLA model are replaced by ballistic trajectories at random directions. Sutherland (Sutherland, 1966) found later out that the model proposed by (Vold, 1963) had biased distribution of trajectories and improved the model for unbiased trajectories. Unlike DLA, the BA model produces asymptotically non-fractal clusters (fractal dimension equal to the space dimension). The agglomerates at the asymptotic regime are characterized by the power-law relationship (Alves et al., 2008; Bensimon et al., 1984).

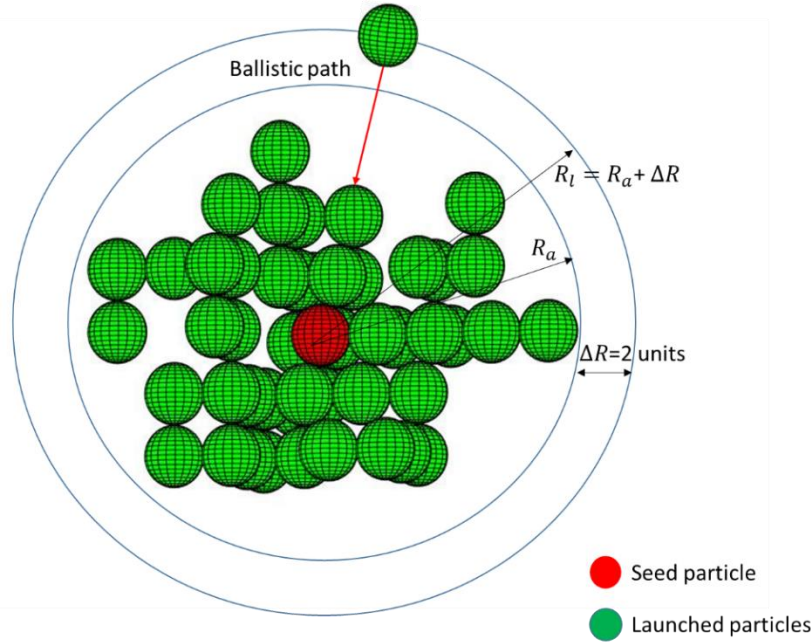


Fig. 4.6: Illustrative representation of ballistic aggregation.

Figure 4.6 shows an illustrative representation of the ballistic aggregation model. The process begins by placing a sphere (seed, marked as red in Fig. 4.6) of unit diameter at the origin and setting $R_a = 0$, where R_a is the maximum distance from the origin of any particle in the aggregate. Subsequent addition of new particles (spheres, marked as green in Fig. 4.6) is made according to the following procedure:

1. The coordinate axes (x, y, z) of the sphere are rotated by a positive angle α_1 around the x -axis to (x', y', z') , where α_1 is uniformly distributed over the range 0 to 2π and then by a positive angle α_2 around the y -axis to $(x_{new}, y_{new}, z_{new})$, where $\sin\alpha_2$ is uniformly distributed between -1 and $+1$. The transformation equations for the coordinates of the center of the sphere are:

$$x_{new} = x \cos\alpha_2 + y \sin\alpha_1 \sin\alpha_2 - z \cos\alpha_1 \sin\alpha_2, \quad (4.1)$$

$$y_{new} = y \cos\alpha_1 + z \sin\alpha_1, \quad (4.2)$$

$$z_{new} = x \sin\alpha_2 - y \sin\alpha_1 \cos\alpha_2 + z \cos\alpha_1 \cos\alpha_2. \quad (4.3)$$

2. The location of the line of approach (parallel to the z -axis) is selected randomly from the surface of the enclosing sphere (of radius $R_a + 2$ units) centered at the origin,

$$x_{app} = (R_a + 2) + rand_1(2R_a + 4), \quad (4.4)$$

$$y_{app} = -(R_a + 2) + rand_2(2R_a + 4), \quad (4.5)$$

where $rand_1$ and $rand_2$ are uniformly distributed on the range 0 to 1 and

$$x_{app}^2 + y_{app}^2 \leq (R_a + 2)^2. \quad (4.6)$$

3. The collision of the particle with the main cluster is checked. If no collision has been achieved, the axes are turned again and the entire process is repeated. If a collision has occurred, the new particle is added to the aggregate at the point of first contact.

Ballistic PC aggregation model generates aggregates with high fractal dimension (close to 3) and high porosity. However, the porosity of aggregates can be reduced by reconstruction or/and compaction (Baric et al., 2019).

4.5 Reaction limited aggregation model

Finally, a third standard aggregation process was proposed by (Eden, 1961) as an on-lattice model for biological pattern formation as, for instance, tumor growth and bacterial colonies. In this model, new particles are sequentially added to the empty neighborhood of the cluster without overlap with previously aggregated particles. Aggregates generated using this model are compact with self-affine fractal surface (Meakin, 1983). Later, (Wang et al., 1995) proposed an off-lattice Eden-model and concluded that the aggregates are porous and uniform.

Meakin (Meakin, 1999) gave an overview of six commonly used combinations of the discussed parameters (aggregate formation, particle trajectories, simulation lattice and sticking probability). The fractal dimensions of clusters generated by simple particle-cluster and cluster-cluster aggregation models are given in Table 4.1.

Table 4.1. Fractal dimension of aggregates generated by different models according to Meakin (Meakin, 1999).

Model	Particle-cluster (PC)	Cluster-cluster (CC)
Diffusion-limited (off-lattice)	2.50	1.80
Ballistic (off-lattice)	3.00	1.95
Reaction-limited (on-lattice)	3.00	2.09

From Table 4.1 it is evident that the fractal dimension of cluster-cluster (CC) aggregation models is lower than that of particle-cluster (PC) aggregation models. Consequently, the porosity of CC aggregates is always higher than the porosity of PC aggregates. According to the existing experimental findings, the fractal dimension of spray fluidized bed agglomerates is between 2 and 3, whereas porosity ranges (depending on agglomerate size) from 0.4 to 0.75 (Dadkhah, 2014; Dadkhah & Tsotsas, 2014). Hence, CC algorithms can be excluded due to too low D_f (Table 4.1). Ballistic PC aggregation has been reported to asymptotically (for large particles) result in a constant porosity of about 0.83 by Sutherland (Sutherland, 1967). This means that the aggregates formed using the ballistic model are too porous in comparison to real SFB agglomerates. Similar behavior has been observed in (Dernedde et al., 2012). Therefore, CC and ballistic algorithms are excluded from further consideration, which will focus on tuning by the sticking probability and on the tunable aggregation model.

4.6 Sticking probability model

The sticking probability aggregation model of this work is an on-lattice PC aggregation model where the primary particles take a random walk like in DLA (Witten & Sander, 1981) to stick to the main cluster. The input parameters are the number of identical spherical primary particles (N_p) and the sticking probability (P_s). The algorithm of this model (given in Fig. 4.7) is as following:

1. A seed particle (the first one from the cluster) is placed at the center of a 3D lattice.
2. The next primary particle of unitary diameter is released from a launching radius centered at the seed, R_l , larger than the cluster radius R_a . ($R_l = R_a + \Delta R$, where R_a is the distance from the center of mass of the cluster at the origin to the farthest particle of the growing cluster and ΔR is a small distance).
3. The released particle performs a random walk on the 3D lattice until it reaches the seed/cluster.
4. If a random number drawn between 0 and 1 (rand) is lower than P_s (sticking probability), then the particle is attached to the seed/cluster. Otherwise, the random walk process continues until the seed/cluster is reached again.
5. When the current particle has been attached to the cluster, the next primary particle is generated and released.
6. If the particle reaches a position that is further away from the center of mass than R_k (killing radius), then it is eliminated and launched again.
7. Steps 2-6 are repeated until the desired number of primary particles in the aggregate is achieved.

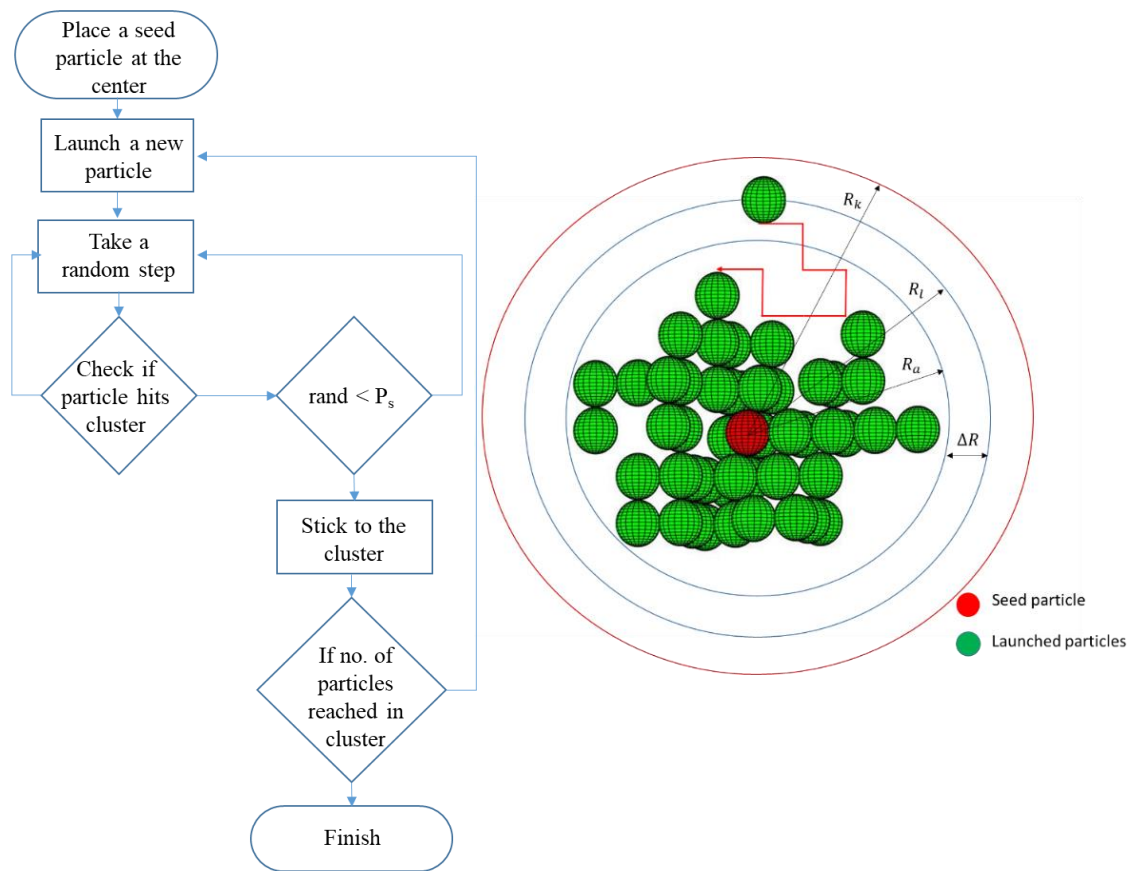


Fig. 4.7: Flowchart and pictorial representation of the sticking probability model.

Several series of agglomerates made of monodisperse spherical primary particles ranging in number from 5 to 100 have been generated at an increment of 5 using this model at various values of the sticking probability, and the fractal dimension of each series has been evaluated. Then, 10 realizations of this procedure have been conducted for each sticking probability and the results are plotted in Fig. 4.8. Each box, in Fig. 4.8, represents the respective interquartile range (difference between the 75th and 25th percentile). The horizontal bar (marked as red) inside the box is the median. Regarding the horizontal bars (marked as black), the one on the top of the box is the largest data point, while the other at the bottom is the lowest data point excluding the outliers (denoted by red plus sign). It can be seen that the fractal dimension increases with a decrease in sticking probability.

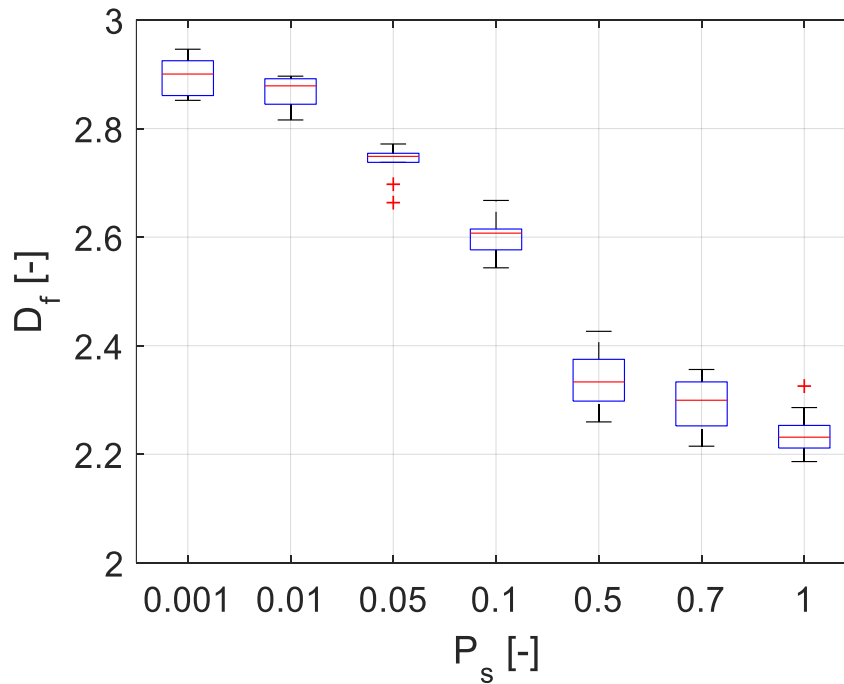
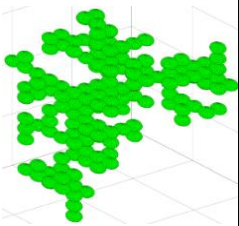
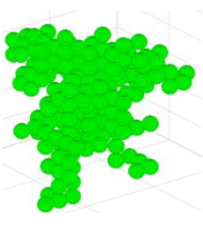
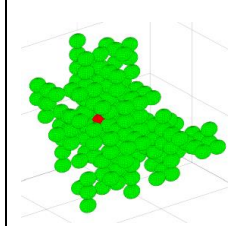
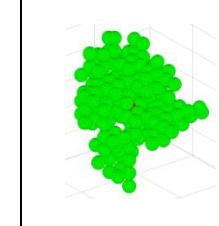


Fig. 4.8: The fractal dimension of agglomerates obtained at different sticking probabilities (P_s) using the sticking probability model.

Morphology of the biggest agglomerates (with 100 primary particles) generated synthetically at different sticking probabilities and computation time on the mentioned personal computer (described in Section 3.10) required for one realization in each case are noted in Table 4.2. The porosity of the agglomerates in Table 4.2 has been measured using the radius of gyration method.

As the sticking probability decreases, porosity decreases and reaches an asymptotic value. The lowest porosity achieved using this model for $N_p = 100$ is comparable to the highest porosities measured for the largest agglomerates in (Dadkhah & Tsotsas, 2014), but still higher than the average porosity of SFB agglomerates of around 0.6. At lower sticking probability, the computation time increases for only marginal change in the structure of an agglomerate, as can be expected.

Table 4.2. Agglomerates ($N_p = 100$) generated using the sticking probability model at different sticking probabilities.

Sticking probability (P_s)	1	0.1	0.01	0.001
				
Porosity (ϵ_{agg})	0.922	0.813	0.765	0.745
Computation time (s)	6	14	60	523

The agglomerate generation here is more efficient as the agglomerates are generated by an on-lattice model. However, the agglomerates would be more realistic (on short scale) if they were generated by an off-lattice model (Meakin, 1983).

4.7 Tunable aggregation model

The trend of the sticking probability model to produce too high agglomerate porosities motivated the use of a model that can better tune morphological and fractal properties. A review of the developments in the tunable aggregation model over the years is presented in Table 4.3. The first tunable CC aggregation algorithm was introduced by (Thouy & Jullien, 1994). Subsequently, several other studies have been conducted to propose different tunable algorithms, however, in most of these studies only the fractal dimension was retained. A notable exception is the algorithm proposed by

(Filippov et al., 2000), which was capable of preserving both the fractal dimension and the prefactor.

Table 4.3. Tunable methods used by different researchers in the past for monodispersed primary particles.

Year	Researcher	Method	Comments
1994	Thouy & Jullien, 1994	CC tuned with D_f	$D_f > 2.5$ not possible No comment on k
1995	Mackowski, 1995	Tuned with the power law and R_g	First to use R_g as a tuning factor
2000	Filippov et al., 2000	Tuned with the power law and R_g ; made new correlation for particle position (sequential algorithm)	$k > 1.66$ not possible for PC; using CC, $D_f >$ 2.3 not possible
2009	Chakrabarty et al., 2009	FracMAP: PC tuned with the power law	$D_f > 2$ not possible $k < 1$ not possible
2014	Skorupski et al., 2014	FLAGE: Using Filippov model	$k > 1.66$ not possible for PC; using CC, $D_f >$ 2.3 not possible

In the present work, the sequential algorithm (SA) proposed by Filippov (Filippov et al., 2000) for the PC aggregation model is used. This model is off-lattice and the input parameters are the number and radius of primary particles (N_p and R_p) and the fractal properties (D_f and k) of the agglomerates. In this algorithm monodisperse spherical primary particles are added one by one using the following steps:

1. Insert a particle (seed) at the center of a 3D simulation lattice.
2. Place the second particle close to it, by selecting a contact point on the spherical surface of the seed.
3. For the third and next particles, the correlation of (Filippov et al., 2000) is used. The center of the next particle is on the sphere of radius R ,

$$R^2 = \frac{N^2 R_p^2}{N-1} \left(\frac{N}{k}\right)^{\frac{2}{D_f}} - \frac{N R_p^2}{N-1} - N R_p^2 \left(\frac{N-1}{k}\right)^{\frac{2}{D_f}}, \quad (4.7)$$

such that there is no overlapping, as shown in Fig. 4.9. Here, N is from 3 to N_p .

4. Randomly a point is selected on the sphere (of radius R) and contact and overlapping conditions are checked.
5. If there is a contact without overlapping then the new particle is attached to the growing cluster (initially a dimer).
6. Steps 3-5 are repeated until the targeted number of primary particles is achieved.

Seed particle (step 1) Binary addition (step 2) Aggregation (steps 3-6)

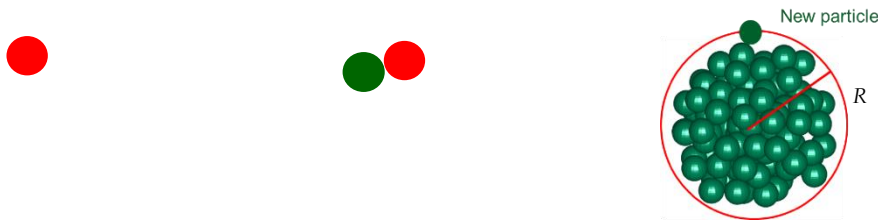
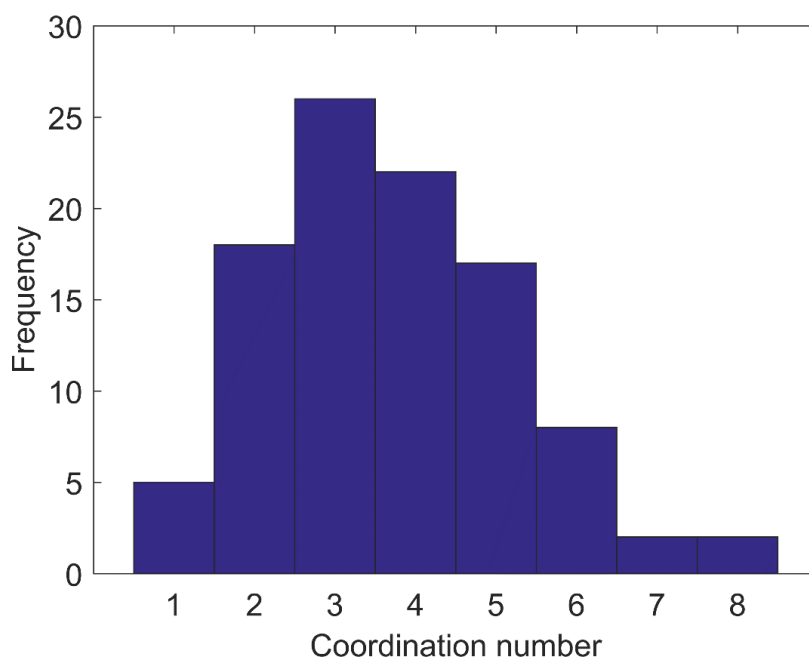
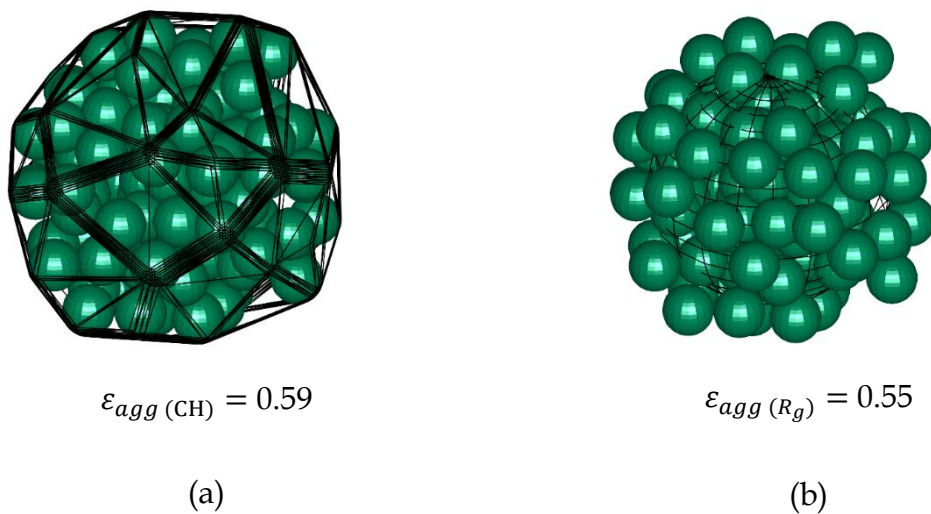


Fig. 4.9: A representation of aggregation of monodisperse primary particles using the sequential algorithm.

The morphology of an agglomerate ($N_p = 100$) formed using SA with $D_f = 3$ and $k = 0.9$ is shown in Fig. 4.10. Using this model, the limitation of the sticking probability model is overcome and agglomerates with porosity less than 0.7 can easily be created.



(c)

Fig. 4.10: Porosity using the convex hull (CH) method (a) and the radius of gyration method (b) and coordination number distribution (c) of an agglomerate ($N_p = 100$) generated using SA at $D_f = 3$ and $k = 0.9$.

The range of morphological descriptors reported by Dadkhah and Tsotsas in their experiments (Dadkhah & Tsotsas, 2014) (Table B.2) is achieved using this model. However, the limitation in the prefactor (greater than 1.66 not possible) still remains, whereas prefactors greater than 1.66 are common in practice (Dadkhah & Tsotsas, 2014; Lapuerta et al., 2006; Pashminehazar et al., 2019; Sorensen, 2011) and it would be desirable to use the model without restriction.

4.8 Tunable sequential aggregation model and its limitation

As stated in Table 4.3, the only limitation of SA is that prefactor values of $k > 1.66$ are not possible. This limitation can be overcome by tuning D_f with respect to the porosity correlation of Eq. (3.13) (Singh & Tsotsas, 2019),

$$\varepsilon_{agg} = 1 - 0.465N_p \left(\frac{k}{N_p} \right)^{\frac{3}{D_f}}. \quad (4.8)$$

Keeping the porosity (ε_{agg}) and the number of primary particles (N_p) same, the fractal dimension is changed by setting the prefactor to $k = 1$:

$$\varepsilon_{agg} = 1 - 0.465N_p \left(\frac{1}{N_p} \right)^{\frac{3}{D_{f,tuned}}}. \quad (4.9)$$

Equating Eqs. (4.8) and (4.9), the correlation for tuned fractal dimension at specific prefactor ($k = 1$) is obtained

$$D_{f,tuned} = D_f \left(\frac{\ln \frac{N_p}{1}}{\ln \frac{1}{N_p}} \right). \quad (4.10)$$

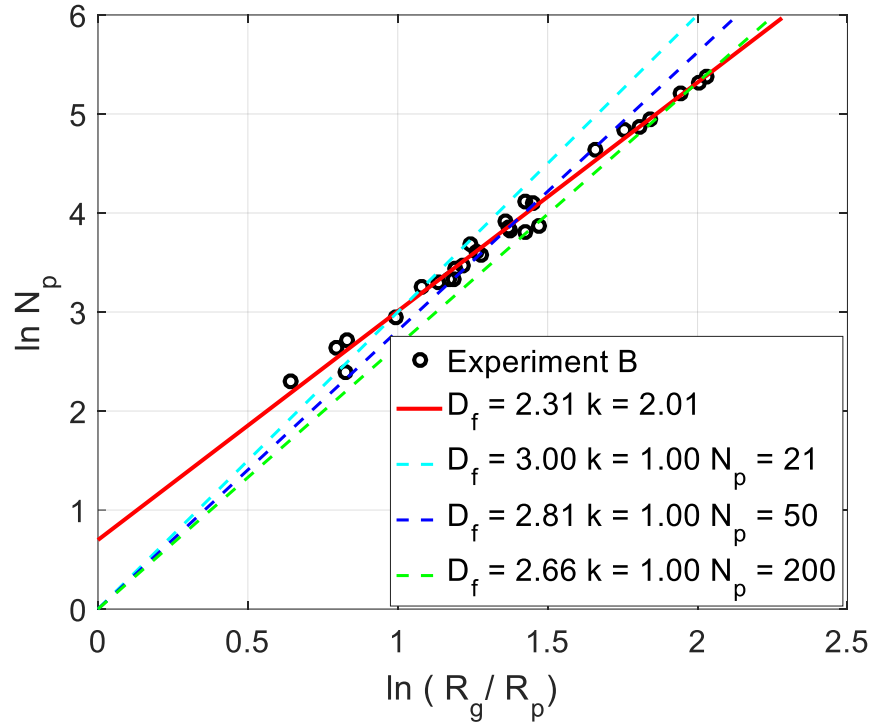


Fig. 4.11: Logarithmic plots of power law from the origin (dashed lines) with same prefactor ($k = 1$) and different slopes ($D_f = 3.00, 2.81, 2.66$) corresponding to the desired plot (solid line) with prefactor ($k = 2.01$) and fractal dimension ($D_f = 2.31$) for certain numbers of primary particles.

Using the power-law relationship (Eq. (3.7)) to compute the change in the fractal properties with the same radius of gyration, the same relationship as in Eq. (4.10) is obtained. The logarithmic version of the power law,

$$\ln N_p = D_f \ln \left(\frac{R_g}{R_p} \right) + \ln k, \quad (4.11)$$

is illustrated in Fig. 4.11 with straight lines that represent original and tuned combinations of D_f and k . Tuned combinations fulfill Eq. (4.10) (preservation of

agglomerate porosity) only for a specific number of primary particles, which is also given in the insert of Fig. 4.11.

Table 4.4 shows the comparison in terms of porosity and mean coordination number of an agglomerate ($N_p = 50$) from Exp. B of Dadkhah (Dadkhah, 2014) and agglomerates with the same number of primary particles synthesized using the SA model. The latter have been obtained with the genuine fractal properties, as well as with modified k (both at $k = 1$ and on some neighbor values, for comparison) and tuned D_f .

Table 4.4. Agglomerates ($N_p = 50$) generated using SA with tuned D_f model and compared with an agglomerate ($N_p = 50$) from Exp. B (Dadkhah, 2014).

	D_f	k	ϵ_{agg} (Eq. (4.8))	ϵ_{agg} (R_g)	ϵ_{agg} (CH)	MCN
Experiment B	2.31	2.01	0.64	0.66	0.64	3.06
	2.68	1.2	0.64	0.61	0.63	3.10
SA	2.81	1.0	0.64	0.61	0.62	3.08
	2.97	0.8	0.64	0.61	0.63	3.02

Experiment B has been chosen for comparison because the size of the primary particles measured by Dadkhah for Exp. B is close to monodisperse. Consequently, this experiment replicates in the best way the assumptions behind the monodisperse tunable aggregation model used in this chapter and can act as a reference to validate the tunable D_f model, as seen in Fig. 4.12.

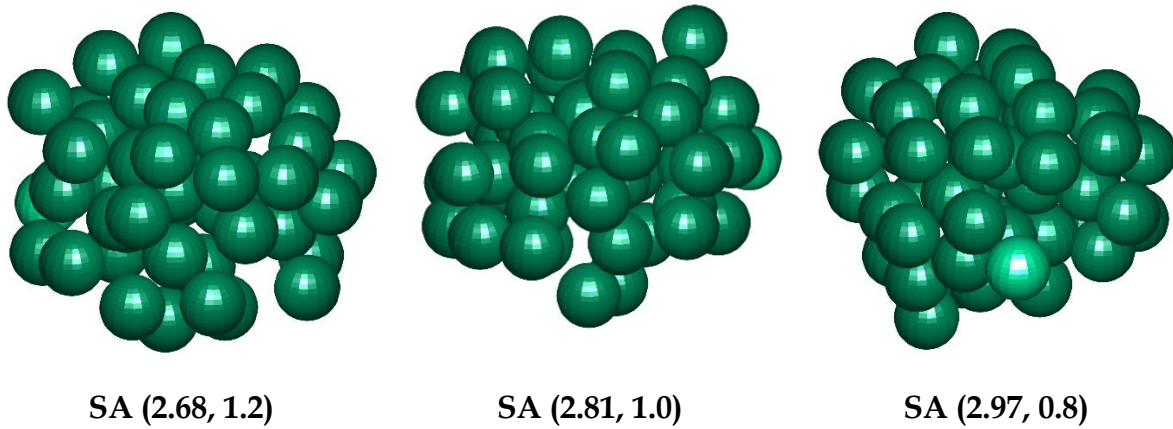


Fig. 4.12: Agglomerates ($N_p = 50$) generated using SA with tuned D_f and k according to Table 4.4.

By tuning the fractal dimension with different prefactors in a way that keeps the porosity that can be obtained from Eq. (4.8) constant, the formed agglomerates are almost the same. This can be visually observed in Fig. 4.12, but it can also be seen in nearly constant porosities obtained by the gyration and convex hull methods as well as nearly constant average coordination number (Table 4.4). Therefore, the limitation of SA regarding the value of k is overcome and all the agglomerates can be constructed with this model.

However, there is another limitation depicted in Fig. 4.11. As the slope increases the fractal dimension also increases, but $D_f > 3$ is physically not feasible, which means that slopes of the dashed lines can only be increased until 71.5° . This limits the formation of aggregates with primary particles less than

$$N_{p,lim} = k \left(\frac{3}{3-D_f} \right). \quad (4.12)$$

This restriction is overcome by constructing the aggregates until $N_{p,lim}$ (for Exp. B until the value of $N_{p,lim} = 21$) at $D_f = 3$ and $k = 1$. The reason for using these particular values of D_f and k is the compactness of small SFB agglomerates.

Combining the SA with this novel approach of tuned fractal dimension enables to construct any SFB agglomerate. The algorithm, referred to in the following as tunable sequential aggregation (TSA) model, is computationally fast. It takes less than 2 seconds to generate an agglomerate with 100 monodisperse spherical primary particles on the mentioned personal computer (described in Section 3.10).

4.9 Validation of the TSA model

Agglomerates with the same number of primary particles as examined by Dadkhah (Dadkhah, 2014) are generated using the TSA model. For each trial, the TSA model takes the values of D_f and k from the empirical correlations obtained by Singh and Tsotsas (Singh & Tsotsas, 2019), i.e. from Eqs. (3.18) and (3.17). These values of D_f and k are used as the input parameters for the TSA model to generate the agglomerates at tuned D_f (calculated using Eq. (4.10)) and $k = 1$. Monodisperse primary particles with diameter of 520 μm are combined with each other in the TSA model.

The morphological descriptors of the generated agglomerates from the TSA model are obtained and averaged over five realizations. In each realization a series of agglomerates are produced with exactly the same number of primary particles as in the experimental morphological evaluation. D_f and k of the agglomerates generated by means of the TSA model (Table 4.5) are calculated using the power-law relationship on a log scale (Eq. (3.7)) for the entire sample, similar to Dadkhah's evaluation method (Dadkhah et al., 2012). Values of ε_{agg} by the radius of gyration method and of MCN are computed for each agglomerate of a series, then averaged arithmetically for the series, then averaged among five realization and, finally, given in Table 4.5. This is also reproducing the procedure that Dadkhah has used in her evaluation of tomography data.

Morphological descriptors obtained from the TSA model agree very well with the experimental values (Dadkhah & Tsotsas, 2014). A slight deviation in the results of the TSA model is due to the size dispersity of primary particles used in the experiments, while in simulations the primary particles are fully monodisperse with diameter of 520 μm . However, all trends of changes in morphology by changing operating conditions are similar between reconstructed and real agglomerates from (Dadkhah & Tsotsas, 2014).

Table 4.5. Experimental and simulation results for each trial.

Experiment set	A	B	C	D	E
Temperature [$^{\circ}\text{C}$]	60	30	90	60	60
Binder [wt. %]	2	2	2	6	10
Experimental results for each trial (Dadkhah & Tsotsas, 2014)					
D_f [-]	2.45	2.31	2.94	2.24	2.09
k [-]	1.76	2.01	0.98	1.96	2.24
Average ε_{agg} [-]	0.57	0.62	0.53	0.58	0.63
Average MCN [-]	3.32	3.10	4.02	2.92	2.87
TSA model results for each trial (averaged over 5 realizations)					
D_f [-]	2.37	2.24	2.72	2.17	2.05
k [-]	2.12	2.37	1.48	2.32	2.53
Average ε_{agg} [-]	0.54	0.59	0.53	0.55	0.64
Average MCN[-]	3.61	3.52	3.90	3.31	3.09

Furthermore, the porosity obtained by the gyration method using the TSA model is compared with Exp. B (in which the primary particles have been close to monodisperse) for specific agglomerates as well as theoretically, by the porosity correlation (Eq. (4.8)) with fractal properties (D_f , k) obtained from experiment and simulation (Table 4.5) in Fig. 4.13. Agglomerates simulated using the TSA model are lying close to the curve of Eq. (4.8) with fractal properties (D_f , k) obtained from

simulation (Table 4.5). There is a difference to the curve with fractal properties (D_f, k) obtained from Exp. B (Table 4.5), but this difference is small.

Figure 4.13 validates the porosity correlation (Eq. (4.8)) for the simulated agglomerates in similar way as it was validated previously in Section 3.8.1 (Singh & Tsotsas, 2019) for real agglomerates obtained from experiments (Dadkhah, 2014). One important aspect of Fig. 4.13 is that the agglomerates formed using the TSA model, regardless of tuned fractal properties (D_f, k) at different N_p , are in close affinity to the agglomerates examined by Dadkhah in her experiments (Dadkhah, 2014).

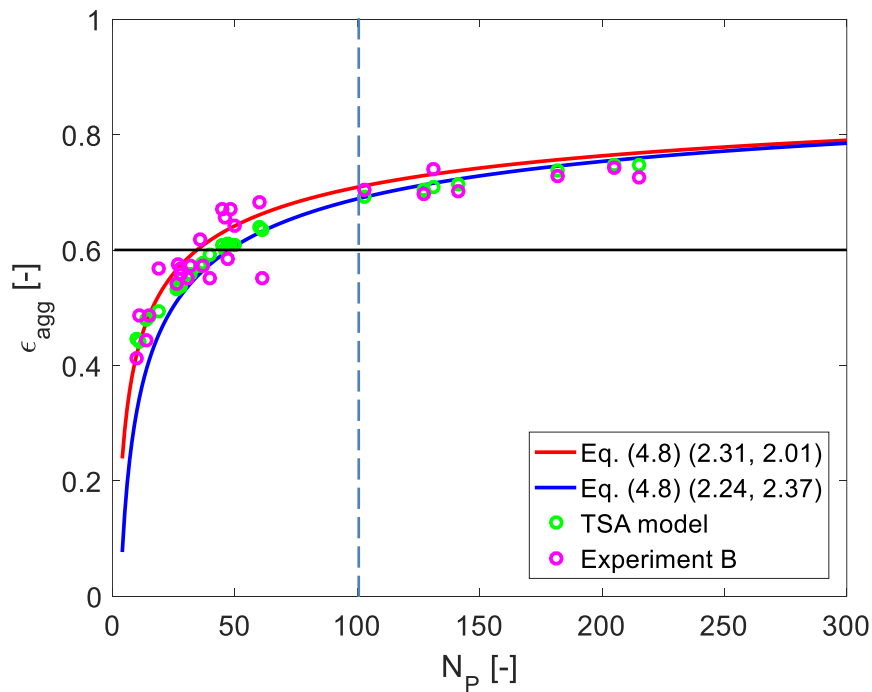


Fig. 4.13: Comparison of porosity obtained from Eq. (4.8) with D_f, k from Table 4.5 (from experiments or simulations) with the porosity of real agglomerates from (Dadkhah, 2014) and agglomerates reconstructed by the means of the TSA model (both evaluated using the gyration method).

The mean coordination numbers for all the agglomerates simulated using the TSA model are compared to the experimental values in Fig. 4.14. MCN using the TSA model for the small agglomerates ($N_p < N_{p,lim}$) are nearly similar for all the

experiments. The reason behind this is the limitation of the TSA model that the small agglomerates are reconstructed at $D_f = 3$.

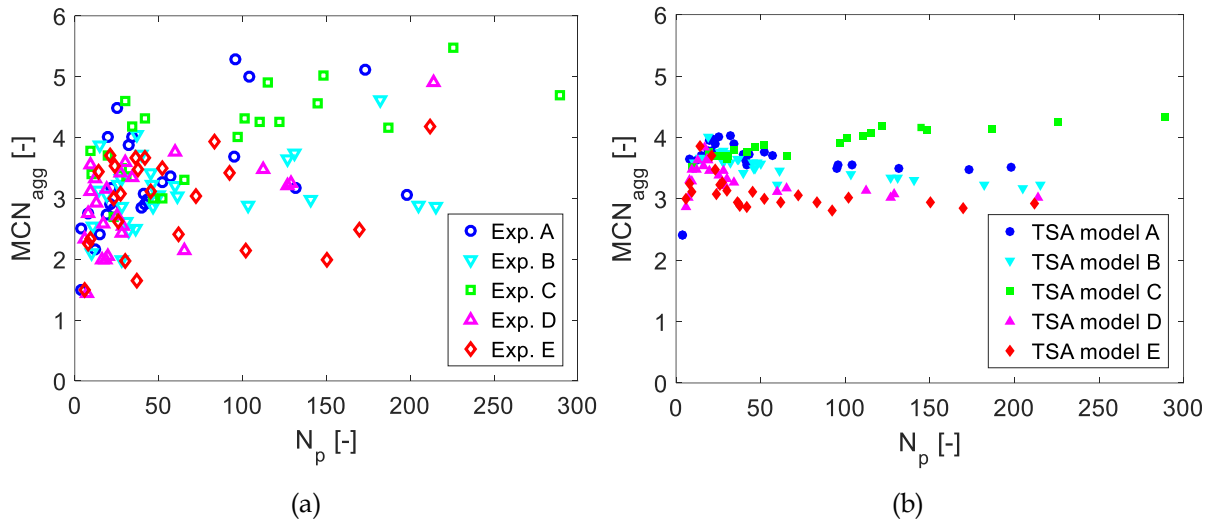


Fig. 4.14: Mean coordination number (MCN) of agglomerates for a set of experiments (Dadkhah & Tsotsas, 2014) (a) compared with synthetic agglomerates using the TSA model (b).

The spread of the experimental data (Fig. 4.14a) is higher because of at least moderately polydisperse primary particles having been used in the experiments (Dadkhah & Tsotsas, 2014). The trends of the results from the TSA model are similar to the experiments (Dadkhah & Tsotsas, 2014). With a high fractal dimension, the porosity is low and MCN is high, leading to a compact structure. On contrary at low fractal dimension, the porosity is high and MCN is low, leading to tenuous structure. The coordination number of compact agglomerates (Exp. C) is the highest and that of the tenuous agglomerates (Exp. E) is the lowest.

Consequently, the strength of agglomerates (reconstructed using the TSA model) is calculated using the Rumpf model (Rumpf, 1958) to

$$\sigma_T = \frac{\text{MCN}(1-\varepsilon_{agg})F_c}{\pi D_p^2}, \quad (4.13)$$

for the five experiments and compared in Fig. 4.15. Here, MCN and ε_{agg} are mean coordination number and porosity of an agglomerate, F_c is the mean cohesive force between the primary particles of diameter D_p . On the one hand, the strength is calculated from Eq. (4.13) with MCN and ε_{agg} from the TSA model with $D_p = 520 \mu\text{m}$ and F_c assumed as 20 N. On the other hand, the strength is calculated using a simplification in determining the MCN ($= \pi/\varepsilon_{agg}$) (Peglow et al., 2014; Rumpf, 1958), ε_{agg} from the TSA model, and same D_p and F_c .

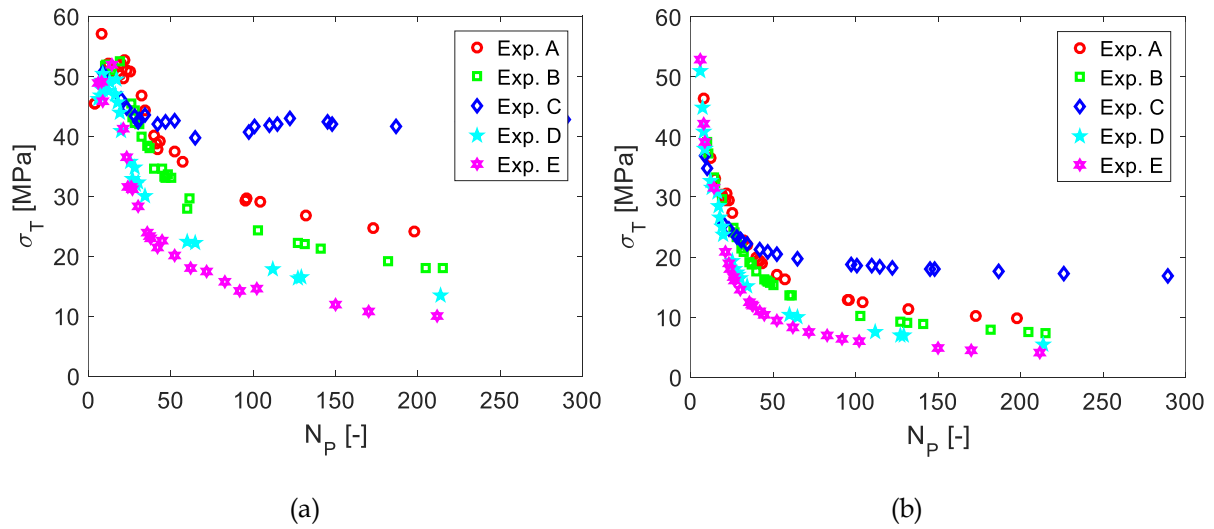


Fig. 4.15: Strength calculated using Eq. (4.13) for the agglomerates generated by means of the TSA model with MCN from TSA model (a) and with $\text{MCN} = \pi/\varepsilon_{agg}$ (b) for a set of experiments (Dadkhah & Tsotsas, 2014).

From the plots of strength calculated using different ways of obtaining MCN in Fig. 4.15 it is clear that agglomerate morphology should be considered as comprehensively as possible (i.e. with MCN and ε_{agg} considered separately) during the process of breakage. It is also evident from Fig. 4.15 that the strength of the most compact agglomerates (Exp. C) is highest, while it is lowest for the most tenuous agglomerates (Exp. E).

4.10 CVMC simulation incorporated with aggregation model (CVMC-2)

The structural change has already been implemented into the CVMC model in the way that has been described in Chapter 3 to determine the kinetics of the agglomeration process at different operating conditions. However, other morphological features like MCN of the agglomerates were not accessible by that approach, though they are very important for the characterization of the product. In this section the CVMC model that has been described in Chapter 3 is modified by introducing the TSA model. Figure 4.16 shows a schematic representation of simulating the SFB agglomeration by incorporating the aggregation model. Using the TSA model as the aggregation model, various morphological descriptors are determined.

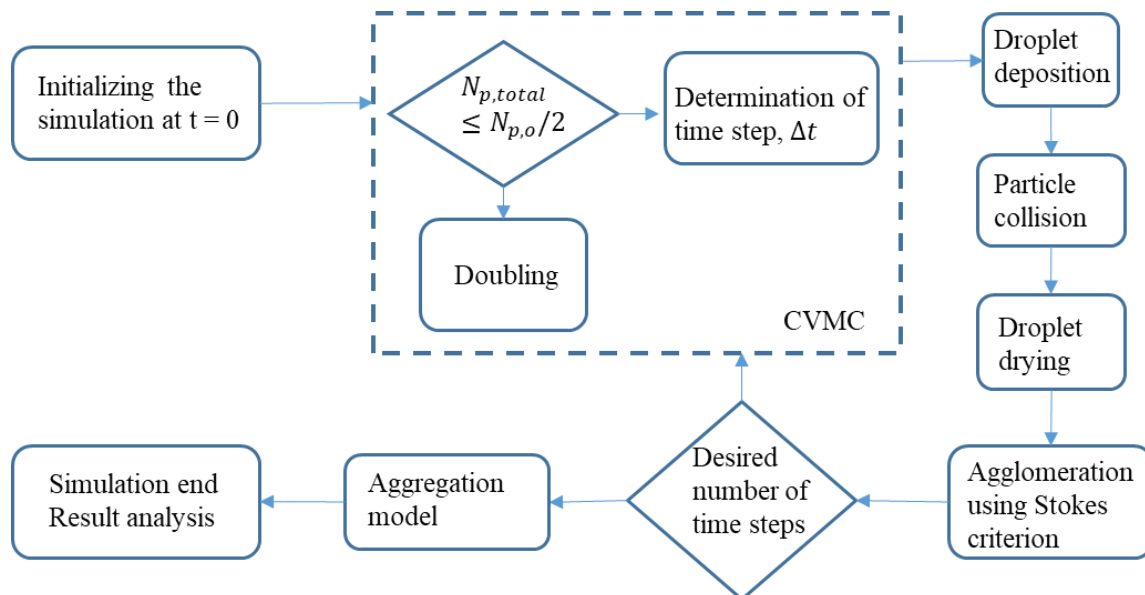


Fig. 4.16: Simplified diagram of the present CVMC (CVMC-2) algorithm.

Figure 4.17 shows two ways of implementing the TSA model into the CVMC model: postprocessing and in-situ. In **postprocessing**, the TSA model is called at the end of

the CVMC simulation. The simulation scheme is same as in Chapter 3 (Singh & Tsotsas, 2019) and after the simulation ends the formed agglomerates are reconstructed using the TSA model with input parameters (N_p, D_f, k) from the CVMC model. Whereas in the **in-situ** version the TSA model is called at every time step of the CVMC simulation. Unlike in Chapter 3 (Singh & Tsotsas, 2019), where the porosity is calculated using Eq. (4.8), here the porosity is calculated using the radius of gyration method by reconstructing the formed agglomerates with the TSA model. Then, this porosity is inserted in Eq. (3.14) to obtain agglomerate diameter, D_{agg} .

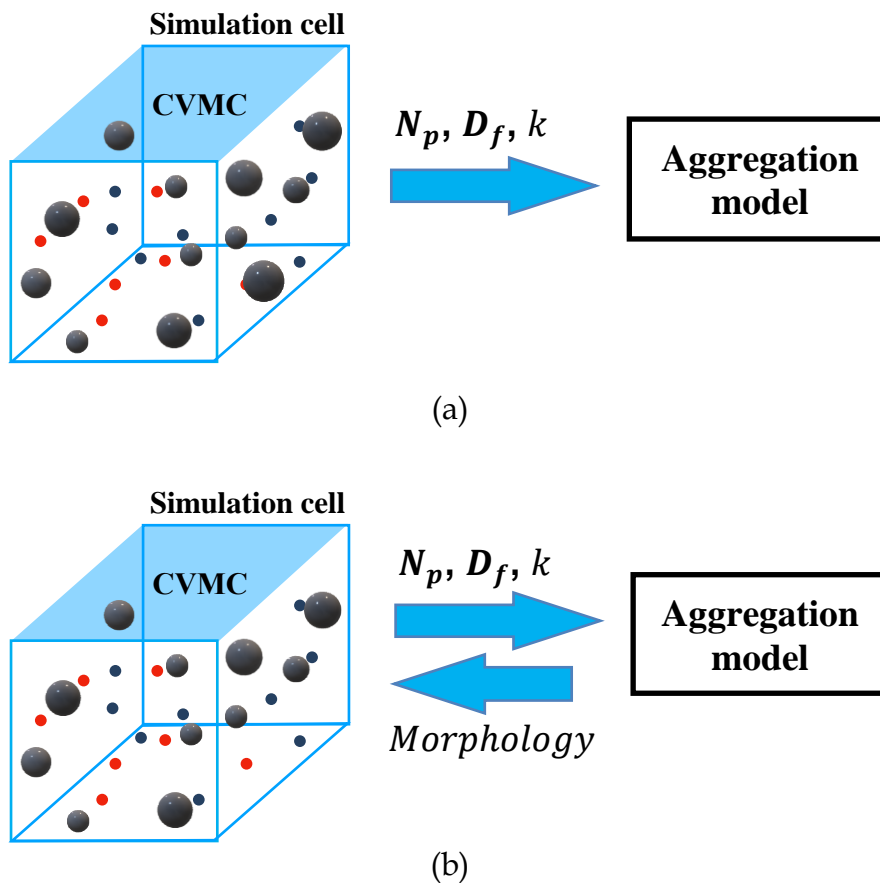


Fig. 4.17: Two ways of implementing the TSA model in the CVMC simulation: postprocessing (a) and in-situ (b).

Morphological descriptors (D_f , k , average ε_{agg} , average MCN) obtained for different experiments in (Dadkhah & Tsotsas, 2014), namely for Exp. A to Exp. E with glass beads as the primary particles, have been presented in Table 4.5. Experiments B, A and C represent the increasing of inlet fluidized gas temperature from 30°C to 60°C and 90°C. Similarly, experiments A, D, and E represent increasing binder (Hydroxypropylmethylcellulose, HPMC) mass fraction of 2 wt. %, 6 wt. % and 10 wt. %. Glass beads with a relatively narrow range of diameters between 450 μm and 631 μm with an average diameter of 520 μm were used for the experiments (Dadkhah & Tsotsas, 2014). A brief description of the experiments with morphological descriptors examined is given in Appendix B.

In postprocessing, the CVMC modeling scheme is same as the CVMC model of Chapter 3 (Singh & Tsotsas, 2019) (**CVMC-1**) with the TSA model called at the end of the CVMC simulation. SFB agglomerates with different numbers of primary particles for the different experiments, as reconstructed using the TSA model, are tabulated in Fig. 4.18. Using the in-situ way of implementing the TSA model in the CVMC model (denoted by **CVMC-2**), the formed agglomerates are reconstructed by means of the TSA model to calculate the porosity at every time step of the CVMC simulation. However, the breakage of solid agglomerates is still not considered and wetting is similar to Chapter 3 (Singh & Tsotsas, 2019; Terrazas-Velarde et al., 2009) in the CVMC-2 model. Simulations for the different experiments (Table 4.5) have been carried out for 300 s, using the same simulation parameters as in Chapter 3 (Singh & Tsotsas, 2019).

Both ways of implementation of the TSA model in the CVMC model provide the same morphological results as in Fig. 4.18. This means that for the same number of primary particles, the agglomerates formed are identical. Increasing the inlet fluidization gas temperature (Exp. B, A and C), the fractal dimension of the formed agglomerates

increases and the prefactor decreases, which in turn decreases the porosity and increases the mean coordination number. On contrary, increasing the binder concentration (Exp. A, D and E) leads to a decrease in the fractal dimension at increasing prefactor, resulting in an increase in porosity and a decrease in the mean coordination number.

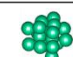

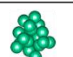
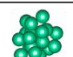
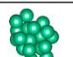
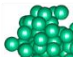
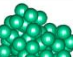

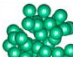
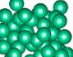
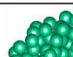
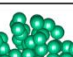
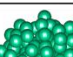
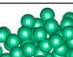
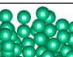
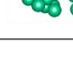
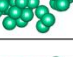


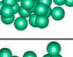
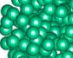



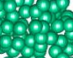
	A	B	C	D	E
$N_p = 20$					
$N_p = 50$					
$N_p = 100$					
$N_p = 200$					
$N_p = 300$					

Fig. 4.18: SFB agglomerates of different sizes reconstructed using the TSA model for different experimental trials.

In Fig. 4.19 diameters of agglomerates (using Eq. (3.14)) are calculated by taking the porosity from the TSA model and plotted against the number of primary particles to depict the morphological change for different experiments. The diameter of agglomerates with a similar number of primary particles is lowest for Exp. C and highest for Exp. E. The reason behind this is that at higher inlet gas temperature (Exp. C) the formed agglomerates are compact with high fractal dimension and coordination number and low porosity (Fig. 4.18). Contrary, for high binder content

(Exp. E) the agglomerates are tenuous with low fractal dimension and coordination number and high porosity (Fig. 4.18). Therefore, the diameter of a volume equivalent sphere is highest for Exp. E and lowest for Exp. C. Similar conclusions were made by Dadkhah for the experimentally produced agglomerates (Dadkhah & Tsotsas, 2014).

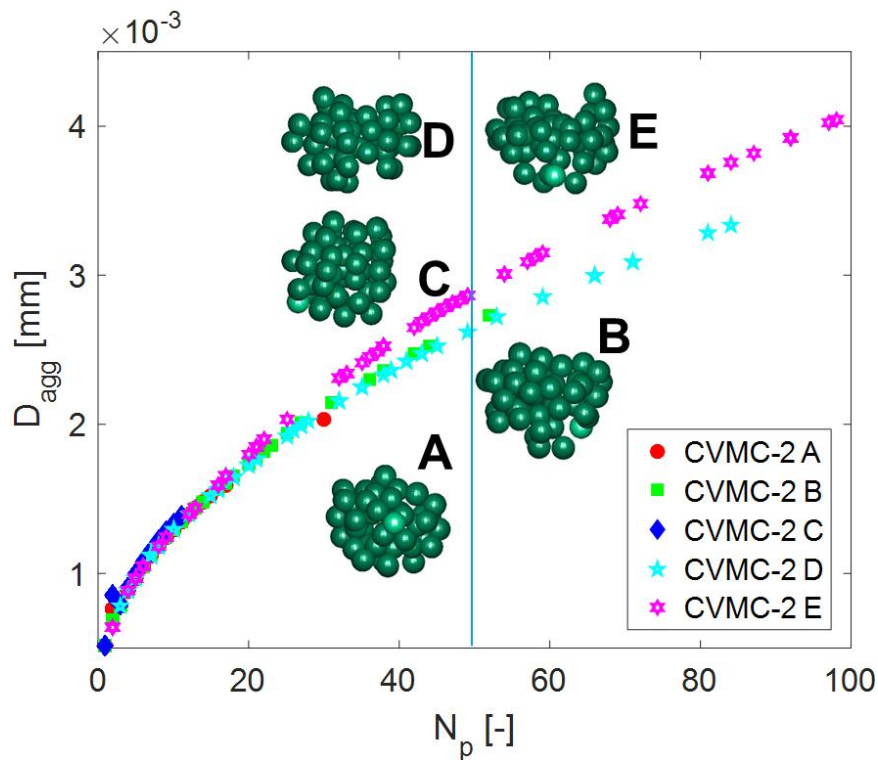


Fig. 4.19: Agglomerate diameter with respect to the number of primary particles, along with agglomerates for $N_p = 50$ for the different experiments at 300 s.

Moreover, in Fig. 4.20 the temporal change of the diameter for the different experiments is used to depict the kinetics of the process. As already mentioned, in contrast to the CVMC-1 model, the agglomerate diameter in the CVMC-2 model is calculated using Eq. (3.14) with porosity evaluated from the TSA model. This has though only little influence on the kinetics of the process (Fig. 4.20). The relative diameter of the agglomerates is the ratio of Sauter mean diameter of the population

and the initial diameter ($D_p = 520 \mu\text{m}$) at a given instant of time (Singh & Tsotsas, 2019). As the temperature of the inlet fluidization gas increases (Exp. B, A and C) the size of deposited droplets decreases and the probability of successful collision becomes smaller (Singh & Tsotsas, 2019; Terrazas-Velarde et al., 2011a). Consequently, the growth rate decreases.

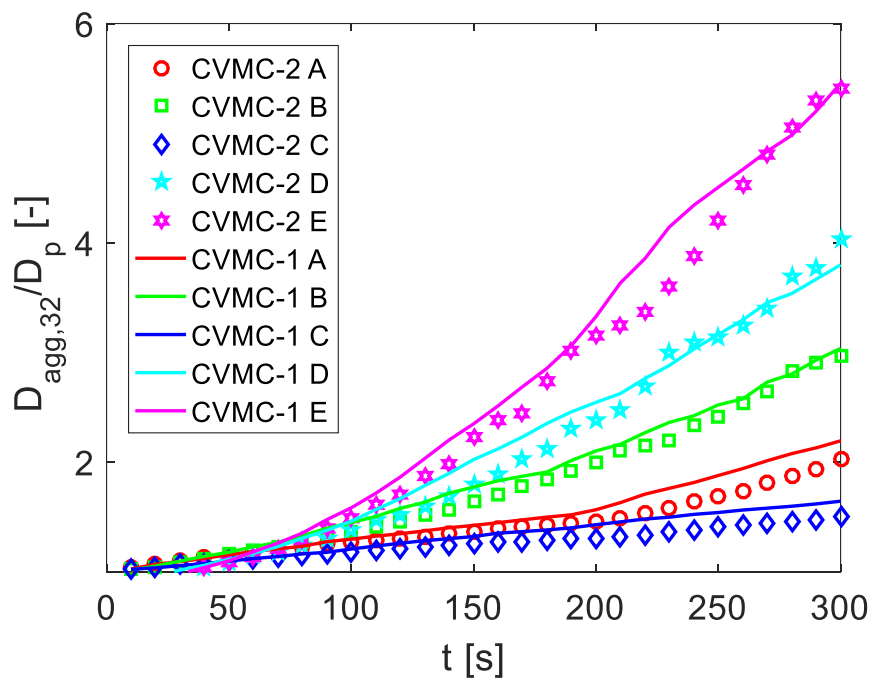


Fig. 4.20: Agglomerate relative average diameter with respect to time, using different model versions (CVMC-1 and CVMC-2) for the different experiments.

On the contrary, as the binder concentration increases (Exp. A, D, and E) the growth rate increases. Binder droplets become more viscous when the binder concentration increases and the fulfillment of the Stokes criterion (Adetayo & Ennis, 1997) upon wet collision becomes easier. A more viscous liquid can rather dissipate the kinetic energy of colliding particles, leading to a higher growth rate (Singh & Tsotsas, 2019; Terrazas-Velarde et al., 2011a). Very similar behavior was seen in (Singh & Tsotsas, 2019; Terrazas-Velarde et al., 2009). However, as can be expected, the CVMC-2 model is

computationally slower than the CVMC-1 model from Chapter 3 (Singh & Tsotsas, 2019).

Using the CVMC-2 model (in-situ) the morphology of the agglomerates formed at every time step can provide the foundation for incorporating breakage in the simulation by calculating the strength of agglomerates by means of Eq. (4.13). Both porosity and coordination number of an agglomerate, that can be predicted using the CVMC-2 model, are required to fully assess its strength. Further upon calculation of the surface area of the formed agglomerates, the description of the droplet (binder) deposition mechanism in the model could be enhanced.

4.11 Conclusion

Morphological descriptors are important in order to capture the structure of spray fluidized bed agglomerates and macroscopic properties, like strength, associated with them. From the plethora of aggregation models in literature, the PC aggregation model offers a good prognosis for SFB agglomerates. Tuning of the aggregation model by means of the sticking probability was not favorable for spray fluidized bed agglomeration. Fractal dimensions obtained in this way were in a reasonable range of 2 to 3, and porosity reached an asymptotic minimum with decreasing sticking probability, but this minimum was still too high compared to the porosity of real SFB agglomerates determined by (Dadkhah & Tsotsas, 2014). The tunable PC aggregation model developed by (Filippov et al., 2000) was therefore used for reconstructing the SFB agglomerates. The fractal dimension and porosity obtained with this model were comparable to those of real SFB agglomerates, but the algorithm was limited to prefactors less than 1.66 according to (Filippov et al., 2000).

A novel approach of tuning the fractal dimension with a given prefactor (equal to one) has been introduced to overcome the limitation of the prefactor. This approach was validated by the experimental data, as the structural features (porosity and coordination number) remained essentially the same when tuning at different prefactor. Irrespectively of the variable fractal dimension for each agglomerate in the TSA model, reconstructed agglomerates were in close affinity to the experimental agglomerates (Dadkhah, 2014). The structural properties of agglomerates evaluated by Dadkhah have been studied in detail using the TSA model. The results of the TSA model strongly agreed with the experiments (Dadkhah & Tsotsas, 2014). Knowing the coordination number and porosity of the agglomerates, the strength of the agglomerates was calculated, which could be used further to model breakage. The TSA model generated the agglomerates with monodisperse primary particles, so the further goal is to enhance the model by introducing size dispersity.

Earlier only the experimental agglomerates validated the porosity correlation (Eq. (4.8)) developed in (Singh & Tsotsas, 2019). Now, it was found to strongly coincide with the porosity of synthetic agglomerates generated using the TSA model. This validates the porosity correlation and the TSA model conjointly. Further, a new CVMC model has been developed by incorporating the TSA model to mimic the morphology of agglomerates formed. Two ways of implementing the TSA model in CVMC simulations were presented, and the in-situ implementation (denoted by CVMC-2) was very promising. Though this way of implementation is computationally slower, it has the advantage of breaking path for the goal of implementing real structural parameters to compute micro-scale mechanisms like droplet deposition and breakage.

Chapter 5 Polydispersity in agglomeration processes

This chapter is a modified version of the paper “Influence of polydispersity and breakage on stochastic simulations of spray fluidized bed agglomeration [in preparation]” with focus on size dispersity of primary particles.

5.1 Introduction

Size dispersity of primary particles is an important aspect to fully assess the morphological features of an agglomerate. In general, agglomerates typically consist of polydisperse primary particles. There is, thus, great interest in understanding the formation dynamics and structure of such agglomerates, and especially also their agglomeration rate, which strongly influences the design of the agglomerator. Several studies have been conducted to analyze the influence of polydispersity on the physical or chemical properties of fractal aggregates made of very small primary particles, such as on sintering, coagulation and radiation properties (Dastanpour & Rogak, 2016; Goudeli et al., 2016; Morán et al., 2018). However, the influence of polydispersity on the kinetics and morphology of SFB agglomerates has not yet been investigated. In the present chapter, a polydisperse TSA model is developed to generate the SFB agglomerates. This structural model is combined with the models that describe micro-scale processes and events in the comprehensive simulation framework.

5.2 Polydisperse aggregation model

An off-lattice particle-cluster polydisperse tunable sequential aggregation (PTSA) algorithm is developed. The input parameters are the number of primary particles (N_p) in the agglomerate to be constructed, the mean and standard deviation (σ) for the Gaussian (normal) distribution of radii of primary particles, and the fractal properties (D_f & k) of agglomerates. In this algorithm polydisperse spherical primary particles are added one by one using the following steps:

1. Normal distribution of radii of primary particles is generated with a given mean value and standard deviation for a given number of primary particles (N_p).
2. The first primary particle (seed) with a radius taken from the distribution is inserted at the center of a 3D simulation space.

3. The second primary particle is placed in contact with it, by selecting a point on the spherical surface of the seed.
4. The input fractal properties (D_f & k) are tuned, due to the limitation of the TSA model that has been described in detail in Chapter 4 (Singh & Tsotsas, 2020). The fractal dimension is tuned at fixed prefactor ($k = 1$) using the formulation developed by (Singh & Tsotsas, 2020),

$$D_{f,tuned} = D_f \left(\frac{\ln \frac{N_p}{1}}{\ln \frac{1}{k}} \right). \quad (5.1)$$

5. For the third and next particles, the correlation of (Filippov et al., 2000) with $D_{f,tuned}$ and $k = 1$ is used. The center of each primary particle to be added is on a sphere of radius R ,

$$R^2 = \frac{n^2 R_{p,n}^2}{n-1} (n)^{\frac{2}{D_{f,tuned}}} - \frac{n R_{p,n}^2}{n-1} - n R_{p,n}^2 (n-1)^{\frac{2}{D_{f,tuned}}}. \quad (5.2)$$

Here, n is from 3 to N_p and $R_{p,n}$ is selected sequentially from the primary particle radius distribution.

6. Randomly a point is selected on the sphere (of radius R) and contact and overlapping conditions are checked.
7. If there is a contact without overlapping then the new particle is attached to the growing cluster (initially a dimer).
8. Steps 5-7 are perpetuated until the targeted number of primary particles has been achieved.

An assumption has been made regarding the mass distribution of the individual particles in the agglomerate while calculating the distance of the new particle (R from Eq. (5.2)). The masses of primary particles are, namely, considered same. This approach is similar to (Skorupski et al., 2014). However, this algorithm is different

from the modifications proposed by FLAGE (Skorupski et al., 2014) while generating polydisperse agglomerates in the aspects of Table 5.1.

Table 5.1. Differences in algorithm of present PTSA model from FLAGE (Skorupski et al., 2014).

PTSA	FLAGE
Actual primary particle radius is used in Eq. (5.2).	Averaged primary particle radius is used.
Geometrical center of aggregate is calculated at each step (n) of the aggregation process.	Geometrical center is calculated once and kept constant.

It should be noted that relatively compact SFB agglomerates with the experimentally observed pairs of fractal property values (i.e., large fractal dimension D_f and large prefactor k , cf. Table B.2) cannot be generated with the original versions of the models proposed by (Filippov et al., 2000) and (Skorupski et al., 2014) because of the limitation of the prefactor (Singh & Tsotsas, 2020). (Morán et al., 2019) had proposed an algorithm by considering the masses of individual primary particles. When testing the algorithm from (Morán et al., 2019), it was though not possible to generate agglomerates resembling real SFB agglomerates (Dadkhah, 2014). This may be caused by combinations of large D_f with small k in (Morán et al., 2019), or by the hierarchical nature of this algorithm.

Figure 5.1 illustrates results of the generation of agglomerates by the PTSA model using 100 polydisperse primary particles with a mean radius of 260 μm and standard deviation varying from 0 to 30 % of the mean radius with an increment of 10. The fractal properties $D_f = 2.5$ and $k = 1.5$ have been taken to generate these exemplary agglomerates. These values are mid-range values of fractal properties determined from the experiments (cf. Table B.2). Radius of gyration of the agglomerate is calculated using the expression proposed by (Dastanpour & Rogak, 2016),

$$R_g = \sqrt{\frac{1}{\sum R_{p,i}^3} \sum_{i=1}^{N_p} R_{p,i}^3 \left(R_i^2 + \frac{3}{5} R_{p,i}^2 \right)}. \quad (5.3)$$

Here, R_i is the position vector of the i^{th} primary particle with radius, $R_{p,i}$ from the center of gravity (Section 3.3, Fig. 3.1) and N_p is the number of primary particles in the agglomerate. The values of R_g stated in Fig. 5.1 have been averaged over five realizations of each agglomerate.

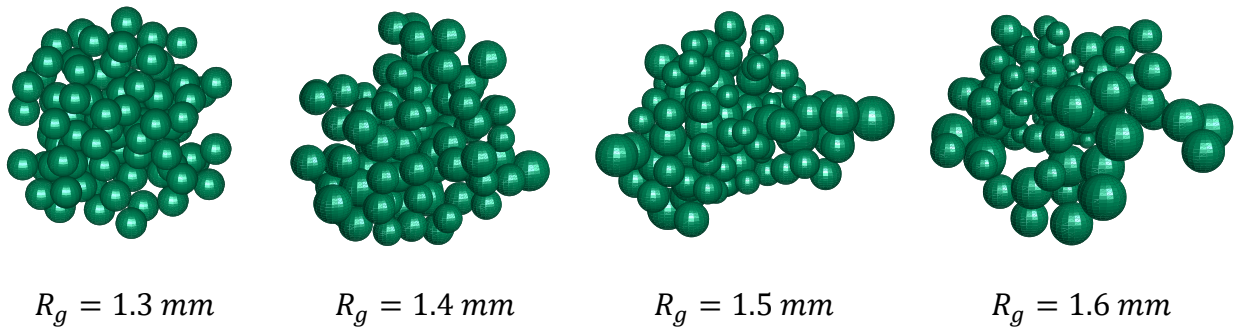


Fig. 5.1: Exemplary agglomerates (with $N_p = 100$) generated using the PTSA model with a mean radius of $260 \mu\text{m}$ and standard deviation varying from 0 to 30 % of the mean radius (from left to right, in steps of 10) with respective radius of gyration (averaged over five realizations).

5.3 Validation of PTSA model

The PTSA model is validated with the SFB agglomerates examined by Dadkhah in her experiments. For a more precise look, experiments A and D from (Dadkhah, 2014), see Appendix B, are considered. In both Exp. A and Exp. D the size diversity of the primary particles measured from individual agglomerates by Dadkhah was close to 10 % of its mean radius. Correspondingly, a standard deviation of $26 \mu\text{m}$ has been combined with the mean radius of $260 \mu\text{m}$. Based on the respective Gaussian distribution, a series of agglomerates made of different number of primary particles ranging from 5 to 250 at an increment of 5 have been generated using the PTSA model

at exactly those input values of the fractal dimension and prefactor which are given in Table B.2 for experiments A and D. For each agglomerate generated with the PTSA model the radius of gyration has been evaluated and averaged over five realizations before being plotted in double logarithmic scale against the number of primary particles in Fig. 5.2.

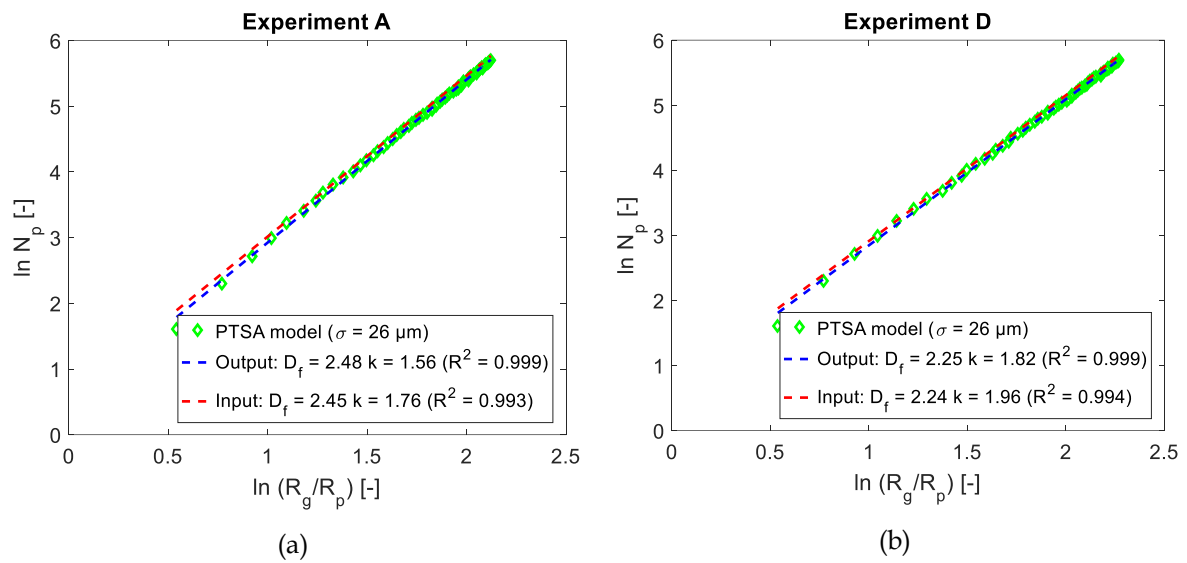


Fig. 5.2: Fractal properties comparison for experimental agglomerates and agglomerates generated by the PTSA model using the power-law relationship given in Eq. (3.7); Exp. A (a) and Exp. D (b) from Appendix B, Table B.2.

Output fractal properties extracted by means of the power-law from agglomerates generated with the PTSA model do not differ significantly from the respective input fractal properties, as it is shown in the Fig. 5.2. The power law is followed almost perfectly in both cases, with $R^2 = 0.999$ for the reconstructed and $R^2 = 0.993$ respectively $R^2 = 0.994$ for the input fractal property values of Exp. A and Exp. D, respectively. This level of agreement with the power law and of preservation of the fractal properties is sufficient for validation of the model. Even for 20 % standard deviation from the average primary particle size for the case Exp. A (not shown pictorially), $R^2 = 0.999$ is obtained with evaluated fractal properties and $R^2 = 0.951$ with input fractal properties, i.e. agreement with the power law remains excellent.

5.4 Effect of polydispersity on morphology using the PTSA model

Agglomerates with number of primary particles from 5 to 250 are aggregated at an increment of 5 using the PTSA model with a mean radius of 260 μm and standard deviation varying from 0 to 30 % of the mean radius of primary particles at an increment of 5. D_f and k are required to generate the agglomerates and are taken as $D_f = 2.5$ and $k = 1.5$. These values are the mid-range values (values of D_f and k of individual experiments are given in Table B.2) of SFB agglomerates examined by Dadkhah (Dadkhah & Tsotsas, 2014). The fractal properties and the mean radius of primary particles remain constant and only the standard deviation of the radius of the primary particles changes.

The morphological descriptors of each constructed agglomerate are obtained and averaged over five realizations. D_f and k of the series of agglomerates (with number of primary particles varying from 5 to 250 at an increment of 5) generated using the PTSA model are calculated using the power-law relationship (Eq. (3.7), which correlates the number of primary particles of the agglomerates, N_p , with their radii of gyration, R_g), on a double logarithmic scale for the entire sample, similarly to the Dadkhah's evaluation method (Dadkhah et al., 2012). Throughout this chapter R_p is the mean radius of the primary particles in the individual agglomerate.

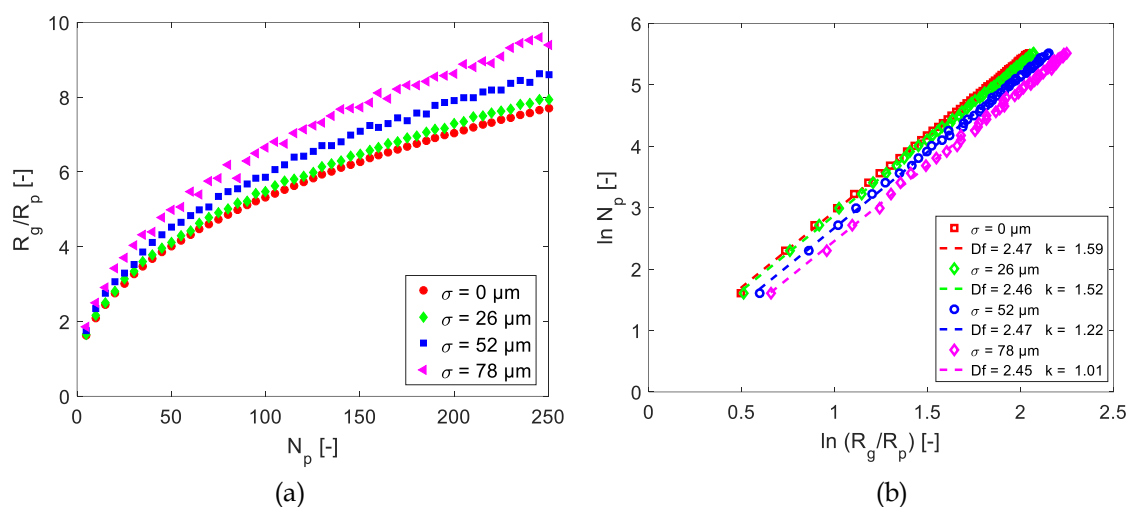


Fig. 5.3: Influence of the size dispersity of the primary particles on the radius of gyration of agglomerates (a) and fractal properties calculated using the power-law relationship given in Eq. (3.7) on a double logarithmic scale (b).

Values of R_g are computed (using Eq. (5.3)) for each agglomerate of a series, then averaged among five realizations and, finally, plotted in Fig. 5.3a. The average gyration radius (over 5 realizations) of the agglomerates at each N_p increases with increasing size dispersity (σ) of the primary particles. These averaged values of R_g for each agglomerate of the series are used to evaluate the fractal properties of the agglomerates on the logarithmic scale using the power-law relationship (Eq. (3.7)), and finally plotted in Fig. 5.3b.

Applying linear regression to the logarithms of N_p and R_g/R_p showed that the calculated fractal dimension is 2.46 ± 0.01 , independent of the dispersity of primary particle size. Similar behavior was reported in (Bushell & Amal, 1998; Tence et al., 1986). On the contrary, the fractal dimension was found to decrease monotonically with increasing dispersity of primary particles in (Eggersdorfer & Pratsinis, 2012), especially at high levels of dispersity. In the present work, the fractal dimension D_f does not change significantly. The prefactor (k) is also preserved quite accurately for standard deviation (σ) up to 10 % of the mean particle size. However, it decreases to

1.01 as the standard deviation of primary particle size increases to 78 μm (30 % of mean R_p), indicating that in such cases still more precise agglomerate reconstruction algorithms might be reasonable.

Values of ε_{agg} by the radius of gyration method and by the convex hull method are computed for each agglomerate of the series, then averaged among five realizations and, finally, plotted in Fig. 5.4.

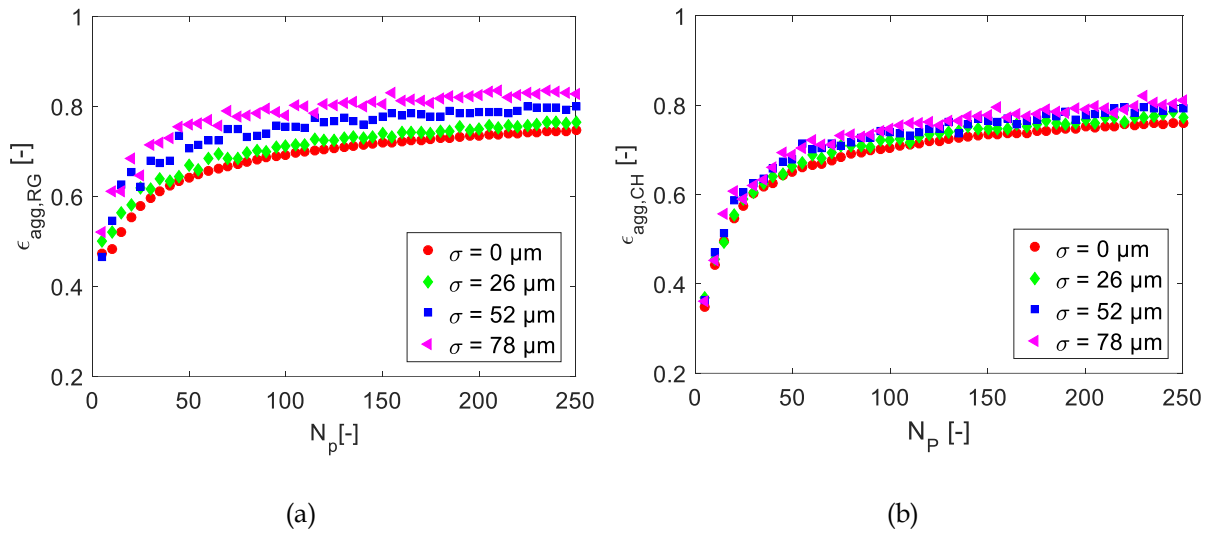


Fig. 5.4: Influence of polydispersity on the porosity of agglomerates by the radius of gyration method (a) and by the convex hull (b).

The trend from the plots in Fig. 5.4 shows that with increasing size dispersity of primary particles (σ), the agglomerates generated become more porous. The porosity of the agglomerates from the radius of gyration method and from the convex hull method increases as the dispersity of the primary particles increases.

Similarly, the surface area of volume equivalent sphere (VES, with porosity by the radius of gyration method) and the surface area of the agglomerates from the convex hull method are computed for each agglomerate of the series, then averaged among five realizations and, finally, plotted in Fig. 5.5. The trend from the plots in Fig. 5.5

shows that with increasing size dispersity of primary particles (σ), the surface area of VES (with porosity by the radius of gyration method) and the surface area of the agglomerates from convex hull method increase.

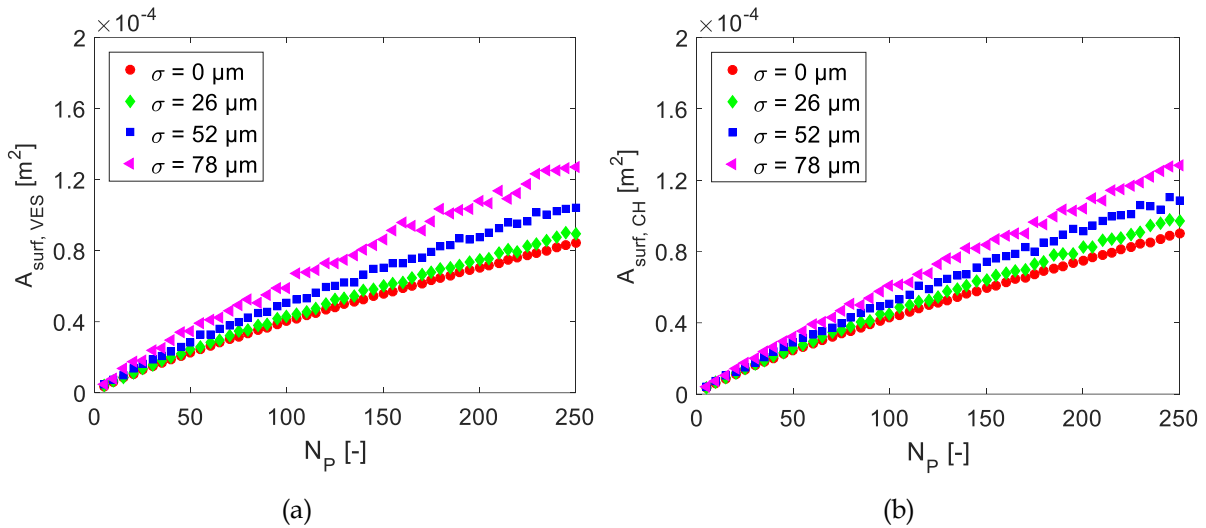


Fig. 5.5: Influence of polydispersity on the surface area of VES with porosity by the radius of gyration method (a) and on the surface area of agglomerates by the convex hull (b) method.

(Dastanpour & Rogak, 2016) also found the radius of gyration and the surface area of aggregates to increase with increasing size dispersity of primary particles (at constant geometric mean primary particle size). In contrast, the porosity of packed beds decreases with increasing dispersity (Schulze et al., 2015). This is due to the methods used to create the packings, such as sedimentation or settling of particles with rolling and vibration, which lead to a higher solid volume fraction (de Klerk, 2003).

5.5 Effect of polydispersity on kinetics using the CVMC model

In order to estimate the kinetics, the CVMC-2 simulation framework is used and the monodisperse aggregation model (TSA model) is replaced with the PTSA model. The experimental data reported by Dadkhah (Dadkhah, 2014) are taken to construct the

agglomerates using the PTSA model. These experiments were performed in batch mode with glass beads as primary particles and HPMC in aqueous solution as a binder. A brief description of the experiments with morphological descriptors examined is given in Appendix B.

Overall simulations have been performed according to the scheme described in Chapter 2 using the same experimental (Dadkhah, 2014) and simulation parameters (given in Table 5.2) as in (Singh & Tsotsas, 2019). Specifically, two sets of simulations for the experiment A (Dadkhah, 2014) with inlet fluidization gas temperature of 60°C and binder (HPMC) mass fraction of 2 wt. % have been carried out for 10 min. In the first set the diameter of the formed agglomerates is the diameter of VES and in the second set surface area equivalent sphere (AES) is used to calculate the diameter, where the surface area is obtained with the convex hull method by constructing the agglomerates using the PTSA model.

Table 5.2. Experimental and simulation parameters.

Bed mass	M_{bed}	500	g
Primary particle density	ρ_p	2500	kg/m ³
Binder density	ρ_l	998.5 – 1024.0	kg/m ³
Binder addition rate	\dot{M}_l	200	g/h
Gas mass flow rate	\dot{M}_g	130	kg/h
Mean primary particle radius	R_p	260	μm
Droplet diameter	D_d	80	μm
Collision frequency prefactor	F_{coll}	10	1/m
Fluidization velocity	u_o	1.912	m/s
Particle surface asperities height	h_a	10	μm
Particle restitution coefficient	e	0.8	-
Binder contact angle	θ	40	°

The formed agglomerates are reconstructed using the PTSA model with a mean radius of primary particles as 260 μm and a standard deviation varying from 0 to 30 % of the mean radius. In order to generate the agglomerates using the PTSA model, fractal properties are taken from the empirical correlation of (Singh & Tsotsas, 2019) (given in Eq. (3.18) and Eq. (3.17)) by inserting the key operating parameters of spray fluidized bed (SFB) agglomeration, namely inlet fluidization gas temperature in $^{\circ}\text{C}$ and binder mass fraction in wt. %.

The kinetics of the agglomeration process is expressed in terms of the relative diameter of the agglomerates over time. The relative diameter of the agglomerates is the ratio of Sauter mean diameter of the population and the initial diameter (twice the R_p) at a given instant of time.

Figure 5.6 shows that the growth rate of the agglomeration process increases with an increase in the standard deviation (σ) of primary particle size from 0 to 30 % of its mean radius, regardless of the choice of the method used to obtain the diameter of formed agglomerates. In addition, the AES method is very sensitive over the spread of primary particle size. The surface area obtained with the convex hull method (as indicated in Section 5.4) provides quantitatively usable information about the morphology of agglomerates with different size dispersity of the primary particles. Therefore, the AES method is preferable for determining the diameter of SFB agglomerates. Hereafter, the CVMC model with AES method of determining agglomerate diameter is referred to as CVMC-3.

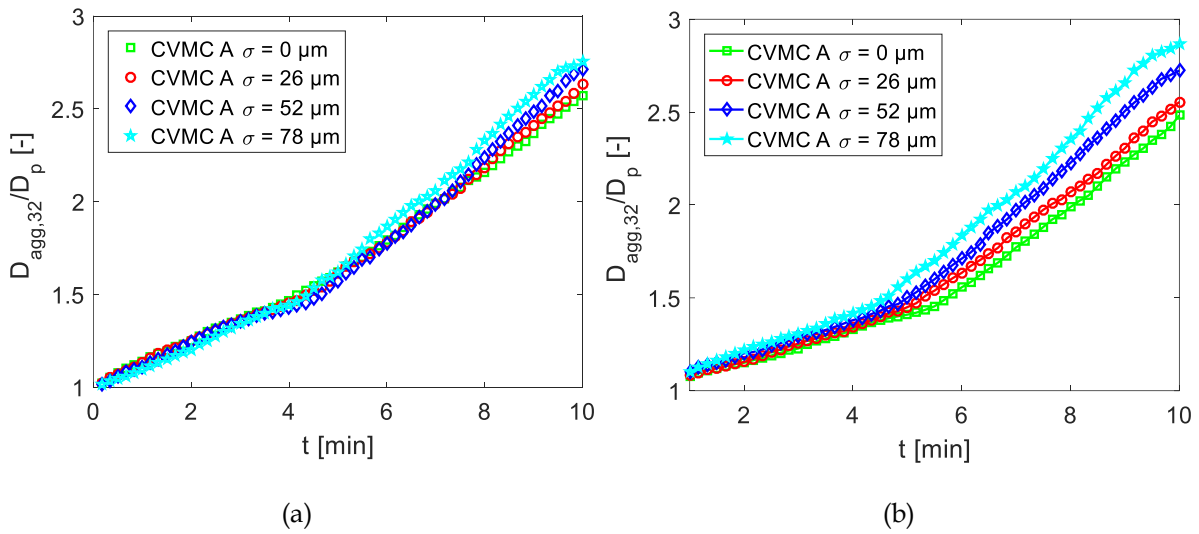


Fig. 5.6: Influence of polydispersity on the kinetics of SFB agglomeration process simulated using the CVMC model by considering the formed agglomerates as VES (left) and AES (right).

The size dispersity of the primary particles influences the morphology of the agglomerates, which in turn affects the Stokes criterion for coalescence. The first effect of primary particle dispersity on the growth rate is simply that the physical size of the agglomerate increases with increasing dispersity. Second, it is easier to meet the Stokes coalescence criterion for collisions on wet positions. Similar behavior was reported in (Goudeli et al., 2016) while investigating the influence of polydisperse primary particles on the coagulation of agglomerates.

5.6 Conclusion

In this study, a tunable aggregation model has been developed to numerically generate SFB agglomerates with polydisperse primary particles. Fractal properties (D_f and k) were precisely preserved for agglomerates with a standard deviation of 10 % of mean primary particle size, which coarsely corresponds to the available experimental results. Fractal dimension D_f is preserved also for much higher standard

deviations of primary particle size, but a shift of the fractal prefactor k is then observed. Hence, it might be reasonable to improve the model for high levels of size dispersity of the primary particles and/or very large agglomerates according to (Morán et al., 2019; Morán et al., 2020).

The influence of primary particle size dispersity on the morphology, growth and size distribution of SFB agglomerates has been investigated (by constructing in total around 3000 agglomerates using the PTSA model). It was found that the radius of gyration, the porosity (by the radius of gyration and the convex hull methods) and the surface area (area of VES and from the convex hull) increase with increasing size dispersity of the primary particles. Regardless of the tuned fractal properties when creating the agglomerates with the PTSA model, the fractal dimension remained almost constant, but the prefactor was reduced with increasing dispersity of the primary particles. Thus, it is concluded that the assumption of an average primary particle size (considered monodisperse), as often applied in particle characterization, hardly influences the fractal dimension, but clearly overestimates the prefactor in case of polydisperse primary particles for all SFB agglomerates. The agglomeration rate was increased with increasing size dispersity of the primary particles (from $\sigma = 0$ to 30 % of the mean radius of primary particles).

Chapter 6 Breakage of SFB agglomerates

This chapter is a modified version of the paper “Influence of polydispersity and breakage on stochastic simulations of spray fluidized bed agglomeration [in preparation]” with focus on breakage of already formed agglomerates.

6.1 Introduction

Breakage of already formed agglomerates is an important mechanism that decreases the growth rate and can lead to an equilibrium between growth (agglomeration) and rupture (binary breakage), which is typical for fluidized bed processes. A large number of parameters influence the agglomerate breakage, e.g. bed hydrodynamics, morphology and bonding material. However, most simulations use average mechanical and structural parameters that eliminate the complexity of real agglomerates from the beginning. Therefore, the simulation results cannot accurately predict the properties of individual agglomerates, particularly those bound by binders (Iveson et al., 2001). Agglomerates can break due to collisions with equipment walls or other particles (primary particles or agglomerates). Here, only the second mechanism has been considered.

6.2 Breakage model

Strength of agglomerates provides the foundation for the development of a dynamic breakage model by incorporating realistic morphology of SFB agglomerates (Singh & Tsotsas, 2020). Agglomerate strength (σ_T) depends on the cohesive force between primary particles and agglomerate morphology and is calculated using the Rumpf model (Rumpf, 1958) to

$$\sigma_T = \frac{\text{MCN}(1-\varepsilon_{agg})F_c}{\pi D_p^2}. \quad (6.1)$$

Here, MCN and ε_{agg} are mean coordination number and porosity of an agglomerate, F_c is the mean cohesive force between the primary particles of mean diameter D_p . MCN and ε_{agg} are necessary to calculate the strength of agglomerate and are evaluated from the PTSA model by constructing the agglomerate.

In SFB agglomeration, pendular liquid bridges are formed when two primary particles are in contact. Liquid bridge forces are the most important forces and can occur both statically through capillary action and dynamically through viscous forces. Under dynamic conditions, however, the viscous forces exceed the capillary forces in the liquid bridge (van den Dries & Vromans, 2002). Due to the continuous collision of agglomerates with walls and other particles (agglomerates and primary particles), the associated primary particles are in relative motion. The viscous force of a liquid bridge due to the binder is given by Reynolds' lubrication equation (Seville et al., 2000) to

$$F_c = \frac{3\pi\mu_l D_p^2 u_c}{2h_{gap}}. \quad (6.2)$$

Here, μ_l is the viscosity of the binder, u_c the collision velocity of the particles with a mean diameter D_p and h_{gap} the interparticle gap. The viscosity of the binder is a function of binder concentration in the droplet (Terrazas-Velarde, 2012) according to Eq. (2.37).

The binder concentration depends on the amount of water present in the droplet. The water contained in the droplet is evaporated due to drying by inlet fluidized gas used as a drying agent. As the droplet dries, the mass of solute (binder) remains constant and the amount of water M_w decreases. This leads to an increase in binder mass fraction x_b and, therefore, increase in viscosity μ_l of binder solution. Eventually, the binder content and viscosity increase due to the drying process.

The interparticle gap in an agglomerate is estimated by considering the pore space between primary particles in an agglomerate as a bundle of cylindrical capillaries having the same surface area as the primary particles assembly (van den Dries & Vromans, 2002) and expressed as

$$h_{gap} = \frac{2\varepsilon_{agg}D_p}{3(1-\varepsilon_{agg})}, \quad (6.3)$$

where ε_{agg} is the porosity calculated using gyration method by constructing the agglomerate using the PTSA model with a mean primary particle diameter D_p .

Substituting the cohesive force, F_c , from Eq. (6.2) with interparticle gap, h_{gap} , from Eq. (6.3), agglomerate strength from Eq. (6.1) becomes

$$\sigma_T = \frac{9\mu_l u_c MCN(1-\varepsilon_{agg})^2}{4D_p \varepsilon_{agg}}. \quad (6.4)$$

The breakage model in the present work is based on the ratio of the externally applied kinetic energy to the energy required for deformation represented by the Stokes deformation number (Liu et al., 2009)

$$St_{def} = \frac{\rho_{agg} u_c^2}{2\sigma_T}, \quad (6.5)$$

where σ_T is calculated from Eq. (6.4), ρ_{agg} is agglomerate density and the collision velocity, u_c , as stated previously is chosen randomly by assuming a normally distributed function around a mean value equal to $0.5u_0$ and a standard deviation of 0.1 m/s. Agglomerate density is calculated as

$$\rho_{agg} = (1 - \varepsilon_{agg})\rho_p \quad (6.6)$$

where ε_{agg} is the porosity of an agglomerate calculated using gyration method by constructing the agglomerate using the PTSA model and ρ_p is primary particle density.

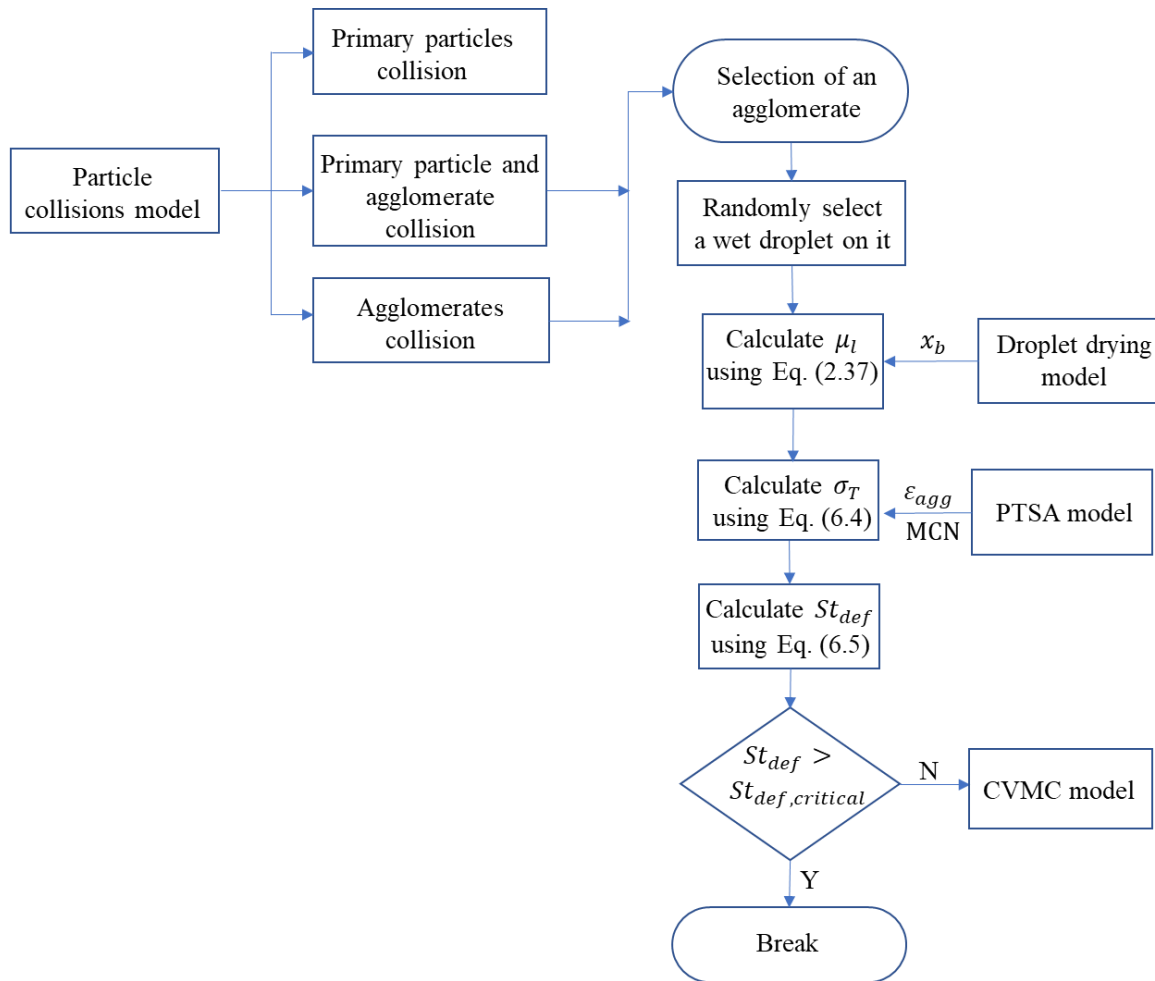


Fig. 6.1: Simplified diagram of the breakage algorithm used in the present work.

A flowchart of the breakage model is given in Fig. 6.1. Immediately after the unsuccessful collision between a pair of particles (with at least one agglomerate), in the case of two colliding agglomerates, one agglomerate is randomly selected from the pair of colliding particles or, in the case of a primary particle and an agglomerate collision, the (only) agglomerate is selected. It should be noted that the breaking of primary particles is not considered in this work. Therefore, if the colliding particles are primary particles, they are excluded from the breakage selection. A droplet is

randomly selected from the wet droplets (completely dried droplets are ignored) deposited on the selected agglomerate. The properties of the selected droplet are used to mimic the properties of all bridges in the agglomerate, assumed to be uniform, when calculating the cohesive force. The strength of the agglomerate is calculated using the cohesive force and morphological descriptors. Morphological descriptors like porosity and mean coordination number are evaluated by constructing the agglomerate using the PTSA model (with a mean primary particle radius R_p and a standard deviation). The agglomerate is broken when the Stokes deformation number is greater than the critical Stokes deformation number.

Many researchers have assumed the critical Stokes deformation number equal to critical Stokes coalescence number (Tardos et al., 1997; Terrazas-Velarde et al., 2011a). However, in the case of SFB agglomeration, the critical Stokes deformation number is expected to be far from the critical Stokes coalescence number because of the rapid solidification rates of the binder, which lead to a stronger bond (Terrazas-Velarde et al., 2009). For the sake of simplicity, the critical Stokes deformation number is assumed to be equal to twice the critical Stokes coalescence number (given by Eq. (2.39)).

In this study, random binary breakage occurs where an agglomerate is divided into two smaller agglomerates, each with a random number of primary particles while retaining the original number of primary particles present in the parent agglomerates. It should be noted that the CVMC simulation invokes the PTSA model after each agglomeration or breakage event. The PTSA model performs five realizations for each agglomerate at each call. The morphological descriptors (like radius of gyration, porosity and MCN) are averaged over those five realizations.

6.3 CVMC simulation incorporated with breakage model

The comprehensive CVMC simulation discussed in Chapter 5 (denoted by CVMC-3) has been incorporated with the breakage model and then called CVMC-4. CVMC-4 is then used to simulate the SFB agglomeration by treating the simulation box as a virtual granulator. The modeling scheme is shown in Fig. 6.2.

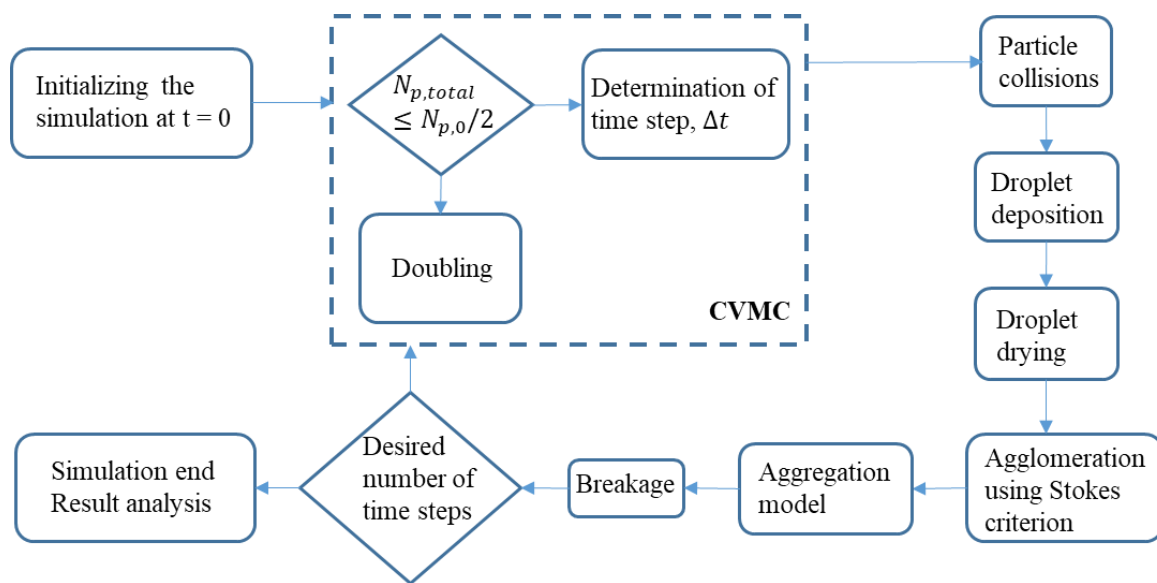


Fig. 6.2: CVMC modeling scheme for spray fluidized bed agglomeration.

Initially, the simulation box, which is considered as a representative sample of the particle population, consists of 1000 primary particles. The number of particles in the simulation box changes depending on the process, such as agglomeration or breakage, which dominates during the simulation. Aggregation model is called after each agglomeration/breakage event to replicate the structure and calculate the morphological descriptors. For each call, the PTSA model performs five realizations for each agglomerate and the evaluated morphological descriptors, namely porosity and MCN, are averaged over those five realizations to be used further in the micro-scale modeling of breakage.

6.4 Effect of breakage on kinetics using the CVMC model

In order to investigate the influence of the breakage mechanism on the kinetics of SFB agglomeration, two CVMC simulations for experiment A (reference experiment) were performed. In the first simulation, the breakage model as described in Section 6.2 was activated (CVMC-4) and for the second (CVMC-3) it was deactivated. The formed agglomerates for both simulations are constructed using the PTSA model (described in Chapter 5) with a mean radius of primary particles as $260 \mu\text{m}$ and a standard deviation of $26 \mu\text{m}$ (10 % of the mean radius). It should be noted from Table B.2 and Fig. B.1 that the standard deviation of the radius of primary particles evaluated from tomographic data by Dadkhah is around 10 % of the mean radius. Moreover, the glass beads (primary particles) used for the experiments in (Dadkhah, 2014) were also found to be normally distributed (Gaussian distribution) with standard deviation of around 10 % of the mean radius by Camsizer measurements (Fig. B.1).

Fractal properties (D_f and k) for the PTSA model are taken from Eqs. (3.18) and (3.17) by inserting the inlet fluidized gas temperature and the binder concentration. The kinetics of the agglomeration process is expressed in terms of the relative growth of the agglomerates over time. The diameter of the formed agglomerates is the diameter of AES, where the surface area is obtained by the convex hull method by constructing the agglomerates using the PTSA model.

Figure 6.3 shows the agglomerate growth (in the left hand-side plot) and the particle size distribution after 23 minutes (in right hand-side plot) according to the CVMC simulations with and without activating the breakage model. A gradual reduction in the rate of agglomeration is achieved in case of breakage, as shown in Fig. 6.3a, leading to an equilibrium where growth is almost constant over time. The CVMC simulation with breakage mechanism (CVMC-4) ends after 33 minutes, whereas without breakage mechanism (CVMC-3), the simulation is stopped at 23 minutes because the

agglomerates become too large to simulate. Breakage decreases the overall growth rate of the agglomerate process. If agglomeration and breakage occur simultaneously, it is possible that the two processes balance each other out and lead to a uniform size distribution (Tan et al., 2004). It accomplishes the equilibrium between growth (agglomeration) and rupture, which is typical for fluidized bed processes.

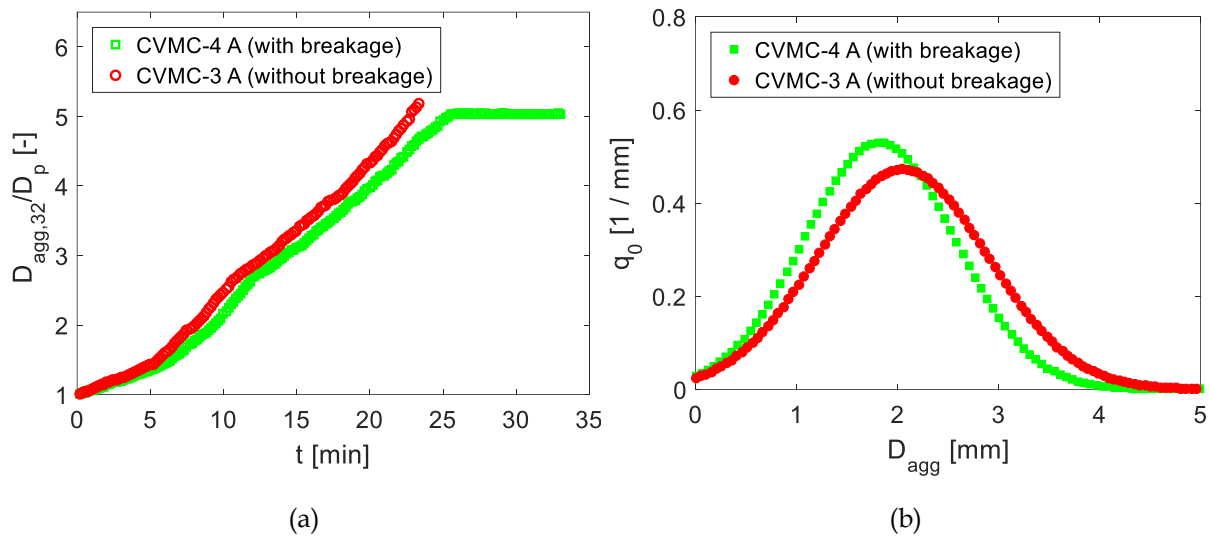


Fig. 6.3: Influence of breakage on the kinetics (a) and particle size distribution (b) of SFB agglomeration process simulated using the CVMC models for Exp. A.

In order to validate the breakage model, overall growth rate is calculated. It is defined as the ratio of the difference between Sauter mean diameter of the final agglomerates at the end of the process and the diameter of primary particles to the duration of the trial,

$$r_G = \frac{D_{agg,32,t} - D_p}{t} . \quad (6.7)$$

Upon implementing the breakage model, the overall growth rate ($r_G = 1.06 \mu\text{m/s}$) after 33 minutes is almost equal to the growth rate ($r_G = 1.07 \mu\text{m/s}$, given in Table B.2 for Exp. A) examined by Dadkhah in her experiments after 37 minutes (Dadkhah &

Tsotsas, 2014). Thus, the current breakage model can be considered as validated and will be further used in CVMC simulations for other experiments in the next chapter.

Figure 6.3b shows the particle size distribution at time $t = 23$ min. The arithmetic mean diameter of the particle size distribution is 1.82 mm with breakage and 2.05 mm without breakage. In addition, the interquartile range (difference between the 75th and 25th percentile) also decreases from 1.16 mm (without breakage) to 0.98 mm (with breakage).

6.5 Conclusion

It has been postulated that agglomerate breakage is closely related to agglomerate strength, which can be calculated from the Rumpf correlation (Rumpf & Schubert, 1974), by including the viscous force of the liquid bridges and the morphological descriptors of the agglomerate. The Stokes deformation number calculated from the impact velocity and the dynamic strength of the agglomerate gave a good indication of whether or not the agglomerate of a particular formulation will break.

A dynamic breakage model has been developed based entirely on the physical properties of the formulations such as binder viscosity, agglomerate porosity, mean coordination number and primary particle size. Further, an enhanced CVMC model (CVMC-4) has been developed by implementing the breakage model in the CVMC framework. It was found that the agglomeration rate decreases when breakage is considered, and an equilibrium between growth and rupture can be established.

Chapter 7 Influence of process parameters on agglomeration behavior

This chapter describes the overall kinetics and morphological features of SFB agglomerates formed under different operating conditions using a CVMC model. Focus of this chapter is to discuss the proposed CVMC model (CVMC-4) by comparing its results with the findings of experiments.

7.1 Introduction

After having incorporated the polydisperse structure model and dynamic breakage model in the CVMC framework to obtain model version CVMC-4, the influence of key operating conditions, namely inlet fluidization gas temperature and binder mass fraction, are analyzed. Further, the results from the enhanced CVMC model (CVMC-4) are compared with the experimental results from (Dadkhah, 2014). Experimental parameters are the same as given in Table B.1. Simulation parameters used for individual simulations in relation to the respective experimental trials are given in Appendix D.

The formed agglomerates are reconstructed using the PTSA model with a mean radius of primary particles as 260 μm and a standard deviation of 26 μm (10 % of the mean radius). It should be noted from Table B.2 and Fig. B.1 that the standard deviation of the radius of primary particles evaluated by Dadkhah is indeed around 10 % of the mean radius. Fractal properties for the PTSA model are taken from Eqs. (3.18) and (3.17) by inserting inlet fluidization gas temperature and binder mass fraction for the respective experiment according to Table B.2.

7.2 Influence of inlet fluidization gas temperature

In order to investigate the influence of inlet fluidizing gas temperature on agglomeration behavior, simulations with the CVMC-4 model are carried out for 10 min and compared with the corresponding experiments B, A and C at 30°C, 60°C and 90°C, respectively.

The overall growth rate in Table 7.1 expresses the kinetics of the process at different temperatures (Exp. B, A and C with increasing temperature) and binder concentration (Exp. A, D and E with increasing concentration). The growth rate evaluated from the

present model is compared with the CVMC-2 model from Chapter 4 (Singh & Tsotsas, 2020) and experiments (Dadkhah, 2014). The CVMC-2 model from Chapter 4 (Singh & Tsotsas, 2020) constructed the agglomerates using monodispersed primary particles and the breakage of already formed agglomerates was not implemented.

Table 7.1. The overall growth rate for different experiments and respective simulations with and without breakage.

Trial	Overall growth rate ($\mu\text{m/s}$)				
	A	B	C	D	E
CVMC-4 model	1.18	1.85	0.79	3.84	5.89
CVMC-2 model	1.78	2.91	1.21	4.48	6.81
Dadkhah's experiments	1.07	1.15	0.63	3.79	8.20

In addition, the diameter of the agglomerates formed in the current CVMC-4 model is the diameter of AES, where the surface area is obtained by the convex hull method by constructing the agglomerates using the PTSA model, whereas for the CVMC-2 model from Chapter 4 (Singh & Tsotsas, 2020) the diameter of VES was used with the porosity by the radius of gyration method to evaluate the growth kinetics. The comparison of the agglomerate diameter evaluated by AES and VES methods for all the experiments is given in Appendix C.

It can be assessed from Table 7.1 that, as the temperature of the inlet gas increases the growth rate decreases, due to faster drying of the binder droplets by the fluidizing gas used as a drying agent. As the temperature increases the droplet size decreases and the probability of particle colliding at a wet spot decreases. Consequently, the agglomeration growth rate decreases as shown in Fig. 7.1a.

The inlet gas temperature also influences the morphology of the agglomerates. With increasing temperature, the binder droplets become smaller so that the liquid bridges

created after successful particle-particle collisions are also smaller and thus weaker and easier to break. Consequently, more bridges are necessary to stabilize the formed agglomerates leading to structures that are more compact. Thus, high temperature results in higher fractal dimension and lower agglomerate porosity, decreasing the diameter of the final agglomerates formed, therefore making them compact. The particle size distributions for different inlet temperatures at 10 min are shown in Fig. 7.1b. PSD is always broader at low fractal dimension because the porosity is high and the formed agglomerates are large.

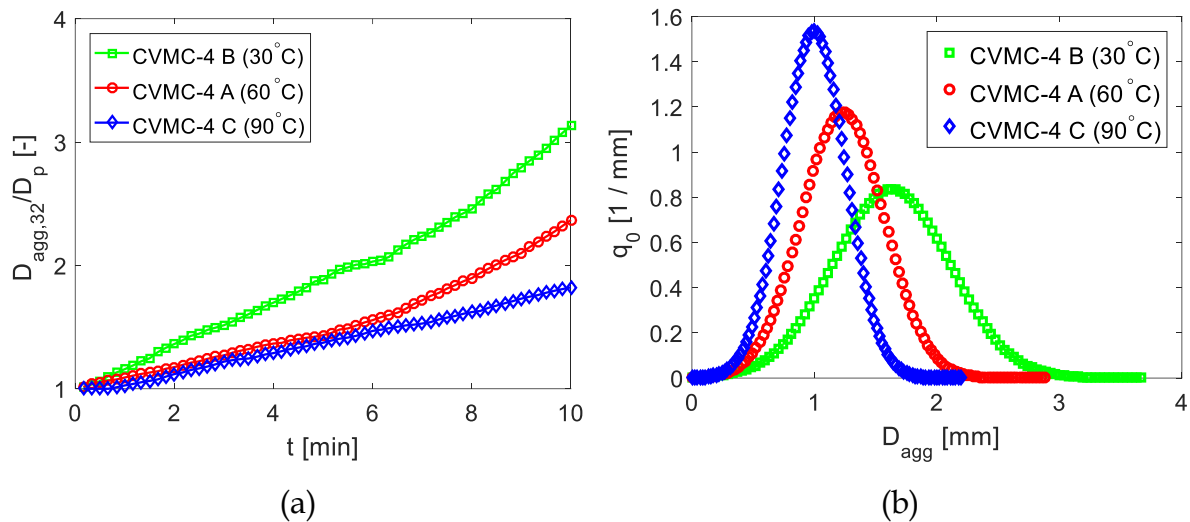


Fig. 7.1: Effect of gas inlet temperature on the relative average diameter of the agglomerates (a) and on the PSD at 600 s (b).

7.3 Influence of initial binder mass fraction

To study the effect of binder mass fraction on the process, simulations with different binder mass fractions, $x_b = 2, 6$ and 10 % were performed with CVMC-4 model for 10 min corresponding to experiments A, D and E respectively. As the binder concentration increases, binder droplets become more viscous and the fulfillment of the Stokes criterion upon collision on wet spots becomes easier. A more viscous liquid

dissipates a high fraction of collision energy. Therefore, the agglomeration growth rate increases as shown in Fig. 7.2a.

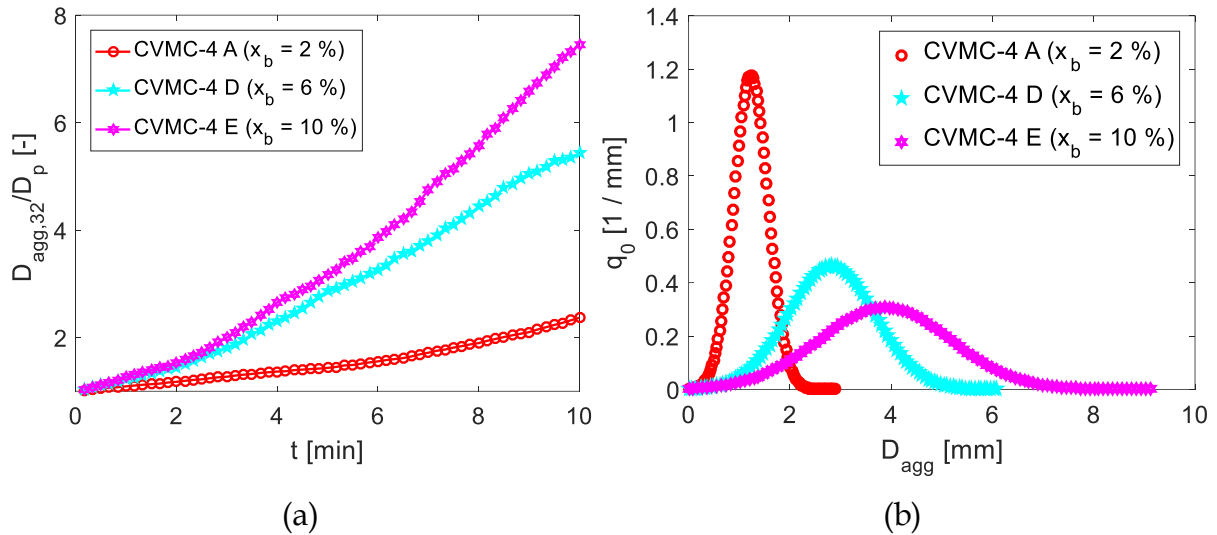


Fig. 7.2: Effect of binder concentration on the relative average diameter of the agglomerates (a) and on the PSD at 600 s (b).

The morphological changes that occur as the binder mass fraction increases can also be explained. The particle size distributions for different binder concentrations at 10 min are shown in Fig. 7.2b. Bridges formed out of high binder concentration are stronger than with less binder, as they are more viscous. Agglomerates formed at high binder concentration are loosely arranged in space and have a large probability to survive in a fluidized bed. Consequently, the agglomerates formed are large and so the fractal dimension of agglomerates decreases and their porosity increases. As a result, the formed agglomerates are porous and tenuous and particle size distribution is shifted to the right from Exp. A to Exp. D and, finally, to Exp. E.

7.4 Comparison of enhanced CVMC model (CVMC-4) with experiments

Simulations have been carried out for all the experiments from Table B.2 (Appendix B) by means of present enhanced CVMC model with the breakage mechanism (CVMC-4 model, as described in Section 6) for 10 minutes. Simulation parameters and corresponding experimental parameters are the same as given in Table 3.4 and Table B.1, respectively. The formed agglomerates are reconstructed using the PTSA model with a mean radius of primary particles as 260 μm and a standard deviation of 26 μm . Fractal properties for the PTSA model are taken from Eqs. (3.18) and (3.17) by inserting inlet fluidized gas temperature and binder concentration for respective trials from Table B.2.

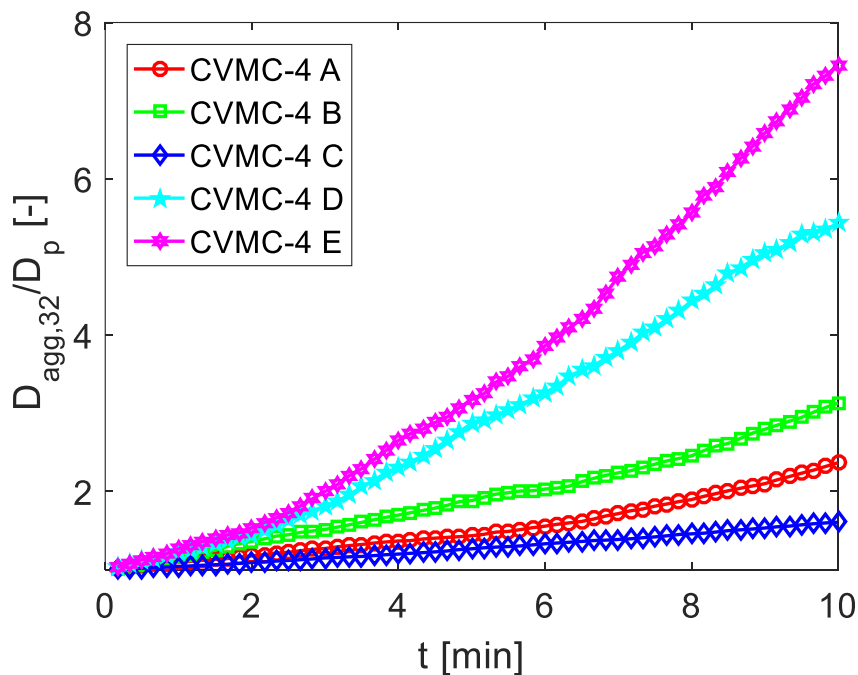


Fig. 7.3: Relative average diameter with respect to time simulated using the CVMC-4 model for the different experiments.

Figure 7.3 shows that the growth rate decreases with increasing temperature of the inlet gas (corresponding to experiments B, A and C at 30 °C, 60 °C and 90 °C, respectively) and increases with increasing binder concentration ($x_b = 2, 6$ and 10 %, corresponding to the experiments A, D and E, respectively). This can be explained by the two underlying mechanisms, namely aggregation and breakage.

Aggregation is a dominant mechanism in determining the growth rate. It is described by the probability of successful collisions. As the temperature increases (for Exps. B, A and C, respectively), the droplet size decreases and the probability of particle collision at a wet location decreases. This is due to the faster drying of the binder droplets; at higher temperatures fewer droplets are available. This means that the total number of available (wet) droplets decreases, which in turn reduces the probability of a successful collision. Consequently, the agglomeration growth rate is reduced, as shown in Fig. 7.3. On the contrary, in simulations with increasing binder concentration ($x_b = 2, 6$ and 10 %, corresponding to the experiments A, D and E, respectively), the viscous force of the binder increases and the fulfillment of the Stokes criterion for wet impact becomes easier. Therefore, the agglomeration growth rate increases as shown in Fig. 7.3. The trends are similar to Chapter 4 (Singh & Tsotsas, 2020), however, the measured overall growth rates (given in Table 7.1) are lower than predicted in (Singh & Tsotsas, 2020). This is the consequence of the breakage mechanism having been incorporated in the present CVMC model.

The mechanism of breakage is described by the strength of the agglomerate, calculated using Eq. (6.1). The higher the strength, the less likely it is that the agglomerate will break. An illustration of strength with collision velocity equal to $0.5u_0$ of different agglomerates that have formed under different operating conditions, measured by Dadkhah (Dadkhah et al., 2012), is given in Fig. 7.4. Agglomerates are constructed using the PTSA model with a mean primary particle radius as 260 μm and a standard

deviation of 26 μm . The effect of drying on binder droplets is not taken into account in this illustration, rather initial binder content is used to evaluate the viscosity of binder. However, if drying is activated the trends shown in Fig. 7.4 remain the same.

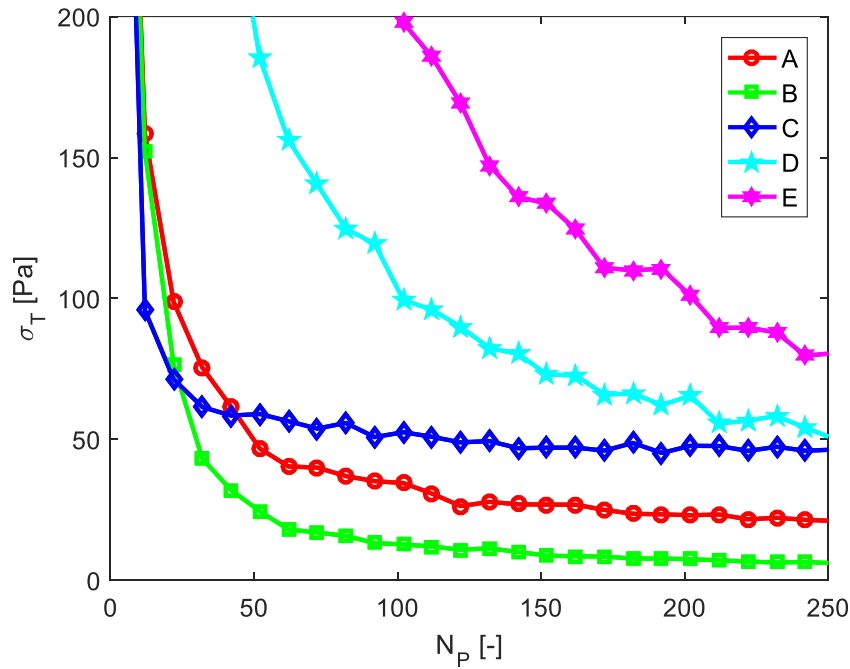


Fig. 7.4: Comparison of strength with collision velocity equal to $0.5u_0$ for different agglomerates that have formed under different operating conditions, measured by (Dadkhah et al., 2012) and constructed using the PTSA model for different experimental trials.

The strength of an agglomerate depends on the viscosity of the binder and the morphology (porosity and mean coordination number) of the agglomerate. The strength of a wet agglomerate increases with increasing binder content (for Exps. A, D and E), and decreases with increasing number of primary particles (for all experiments). The argument is that the binder droplets are more viscous at a higher binder content (highest for Exp. E with a binder content of 10 wt. %). A more viscous liquid dissipates a higher proportion of the collision energy and the resulting liquid bridge is less likely to break. Moreover, if the binder content is kept constant (for Exps. B, A and C), the morphology of the agglomerates plays an important role, with the

compact agglomerates (high D_f and low porosity) of Exp. C being stronger than the tenuous agglomerates (low D_f and high porosity) of Exp. B.

It should be noted that the mean radius of the primary particles is assumed to be 260 μm . This is the average size of the primary particles used by (Dadkhah, 2014), as measured separately by particle image projections (Camsizer). The mean radius of 260 μm and the standard deviation of 26 μm used here differ from the radius of the primary particles for individual agglomerates evaluated from tomography data. This is especially important for Exp. B and Exp. E in particular (cf. mean and standard deviation of R_p in Table B.2). It means that the agglomerate diameter, which is reflected in the calculation of the growth rate in Table 7.1 and kinetics in Fig. 7.3, cannot be consistently obtained with the same quality when setting the mean radius of primary particles at 260 μm and the standard deviation at 26 μm . This could be the reason for the deviation of the calculated growth rate for Exp. E from the experimental value in Table 7.1.

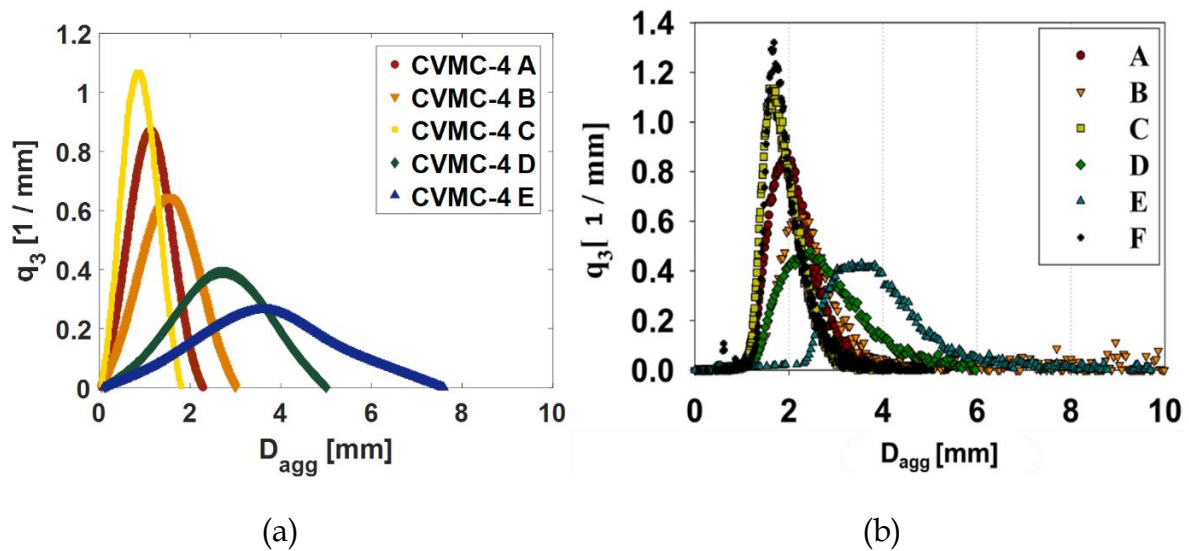


Fig. 7.5: Particle size distribution for different experiments as simulated with the CVMC-4 model after 10 minutes (a) and from experiments conducted by (Dadkhah & Tsotsas, 2014) (b).

The particle size distributions for different operating conditions as simulated by means of the CVMC-4 model after 10 min are shown in Fig. 7.5a. The operating conditions like inlet fluidization gas temperature corresponds to experiments B, A and C at 30 °C, 60 °C and 90 °C, respectively and binder mass fraction $x_b = 2, 6$ and 10 % corresponding to the experiments A, D and E, respectively. The distributions are in agreement with the experimental findings of (Dadkhah & Tsotsas, 2014), as shown in Fig. 7.5b.

Chapter 8 Conclusions and outlook

This chapter contains the main conclusions with possible improvements of the proposed models and an outlook on future research.

8.1 Conclusions

Spray fluidized bed agglomeration is considered as a complex network of discrete micro-scale events and processes between particles (primary particles and agglomerates) and binder droplets. Such micro-scale events and processes are collisions between particles, droplet deposition, deposited droplet drying, liquid bridge formation and agglomerate breakage that occur in series and in parallel. A comprehensive stochastic simulation, with micro-scale mechanisms happening within the fluidized bed has been presented in this study. The simulation was solved by the constant volume Monte Carlo method, a stochastic and discrete event-driven method based on the use of randomly generated numbers with periodical particle regulation.

Morphological descriptors of the agglomerates are imperative in understanding product characteristics that affect their behavior. A cross-correlation between the main morphological descriptors has been developed to predict the size of agglomerates consisting of monodispersed spherical primary particles. The formulated correlation confirms that the morphological data from (Dadkhah, 2014) are consistent. It has been shown that agglomerate size can be more accurately predicted from the number of primary particles by known fractal dimension and prefactor of an agglomerate sample, than by known average porosity of the agglomerates of the same sample.

Numerically, the interest in structure formation by aggregation of small particles has motivated the search for simulation algorithms that could provide comparable results to experimental observations. The morphology of agglomerates provides a quantitative link between microstructural features and their macroscopic properties. From the plethora of aggregation models in literature, the PC aggregation model offers a good prognosis for SFB agglomerates. The tunable PC aggregation model developed by (Filippov et al., 2000) was therefore used for reconstructing the SFB agglomerates consisting of monodisperse primary particles. The fractal dimension and porosity obtained with this model were comparable to those of real SFB

agglomerates, but the algorithm was limited to prefactors less than 1.66 according to (Filippov et al., 2000; Skorupski et al., 2014). A novel approach of tuning the fractal dimension with a given prefactor (equal to one) has been introduced to overcome the limitation of the prefactor. This approach was validated by the experimental data, as the structural features (porosity and coordination number) remained essentially the same when tuned at different prefactor.

In general, however, agglomerates typically consist of polydisperse primary particles. With this respect, a polydisperse TSA model has been developed to generate the SFB agglomerates. Fractal properties (D_f and k) were precisely preserved for agglomerates with a standard deviation of 10 % of mean primary particle size, which coarsely corresponds to the available experimental results. This structural model has been combined in the comprehensive simulation framework (CVMC) to investigate the kinetics of the process. It is shown that the radius of gyration, porosity, surface area and agglomeration rate increase with primary particle dispersity.

A dynamic breakage model has, finally, been developed based entirely on the physical properties of the formulations, such as binder viscosity, agglomerate porosity, mean coordination number and primary particle size. The influence of binder viscosity and agglomerate morphology on strength has been investigated using the PTSA model. It was found that the strength of the agglomerates decreases with decreasing binder viscosity and with an increasing number of primary particles. Further, an enhanced CVMC model has been developed by implementing the breakage model in the CVMC framework. The influence of breakage decreases the arithmetic mean diameter of the particle size distribution by around 11 %. It was also found that the agglomeration growth rate decreases when breakage is considered, and an equilibrium between growth and rupture can be established.

The present comprehensive CVMC simulation, with the polydisperse tunable sequential aggregation and the dynamic breakage models, predicts satisfactorily the overall kinetics of SFB agglomeration and the morphological descriptors of SFB agglomerates under different operating conditions.

8.2 Outlook

In general, morphology-based Monte Carlo approach has demonstrated its great potential as an alternative for the simulation of the spray fluidized bed agglomeration processes. Therefore, it should be further enhanced by incorporating additional micro-mechanisms and by improving the modeling of the already considered mechanisms. One of the most important areas of improvement may be the droplet deposition mechanism.

In order to model the deposition of binder droplets and the wetting of particles (primary particles and agglomerates), the “concept of positions” (CoP) has been used. The initial number of positions on the primary particles (i.e. $N_{pos} = 48$) is calculated using Eq. (2.12). The particles were divided into sectors with respect to the assumed maximum coordination number as 6. This means that, for an agglomerate of two primary particles, the number of positions on the agglomerate is calculated as $N_{pos} = 2 * (48 - 8) = 80$. Regardless of the operating conditions, the morphology remains the same to imitate the droplet deposition on the particles. The morphology of the agglomerates could be implemented by introducing the surface area of the formed agglomerates in Eq. (2.12) after each agglomeration/breakage event by means of the aggregation model.

Further, the polydisperse aggregation model (PTSA model) could be improved to reconstruct agglomerates with higher levels of size dispersity of the primary particles. Fractal dimension D_f was precisely preserved for agglomerates with relatively high

standard deviations of primary particle size, but a shift of the fractal prefactor k was then observed. Hence, it might be reasonable to improve the model for high levels of size dispersity of the primary particles and/or very large agglomerates according to (Morán et al., 2019; Morán et al., 2020). Furthermore, the PTSA model deserves to be appraised by real agglomerates with higher standard deviations of primary particle size.

This study could also serve as a basis for further investigations by modeling the morphology and growth of soft and/or porous agglomerates. Present work could, finally, enable to investigate the morphological aspects of heteroagglomerates by reconstructing the agglomerates using more than one type of primary particles.

References

- Adetayo, A. A., & Ennis, B. J. (1997). Unifying approach to modeling granule coalescence mechanisms. *AIChE Journal*, 43(4), 927-934.
- Alves, S. G., Ferreira Jr., S. C., & Martins, M. L. (2008). Strategies for optimize off-lattice aggregate simulations. *Brazilian Journal of Physics*, 38(1), 81-86.
- Ball, R. C., & Witten, T. A. (1984). Particle aggregation versus cluster aggregation in high dimensions. *Journal of Statistical Physics*, 36(5-6), 873-879.
- Baric, V., Ciacchi, L. C., & Mädler, L. (2019). Compaction-induced restructuring of aggregated nanoparticle films using the discrete element method. *Powder Technology*, 342, 773-779.
- Barnocky, G., & Davis, R. H. (1988). Elastohydrodynamic collision and rebound of spheres: Experimental verification. *Physics of Fluids*, 31(6), 1324-1329.
- Bensimon, D., Shraiman, B., & Liang, S. (1984). On the ballistic model of aggregation. *Physics Letters A*, 102(5-6), 238-240.
- Boyce, C. M. (2018). Gas-solid fluidization with liquid bridging: A review from a modeling perspective. *Powder Technology*, 336, 12-29.
- Brasil, A. M., Farias, T. L., Carvalho, M. G., & Koylu, U. O. (2001). Numerical characterization of the morphology of aggregated particles. *Journal of Aerosol Science*, 32(4), 489-508.
- Bück, A., Tsotsas, E., & Sommer, K. (2014). Size Enlargement. *Ullmann's Encyclopedia of Industrial Chemistry* (47 pages). Weinheim: Wiley-VCH Verlag GmbH & Co. KGaA.
- Buffière, P., & Moletta, R. (2000). Collision frequency and collisional particle pressure in three-phase fluidized beds. *Chemical Engineering Science*, 55(22), 5555-5563.
- Bushell, G., & Amal, R. (1998). Fractal aggregates of polydisperse particles. *Journal of Colloid and Interface Science*, 205(2), 459-469.

- Clarke, A., Blake, T. D., Carruthers, K., & Woodward, A. (2002). Spreading and imbibition of liquid droplets on porous surfaces. *Langmuir*, 18(8), 2980–2984.
- Crowe, C. T., Schwarzkopf, J. D., Sommerfeld, M., & Tsuji, Y. (2011). *Multiphase flows with droplets and particles*. CRC Press. New York, USA.
- Dadkhah, M. (2014). *Morphological characterization of agglomerates produced in a spray fluidized bed by X-ray tomography*. Ph.D. thesis, Otto von Guericke University Magdeburg.
- Dadkhah, M., Peglow, M., & Tsotsas, E. (2012). Characterization of the internal morphology of agglomerates produced in a spray fluidized bed by X-ray tomography. *Powder Technology*, 228, 349–358.
- Dadkhah, M., & Tsotsas, E. (2014). Influence of process variables on internal particle structure in spray fluidized bed agglomeration. *Powder Technology*, 258, 165–173.
- Dastanpour, R., & Rogak, S. N. (2016). The effect of primary particle polydispersity on the morphology and mobility diameter of the fractal agglomerates in different flow regimes. *Journal of Aerosol Science*, 94, 22–32.
- Davis, R. H., Serayssol, J.-M., & Hinch, E. J. (1986). The elastohydrodynamic collision of two spheres. *Journal of Fluid Mechanics*, 163, 479–497.
- de Klerk, A. (2003). Voidage variation in packed beds at small column to particle diameter ratio. *AIChE Journal*, 49(8), 2022–2029.
- Deng, X., Huang, Z., Wang, W., & Davé, R. N. (2016). Investigation of nanoparticle agglomerates properties using Monte Carlo simulations. *Advanced Powder Technology*, 27(5), 1971–1979.
- Dernedde, M., Peglow, M., & Tsotsas, E. (2012). A novel, structure-tracking Monte Carlo algorithm for spray fluidized bed agglomeration. *AIChE Journal*, 58(10), 3016–3029.
- Dernedde, M., Peglow, M., & Tsotsas, E. (2013). Stochastic modeling of fluidized bed agglomeration: Determination of particle moisture content. *Drying Technology*, 31(15), 1764–1771.
- Dirkse, J. F., & Cawley, J. D. (1995). A modified ballistic aggregation model. *Journal of Colloid and Interface Science*, 170(2), 466–476.
- Dosta, M., Antonyuk, S., & Heinrich, S. (2013). Multiscale simulation of agglomerate breakage in fluidized beds. *Industrial & Engineering Chemistry Research*, 52(33), 11275–11281.
- Eden, M. (1961). A two-dimensional growth process. In *Proceedings of the 4th Berkeley Symposium on Mathematical Statistics and Probability*, 223–239. University of California Press.

- Eggersdorfer, M. L., & Pratsinis, S. E. (2012). The structure of agglomerates consisting of polydisperse particles. *Aerosol Science and Technology*, 46(3), 347–353.
- Ehrl, L., Soos, M., & Lattuada, M. (2009). Generation and geometrical analysis of dense clusters with variable fractal dimension. *The Journal of Physical Chemistry B*, 113(31), 10587–10599.
- Erbil, H.Y., McHale, G., & Newton, M.I. (2002). Drop evaporation on solid surfaces: constant contact angle mode. *Langmuir*, 18, 2636–2641.
- Filippov, A. V., Zurita, M., & Rosner, D. E. (2000). Fractal-like aggregates: Relation between morphology and physical properties. *Journal of Colloid and Interface Science*, 229(1), 261–273.
- Gaume, J., Löwe, H., Tan, S., & Tsang, L. (2017). Scaling laws for the mechanics of loose and cohesive granular materials based on Baxter's sticky hard spheres. *Physical Review E*, 96(3), 1–12.
- Gmachowski, L. (1995). Mechanism of shear aggregation. *Water Research*, 29(8), 1815–1820.
- Gmachowski, L. (2002). Calculation of the fractal dimension of aggregates. *Colloids and Surfaces A: Physicochemical and Engineering Aspects*, 211(2–3), 197–203.
- Goudeli, E., Eggersdorfer, M. L., & Pratsinis, S. E. (2016). Coagulation of agglomerates consisting of polydisperse primary particles. *Langmuir*, 32(36), 9276–9285.
- Hales, T. C. (1994). The status of the Kepler conjecture. *The Mathematical Intelligencer*, 16(3), 47–58.
- Hussain, M., Kumar, J., Peglow, M., & Tsotsas, E. (2013). Modeling spray fluidized bed aggregation kinetics on the basis of Monte-Carlo simulation results. *Chemical Engineering Science*, 101, 35–45.
- Hussain, M., Peglow, M., Tsotsas, E., & Kumar, J. (2014). Modeling of aggregation kernel using Monte Carlo simulations of spray fluidized bed agglomeration. *AIChE Journal*, 60(3), 855–868.
- Iveson, S. M., Litster, J. D., Hapgood, K., & Ennis, B. J. (2001). Nucleation, growth and breakage phenomena in agitated wet granulation processes: A review. *Powder Technology*, 117(1–2), 3–39.
- Jiang, Z., Bück, A., & Tsotsas, E. (2018). CFD-DEM study of residence time, droplet deposition, and collision velocity for a binary particle mixture in a Wurster fluidized bed coater. *Drying Technology*, 36(6), 638–650.

- Jiang, Z., Rieck, C., Bück, A., & Tsotsas, E. (2020). Modeling of inter- and intra-particle coating uniformity in a Wurster fluidized bed by a coupled CFD-DEM-Monte Carlo approach. *Chemical Engineering Science*, 211, 115289.
- Kamyabi, M., Saleh, K., Sotudeh-Gharebagh, R., & Zarghami, R. (2019). Effects of the number of particles and coordination number on viscous-flow agglomerate sintering. *Particuology*, 43, 76–83.
- Kätzel, U., Bedrich, R., Stintz, M., Ketzmerick, R., Gottschalk-Gaudig, T., & Barthel, H. (2008). Dynamic light scattering for the characterization of polydisperse fractal systems, Part 1: Simulation of the diffusional behavior. *Particle & Particle Systems Characterization*, 25(1), 9–18.
- Klobes, P., Meyer, K., & Munro, R. G. (2006). *Porosity and specific surface area measurements for solid materials*. Natl. Inst. Stand. Technol., Spec. Publ. 960-17, Washington, DC, USA.
- Kumar, J. (2006). *Numerical approximations of population balance equations in particulate systems*. Ph.D. thesis, Otto von Guericke University Magdeburg.
- Lapuerta, M., Ballesteros, R., & Martos, F. J. (2006). A method to determine the fractal dimension of diesel soot agglomerates. *Journal of Colloid and Interface Science*, 303(1), 149–158.
- Lapuerta, M., Ballesteros, R., & Martos, F. J. (2009). The effect of diesel engine conditions on the size and morphology of soot particles. *International Journal of Vehicle Design*, 50(1–4), 91–106.
- Li, C., Zhou, Z., Zou, R., Dong, K., Pinson, D., & Yu, A. (2018). Equivalent packing size of spheroidal particles: A microscopic test. *Powder Technology*, 333(2017), 286–292.
- Liu, L. X., Smith, R., & Litster, J. D. (2009). Wet granule breakage in a breakage only high-shear mixer: Effect of formulation properties on breakage behaviour. *Powder Technology*, 189(2), 158–164.
- Mandelbrot, B. B. (1992). Plane DLA is not self-similar; is it a fractal that becomes increasingly compact as it grows? *Physica A: Statistical Mechanics and Its Applications*, 191(1–4), 95–107.
- Meakin, P. (1983). The Vold-Sutherland and Eden models of cluster formation. *Journal of Colloid and Interface Science*, 96(2), 415–424.
- Meakin, P. (1987). Fractal aggregates. *Advances in Colloid and Interface Science*, 28(C), 249–331.
- Meakin, P. (1999). Historical introduction to computer models for fractal aggregates. *Journal of Sol-Gel Science and Technology*, 15(2), 97–117.

- Medalia, A. I. (1967). Morphology of aggregates, Part 1: Calculation of shape and bulkiness factors; application to computer-simulated random flocs. *Journal of Colloid and Interface Science*, 24(3), 393–404.
- Metropolis, N., & Ulam, S. (1949). The Monte Carlo method. *Journal of the American Statistical Association*, 44(247), 335–341.
- Morán, J., Cuevas, J., Liu, F., Yon, J., & Fuentes, A. (2018). Influence of primary particle polydispersity and overlapping on soot morphological parameters derived from numerical TEM images. *Powder Technology*, 330, 67–79.
- Morán, J., Fuentes, A., Liu, F., & Yon, J. (2019). FracVAL: An improved tunable algorithm of cluster–cluster aggregation for generation of fractal structures formed by polydisperse primary particles. *Computer Physics Communications*, 239, 225–237.
- Morán, J., Yon, J., & Poux, A. (2020). Monte Carlo Aggregation Code (MCAC), Part 1: Fundamentals. *Journal of Colloid and Interface Science*, 569, 184–194.
- Morán, J., Yon, J., Poux, A., Corbin, F., Ouf, F. X., & Siméon, A. (2020). Monte Carlo Aggregation Code (MCAC), Part 2: Application to soot agglomeration, highlighting the importance of primary particles. *Journal of Colloid and Interface Science*, 575, 274–285.
- Mörl, L., Heinrich, S., & Peglow, M. (2007). Fluidized bed spray granulation. In A. D. Salman, M. J. Hounslow, and J. P. K. Seville, editors, *Granulation*, volume 11 of *Handbook of Powder Technology*, 21–188. Elsevier Science B.V., Amsterdam, Netherlands.
- Pashminehazar, R., Ahmed, S. J., Kharaghani, A., & Tsotsas, E. (2018). Spatial morphology of maltodextrin agglomerates from X-ray microtomographic data: Real structure evaluation vs. spherical primary particle model. *Powder Technology*, 331, 204–217.
- Pashminehazar, R., Kharaghani, A., & Tsotsas, E. (2016). Three dimensional characterization of morphology and internal structure of soft material agglomerates produced in spray fluidized bed by X-ray tomography. *Powder Technology*, 300, 46–60.
- Pashminehazar, R., Kharaghani, A., & Tsotsas, E. (2019). Determination of fractal dimension and prefactor of agglomerates with irregular structure. *Powder Technology*, 343, 765–774.

- Peglow, M., Antonyuk, S., Jacob, M., Palzer, S., Heinrich, S., & Tsotsas, E. (2011). Particle formulation in spray fluidized beds. In E. Tsotsas and A. S. Majumdar, editors, *Modern Drying Technology, Product quality and formulation*, volume 3, 295–378. Wiley-VCH Verlag GmbH & Co. KGaA.
- Peglow, M., Kumar, J., Hampel, R., Tsotsas, E., & Heinrich, S. (2007). Towards a complete population balance model for fluidized bed spray agglomeration. *Drying Technology*, 25(7–8), 1321–1329.
- Rieck, C., Bück, A., & Tsotsas, E. (2020). Estimation of the dominant size enlargement mechanism in spray fluidized bed processes. *AIChE Journal*, 66(5), 1–18.
- Rong, W., Ding, W., Mädler, L., Ruoff, R. S., & Friedlander, S. K. (2006). Mechanical properties of nanoparticle chain aggregates by combined AFM and SEM: Isolated aggregates and networks. *Nano Letters*, 6(12), 2646–2655.
- Rumpf, H. (1958). Grundlagen und Methoden des Granulierens. *Chemie Ingenieur Technik*, 30(3), 144–158.
- Rumpf, H., & Schubert, H. (1974). The behavior of agglomerates under tensile strain. *Journal of Chemical Engineering of Japan*, 7(4), 294–298.
- Salman, A. D., & Hounslow, M. J. (2004). Particle breakage. *Powder Technology*, 143–144, 1.
- Schlünder, E.-U., & Tsotsas, E. (1988). *Wärmeübertragung in Festbetten, druchmischten Schüttgütern und Wirbelschichten*. Thieme, Stuttgart, Germany.
- Schulze, S., Nikrityuk, P. A., & Meyer, B. (2015). Porosity distribution in monodisperse and polydisperse fixed beds and its impact on the fluid flow. *Particulate Science and Technology*, 33(1), 23–33.
- Seville, J. P. K., Willett, C. D., & Knight, P. C. (2000). Interparticle forces in fluidisation: A review. *Powder Technology*, 113(3), 261–268.
- Singh, A. K., & Tsotsas, E. (2019). Stochastic model to simulate spray fluidized bed agglomeration: A morphological approach. *Powder Technology*, 355, 449–460.
- Singh, A. K., & Tsotsas, E. (2020). A tunable aggregation model incorporated in Monte Carlo simulations of spray fluidized bed agglomeration. *Powder Technology*, 364, 417–428.
- Skorupski, K., Mroczka, J., Wriedt, T., & Riefler, N. (2014). A fast and accurate implementation of tunable algorithms used for generation of fractal-like aggregate models. *Physica A: Statistical Mechanics and Its Applications*, 404, 106–117.

- Smith, M., & Matsoukas, T. (1998). Constant-number Monte Carlo simulation of population balances. *Chemical Engineering Science*, 53(9), 1777-1786.
- Sommerfeld, M., & Stübing, S. (2017). A novel Lagrangian agglomerate structure model. *Powder Technology*, 319, 34-52.
- Sorensen, C. M. (2011). The mobility of fractal aggregates: A review. *Aerosol Science and Technology*, 45(7), 765-779.
- Sorensen, C. M., & Roberts, G. C. (1997). The prefactor of fractal aggregates. *Journal of Colloid and Interface Science*, 186(2), 447-452.
- Sutherland, D. N. (1966). Comments on Vold's simulation of floc formation. *Journal of Colloid and Interface Science*, 22(3), 300-302.
- Sutherland, D. N. (1967). A theoretical model of floc structure. *Journal of Colloid and Interface Science*, 25(3), 373-380.
- Tan, H. S., Salman, A. D., & Hounslow, M. J. (2004). Kinetics of fluidised bed melt granulation, Part 4: Selecting the breakage model. *Powder Technology*, 143-144, 65-83.
- Tardos, G. I., Khan, M. I., & Mort, P. R. (1997). Critical parameters and limiting conditions in binder granulation of fine powders. *Powder Technology*, 94(3), 245-258.
- Tence, M., Chevalier, J. P., & Jullien, R. (1986). On the measurement of the fractal dimension of aggregated particles by electron microscopy: Experimental method, corrections and comparison with numerical models. *Journal de Physique*, 47(11), 1989-1998.
- Terrazas-Velarde, K. (2012). *Monte Carlo simulation of fluidized bed spray agglomeration*. Ph.D. thesis, Otto von Guericke University Magdeburg.
- Terrazas-Velarde, K., Peglow, M., & Tsotsas, E. (2009). Stochastic simulation of agglomerate formation in fluidized bed spray drying: A micro-scale approach. *Chemical Engineering Science*, 64(11), 2631-2643.
- Terrazas-Velarde, K., Peglow, M., & Tsotsas, E. (2011a). Kinetics of fluidized bed spray agglomeration for compact and porous particles. *Chemical Engineering Science*, 66(9), 1866-1878.
- Terrazas-Velarde, K., Peglow, M., & Tsotsas, E. (2011b). Investigation of the kinetics of fluidized bed spray agglomeration based on stochastic methods. *AIChE Journal*, 57(11), 3012-3026.

- Thouy, R., & Jullien, R. (1994). A cluster-cluster aggregation model with tunable fractal dimension. *Journal of Physics A: Mathematical and General*, 27(9), 2953–2963.
- Turkevich, L. A., & Scher, H. (1986). Sticking probability scaling in diffusion-limited aggregation. In *Fractals in Physics, Proceedings of the 6th Trieste International Symposium*, 223–229. Elsevier Science BV.
- van den Dries, K., & Vromans, H. (2002). Relationship between inhomogeneity phenomena and granule growth mechanisms in a high-shear mixer. *International Journal of Pharmaceutics*, 247(1–2), 167–177.
- van Peborgh Gooch, J. R., & Hounslow, M. J. (1996). Monte Carlo simulation of size-enlargement mechanisms in crystallization. *AIChE Journal*, 42(7), 1864–1874.
- Vanni, M. (2000). Creeping flow over spherical permeable aggregates. *Chemical Engineering Science*, 55(3), 685–698.
- Vo, T.-T., Mutabaruka, P., Delenne, J.-Y., Nezamabadi, S., & Radjai, F. (2017). Strength of wet agglomerates of spherical particles: Effects of friction and size distribution. In *Proceedings of the 8th International Conference on Micromechanics on Granular Media*, EPJ Web of Conferences, 140.
- Vold, M. J. (1963). Computer simulation of floc formation in a colloidal suspension. *Journal of Colloid Science*, 18(7), 684–695.
- Wang, C. Y., Liu, P. L., & Bassingthwaite, J. B. (1995). Off-lattice Eden-C cluster growth model. *Journal of Physics A: Mathematical and General*, 28(8), 2141–2147.
- Witten, T. A., & Sander, L. M. (1981). Diffusion-limited aggregation, a kinetic critical phenomenon. *Physical Review Letters*, 47(19), 1400–1403.
- Wu, M. K., & Friedlander, S. K. (1993). Enhanced power law agglomerate growth in the free molecule regime. *Journal of Aerosol Science*, 24(3), 273–282.
- Yu, W. (2016). Applications of Monte Carlo method to 3-D capacitance calculation and large matrix decomposition. In *Proceedings of the 13th IEEE International Conference on Solid-State and Integrated Circuit Technology (ICSICT)*, 227–230. IEEE.
- Zhang, B., Yu, W., & Mascagni, M. (2019). Revisiting Kac's method: A Monte Carlo algorithm for solving the telegrapher's equations. *Mathematics and Computers in Simulation*, 156, 178–193.
- Zhao, H., Maisels, A., Matsoukas, T., & Zheng, C. (2007). Analysis of four Monte Carlo methods for the solution of population balances in dispersed systems. *Powder Technology*, 173(1), 38–50.

Appendix A Coordination angle

The coordination angle, θ_c , is defined as the angle between the vectors connecting the center of each primary particle to the centers of two of its recognized contact neighbors. For example, if a particle has three touching neighbors, then that particle also has three coordination angles, as shown in Fig. A.1. In order to calculate the coordination angle, all vectors connecting the contacting primary particles were identified and the angles (less than 180°) between them were evaluated using the dot (scalar) product of the vectors.

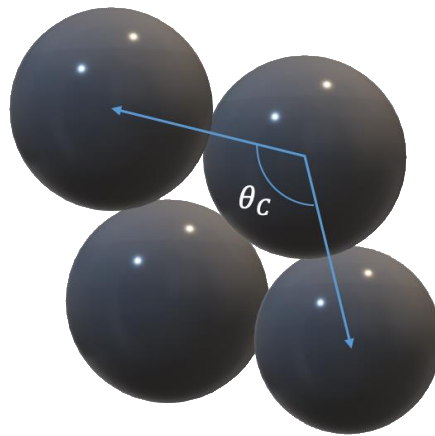


Fig. A.1: Representation of coordination angle (θ_c) of a primary particle with its three contacting neighbors in an aggregate.

The coordination angles of all the primary particles of an agglomerate result in the distribution of coordination angle. An illustration of coordination angle distribution of an agglomerate consisting of 200 monodisperse primary particles generated using the TSA model (detailed description is given in Section 4.7) is shown in Fig. A.2. The

coordination angle distribution is a property that is useful in determining the stability of spray fluidized bed agglomerates (Dadkhah, 2014; Pashminehazar et al., 2018).

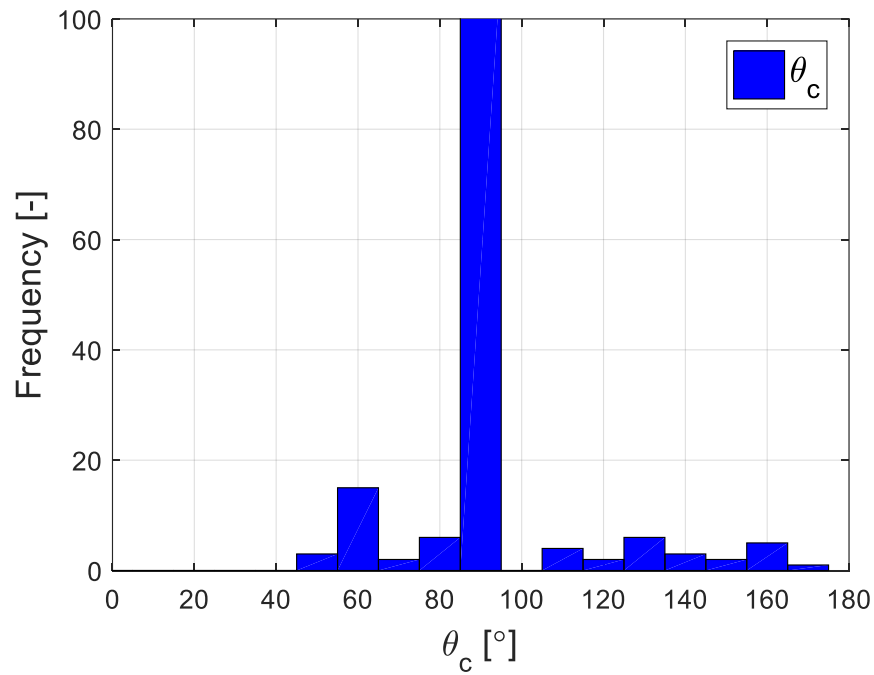


Fig. A.2: Coordination angle (θ_c) distribution of an agglomerate with 200 monodisperse primary particles.

Appendix B Experiments of Dadkhah

In the experiments of Dadkhah (Dadkhah, 2014), a laboratory-scale fluidized bed agglomerator with an inner diameter of 152 mm and a height of 450 mm was used. The binder consisted of hydroxypropylmethylcellulose (HPMC) in water, injected in top spray configuration through a two-fluid nozzle located 150 mm above the air distributor plate. The main experimental parameters are shown in Table B.1.

Table B.1. Experimental parameters.

Bed mass	M_{bed}	500	g
Primary particle density	ρ_p	2500	kg/m ³
Binder density	ρ_l	998.5-1024.0	kg/m ³
Binder addition rate	\dot{M}_l	200	g/h
Dry gas mass flow rate	\dot{M}_g	130	kg/h

Five experiments were carried out with glass beads to investigate the influence of process parameters (inlet air temperature and initial binder mass fraction) listed in Table B.2, with Exp. A as the reference experiment. The transition from experiment B to A and then to C represents the conditions of increasing inlet temperature of the fluidization gas. The transition from experiment A to experiments D and E corresponds to an increasing binder mass fraction.

Glass beads (non-porous), as primary particles, were found to have very high sphericity (0.98). Measured by Camsizer, the size of glass beads was normally distributed with an average radius of 260 μm and standard deviation of around 10 %

from the mean radius. The size distributions of glass beads are plotted in Fig. B.1. The findings of Dadkhah's experiments measured by X-ray tomography for each experiment are given in Appendix B.1. The mean and standard deviation of radii of the glass beads (primary particles) evaluated from individual agglomerate X-ray tomography data are given in Table B.2 (and in Fig. B.1; for experiment A). In accordance with the Camsizer data the standard deviation of the primary particle radius is around 10 % of the arithmetic mean value for all the experiments except Exps. B and E with 1 % and 3 %, respectively.

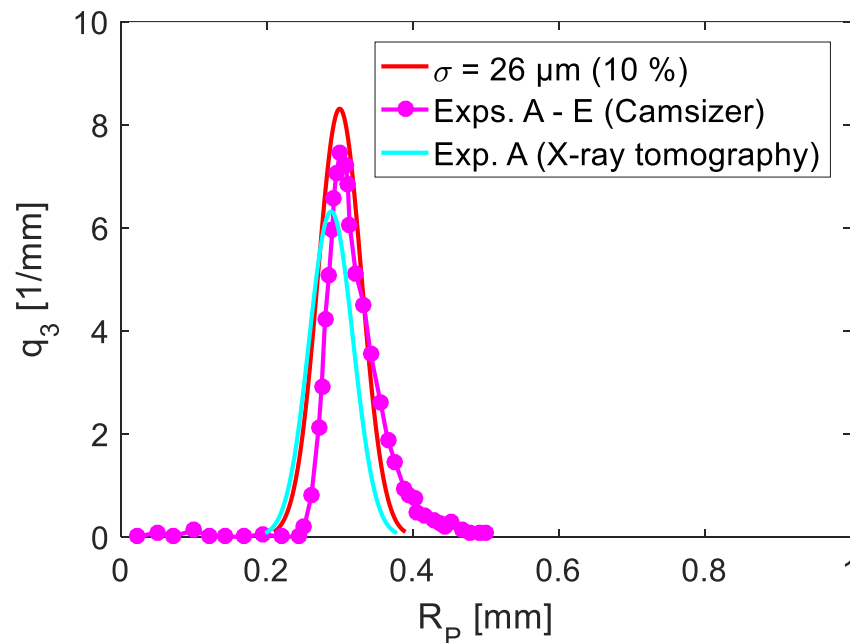


Fig. B.1: Particle size distribution of glass beads from Camsizer and primary particles evaluated from X-ray tomography data of individual agglomerates of Exp. A.

Experiment F was conducted with porous primary particles made of $\gamma\text{-Al}_2\text{O}_3$ under otherwise the same conditions as experiment A. $\gamma\text{-Al}_2\text{O}_3$ primary particles have a sphericity of 0.97 and diameters between 580 and 650 μm , with an average diameter of 616 μm (measured from Camsizer).

The morphological descriptors (D_f , k , average ε_{agg} , average MCN) obtained for the different experiments are also shown in Table B.2. In order to derive these descriptors, around 24 agglomerates were investigated for each experiment (exact number of evaluated agglomerates for each experiment is given in Table B.2).

Table B.2. Experimental results for each trial.

	A	B	C	D	E	F
Primary particles	Glass	Glass	Glass	Glass	Glass	$\gamma\text{-Al}_2\text{O}_3$
Temperature [°C]	60	30	90	60	60	60
Binder [wt. %]	2	2	2	6	10	2
Growth rate [$\mu\text{m}/\text{s}$]	1.068	1.146	0.630	3.789	8.204	0.599
D_f [-]	2.45	2.31	2.94	2.24	2.09	2.45
k [-]	1.76	2.01	0.98	1.96	2.24	1.60
Average ε_{agg} [-]	0.57	0.62	0.53	0.58	0.63	0.62
Average MCN	3.32	3.10	4.02	2.92	2.87	3.16
Evaluated agglomerates	25	28	22	24	24	25
R_p [μm]	[321.2 236.8]	[317.3 303.3]	[298.6 210.4]	[342.9 229.5]	[332.0 300.3]	[311.4 301.7]
Mean R_p [μm]	288.2	309.3	257.3	285.3	312.4	308.6
Standard deviation of R_p [μm]	30	3	33	32	9	2

B.1 Detailed results of experiments A to F

Table B.3. Detailed morphological data for experiment A.

N_p [-]	R_p [μm]	R_g [μm]	$\epsilon_{\text{agg}}(R_g)$ [-]
4	316.5	432.6	0.169
8	255.4	526.2	0.268
12	252.2	596.7	0.569
15	303.5	701.7	0.635
19	306.7	819.0	0.425
20	321.2	901.1	0.533
21	304.5	827.2	0.573
22	307.4	837.7	0.531
23	311.7	890.1	0.492
25	311.9	930.9	0.535
34	311.7	1073.9	0.555
32	257.2	863.3	0.607
40	241.5	1008.2	0.615
41	253.9	926.2	0.763
42	249.4	1001.8	0.618
43	246.1	916.9	0.732
52	255.3	1117.7	0.633
57	304.9	1174.9	0.731
95	313.6	1483.3	0.530
96	312.9	1451.5	0.577
104	309.3	1479.0	0.546
132	312.1	1892.4	0.552
173	310.4	1761.2	0.721
198	236.8	1649.8	0.554

Table B.4. Detailed morphological data for experiment B.

N_p [-]	R_p [μm]	R_g [μm]	$\varepsilon_{\text{agg}}(R_g)$ [-]
10	312.1	593.3	0.320
11	308.6	704.6	0.570
14	317.3	701.4	0.395
15	305.3	700.8	0.414
19	310.7	840.6	0.576
26	304.1	894.1	0.519
27	306.3	951.2	0.595
28	312.9	1024.9	0.625
28	310.6	1003.2	0.605
31	307.8	1011.0	0.575
32	306.4	1037.2	0.610
36	306.7	1100.7	0.647
37	311.4	1103.1	0.649
40	312.2	1082.3	0.547
45	309.6	1284.7	0.734
46	311.2	1231.6	0.679
47	312.1	1225.8	0.636
48	309.8	1347.1	0.743
50	311.4	1212.9	0.662
60	308.1	1317.2	0.682
61	303.3	1258.5	0.597
103	308.5	1625.0	0.705
127	309.8	1790.2	0.718
131	307.7	1870.0	0.761
141	308.9	1946.8	0.734
182	312.1	2174.3	0.746
205	307.5	2277.8	0.789
215	306.8	2338.8	0.771

Table B.5. Detailed morphological data for experiment C.

N_p [-]	R_p [μm]	R_g [μm]	$\epsilon_{\text{agg}}(R_g)$ [-]
9	267.0	549.6	0.311
10	295.6	595.7	0.359
20	219.6	664.5	0.580
23	210.4	705.9	0.635
28	298.5	875.0	0.470
30	229.5	693.6	0.394
31	232.5	764.2	0.543
34	224.1	743.2	0.486
42	296.2	1002.0	0.487
47	298.6	1105.1	0.561
52	294.8	1176.2	0.611
65	262.9	1089.8	0.604
97	292.5	1342.3	0.526
101	226.4	1063.2	0.511
110	293.6	1432.5	0.551
115	220.5	1124.6	0.531
122	227.5	1250.9	0.606
145	296.5	1622.9	0.581
148	262.7	1361.6	0.541
187	252.9	1470.1	0.592
226	220.8	1371.6	0.510
289	238.3	1646.4	0.531

Table B.6. Detailed morphological data for experiment D.

N_p [-]	R_p [μm]	R_g [μm]	$\epsilon_{\text{agg}}(R_g)$ [-]
6	342.9	610.5	0.503
7	296.1	559.3	0.511
8	318.8	606.9	0.455
9	256.8	476.6	0.406
9	229.5	421.1	0.285
12	290.4	434.8	0.455
13	297.9	450.8	0.541
16	304.7	790.3	0.547
17	315.7	875.6	0.626
18	318.7	887.2	0.605
19	310.6	816.5	0.510
20	299.5	845.9	0.577
25	291.4	1062.4	0.747
27	246.0	820.8	0.661
28	300.9	1097.9	0.726
29	299.5	1047.6	0.680
30	252.2	882.7	0.716
34	245.1	931.6	0.728
60	308.1	1167.5	0.481
65	300.2	1391.8	0.689
112	238.5	1283.4	0.682
127	245.3	1565.7	0.777
129	236.7	1603.6	0.811
214	301.7	2158.0	0.722

Table B.7. Detailed morphological data for experiment E.

N_p [-]	R_p [μm]	R_g [μm]	$\epsilon_{\text{agg}}(R_g)$ [-]
6	308.8	474.9	0.227
8	316.3	584.1	0.404
9	314.3	646.5	0.508
14	313.5	827.9	0.641
21	306.2	935.0	0.652
23	309.2	956.3	0.635
24	307.1	1044.1	0.712
26	301.9	889.0	0.518
27	310.1	924.9	0.518
30	326.1	1507.2	0.853
36	309.5	1028.2	0.537
37	328.5	1538.5	0.824
38	306.1	1272.5	0.749
42	318.5	1294.2	0.704
45	316.2	1211.9	0.623
52	303.7	1288.9	0.677
62	301.4	1300.6	0.630
72	302.4	1427.1	0.675
83	302.5	1673.3	0.767
92	300.3	1547.7	0.682
102	323.9	2148.3	0.830
150	323.2	2311.4	0.801
170	317.0	2330.0	0.794
212	332.0	3000.1	0.860

Table B.8. Detailed morphological data for experiment F.

N_p [-]	R_p [μm]	R_g [μm]	$\epsilon_{\text{agg}}(R_g)$ [-]
8	310.6	587.8	0.451
9	309.3	622.1	0.586
10	304.9	686.9	0.592
11	308.6	704.6	0.569
13	309.6	710.7	0.533
14	310.1	763.5	0.564
19	310.7	840.6	0.576
22	306.3	821.6	0.490
23	308.0	959.9	0.676
27	306.3	951.2	0.595
30	307.9	978.9	0.594
36	306.7	1100.7	0.647
37	311.4	1103.1	0.649
45	309.6	1284.7	0.734
46	311.2	1231.6	0.679
48	309.8	1347.1	0.742
49	311.5	1206.7	0.657
50	310.7	1267.1	0.664
60	308.1	1317.2	0.579
80	306.7	1400.7	0.662
103	308.5	1625.0	0.705
127	309.9	1790.2	0.718
129	308.9	1878.9	0.768
186	301.7	2107.6	0.765
205	307.5	2277.8	0.789

Appendix C Estimation of agglomerate diameter

Agglomerates with number of primary particles from 5 to 250 are aggregated at an increment of 5 for different experimental trials (given in Appendix B). Those agglomerates are generated using the PTSA model with a mean radius of primary particles as 260 μm and a standard deviation of 26 μm . Fractal properties for the PTSA model are taken from Eqs. (3.18) and (3.17) by inserting inlet fluidization gas temperature and binder mass fraction for the respective experiment according to Table B.2.

Figure C.1 shows the ratio between AES and VES diameter for agglomerates generated using the PTSA model, plotted over the number of primary particles present in the agglomerate. The ratio decreases with increasing number of primary particles in the agglomerates. It is almost the same for compact agglomerates (as in the case of Exps. A and C) with high D_f . However, the ratio increases for tenuous agglomerates (especially for Exp. E) with low D_f .

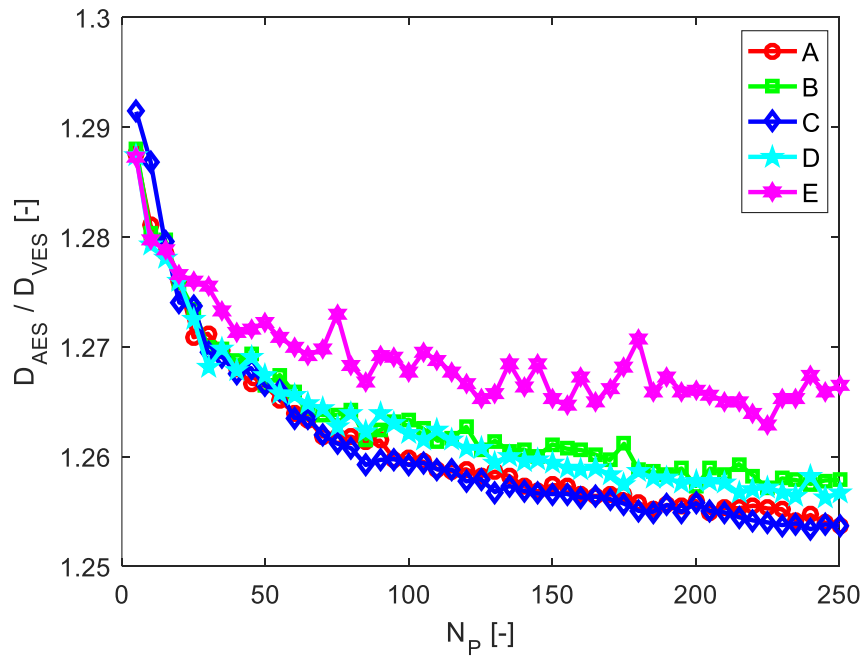


Fig. C.1: Ratio of AES and VES diameters of agglomerates generated using the PTSA model for the different experiments.

Appendix D Simulation parameters for different experiment trials

This appendix summarizes the simulation parameters used to investigate the influence of the main operating parameters on the agglomeration behavior in Chapter 7. Experiments B, A and C represent the increase of inlet fluidized gas temperature from 30°C to 60°C and 90°C. Similarly, experiments A, D, and E represent increasing binder (hydroxypropylmethylcellulose, HPMC) mass fraction of 2 wt. %, 6 wt. % and 10 wt. %.

Table D.1 contains the parameters used for the respective simulations. It relates the simulations to parameter variations corresponding to the respective experiment.

Table D.1. Simulation parameters.

		A	B	C	D	E	
Bed mass	M_{bed}	500	500	500	500	500	g
Primary particle diameter	D_p	0.52	0.52	0.52	0.52	0.52	mm
Primary particle density	ρ_p	2500	2500	2500	2500	2500	kg/m ³
Particle surface asperities height	h_a	10	10	10	10	10	μm
Particle restitution coefficient	e	0.8	0.8	0.8	0.8	0.8	-
Droplet diameter	D_d	80	80	80	80	80	μm
Droplet addition rate	γ	0.08	0.08	0.08	0.08	0.08	1/s
Particle-droplet contact angle	θ	40	40	40	40	40	°
Positions on the primary particle surface	N_{pos}	48	48	48	48	48	-
Binder mass fraction	x_b	2	2	2	6	10	wt. %
Binder density	ρ_l	998.5	998.5	998.5	1014	1024	kg/m ³
Binder addition rate	\dot{M}_l	200	200	200	200	200	g/h
Binder viscosity	μ_l	0.0086	0.0086	0.0086	0.0597	0.3222	Pa·s
Fluidization velocity	u_0	1.912	1.912	1.912	1.912	1.912	m/s
Collision velocity, mean value	u_c	0.956	0.956	0.956	0.956	0.956	m/s
Collision velocity, standard deviation	σ_u	0.1	0.1	0.1	0.1	0.1	m/s
Gas mass flow rate	\dot{M}_g	130	130	130	130	130	kg/h
Gas inlet temperature	T_g	60	30	90	60	60	°C
Saturation temperature	T^*	20	14	30	20	20	°C
Moisture content in the gas	Y_g	3.4	3.4	3.4	3.4	3.4	g/kg
Molar fraction of vapor in the gas	\tilde{y}_g	0.0031	0.0031	0.0031	0.0031	0.0031	-